









R First Author 1973-1995 Oh Park Pierce Pope Quinn Ramirez Rockhold Russell Gregonis Ives Suci Jhon			
View Arrange By Action Share Edit Tags			Search
SCIENCE_WITHO... AirDrop All My Files Downloads Cloud Drive	Name	Date Modified	Size
	 Ramirez 1973 Iron CoPolymer.pdf	Jun 4, 2006, 5:19 PM	1.7 MB
	 Ramirez 1974 Poly...olymer-Drug iron.pdf	Oct 31, 2017, 6:04 PM	588 KB
	 Ramirez 1976 Polymer Iron.pdf	Jun 4, 2006, 5:53 PM	6.8 MB
	 Reichert 1985 Raman Chapter Bk V.1.pdf	Jun 4, 2006, 4:53 PM	3.5 MB
	 Reichert 1987 TIRF Models suci ives .pdf	Apr 17, 2006, 9:06 PM	3.2 MB
	 Rockhold 1983 TIRF quinn reichert.pdf	Oct 11, 2006, 6:03 PM	3.3 MB
	 Russell 1976 ACS B...devisser dalling.pdf	Jul 3, 2006, 4:01 PM	1.7 MB
	 Russell 1980 Relax...regonis devisser.pdf	Oct 12, 2006, 9:40 PM	2 MB

last
page

- [9] C. F. Whitten, G. W. Gibson, M. H. Good, J. F. Goodwin, and J. Brough, *Pediatrics*, **36**, 322 (1965).
- [10] J. T. McEnery, *Clin. Toxicol.*, **4**, 603 (1971).
- [11] H. Brunner, G. Peters, and R. Jaques, *Helv. Physiol. Acta*, **21**, 3 (1963).
- [12] W. F. Westlin, *Clin. Pediat.*, **5**, 531 (1966).
- [13] J. D. Andrade, R. Van Wagenen, C. Chen, M. Ghavamian, J. Volder, R. Kirkham, and W. J. Kolff, *Trans. Amer. Soc. Artif. Int. Organs*, **18**, 473 (1972).
- [14] J. D. Andrade, K. Kunitomo, R. Van Wagenen, B. Kastagir, D. Gough, and W. J. Kolff, *Ibid.*, **17**, 222 (1971).
- [15] R. C. Schulz, K. Meyersen, and W. Kern, *Makromol. Chem.*, **54**, 156 (1962).
- [16] R. C. Schulz, in *Vinyl Polymerization*, Vol. 1, Part I (G. E. Ham, ed.), Dekker, New York, 1967, Chap. 7.
- [17] E. E. Seibert, *J. Polymer Sci., Part C*, **8**, 87 (1965).
- [18] C. Rhem, CIBA Pharmaceutical Co., Personal Communication.
- [19] H. Bickel, H. Keberle, and E. Vischer, *Helv. Chim. Acta*, **46**, 1385 (1963).
- [20] K. Nakanishi, *Infrared Absorption Spectroscopy*, Holden-Day, San Francisco; Naukodo, Tokyo, 1962.
- [21] L. J. Bellamy, *The Infrared Spectra of Complex Molecules*, Methuen, London; Wiley, New York, 1958.
- [22] R. C. Schulz, R. Hollander, and W. Kern, *Makromol. Chem.*, **40**, 16 (1960).
- [23] H. H. Willard, L. L. Merritt, Jr., and J. A. Dean, *Instrumental Methods of Analysis*, Van Nostrand, Princeton, New Jersey, 1965, p. 104.

Received for publication January 29, 1973

J. MACROMOL. SCI.—CHEM., A7(5), pp. 1035-1045 (1973)

A Novel Iron-Chelating Graft Copolymer

R. S. RAMIREZ

Division of Materials Science and Engineering and Institute for Biomedical Engineering
University of Utah
Salt Lake City, Utah 84112

Instituto de Química
Universidad Católica de Chile
Santiago, Chile

and

J. D. ANDRADE

Division of Materials Science and Engineering and Institute for Biomedical Engineering
University of Utah
Salt Lake City, Utah 84112

ABSTRACT

Deferoxamine B, liberated from its methane-sulfonate salt, has been linked to the chemically reactive polyacrolein to form polyacrolein-deferoximine (PADFI), whose structure may contain imino groups as well as N-acetal groups. Free aldehydes are still present in the polymer structure.

The polyacrolein-deferoximine is stable in physiological saline solution for at least 24 hr. A sample of 0.3000 g of PADFI removes 40% of iron(III) from a 1.8×10^{-3} M solution. The polymer, PADFI, is insoluble in most ordinary solvents, and it failed to dissolve completely in sulfur dioxide solution. Deferoxamine B attached to a polymer backbone may be useful as an insolubilized chelating agent for the extracorporeal treatment of severe iron poisoning.

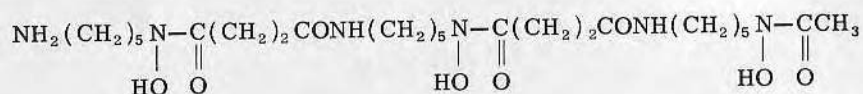
1035

INTRODUCTION

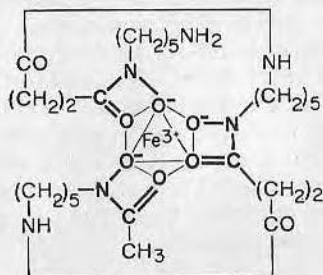
Acute iron poisoning is a common cause of poisoning among young children [1]. One of the few ways in which dangerously high levels of iron can be treated is through the use of a strong chelate for iron. One of the most specific and irreversible of the iron chelating agents is deferoxamine B, a derivative of which is a drug produced by CIBA under the brand name of Desferal (trademark, CIBA Pharmaceutical Co., Summit, New Jersey) [2].

Deferoxamine B is isolated from feroxamine B, an iron-bearing metabolite belonging to the sideramines, a group of natural occurring substances [3, 4]. Due to its great affinity for iron and to its rapid excretion by the kidneys, deferoxamine B is used clinically for the treatment of severe acute iron poisoning [1]. The relatively low molecular weight iron-deferoxamine B complex is hydrophilic and water soluble, so that it can pass through the kidneys. Roughly 10 parts by weight of the drug will bind one part of Fe(III). The stability constant of the complex is approximately 10^{31} in aqueous solutions ranging from pH 3 to 8. This value is about 15 powers of ten higher than the stability constants for other metallic complexes of deferoxamine B [5]. This difference is greater than in the case of synthetic chelating agents. On the other hand, the complexes of transferrin and ferritin (the two iron transporting proteins in the blood) with iron are more stable than feroxamine B, meaning that deferoxamine B should not remove iron from such proteins [6].

Chemically, deferoxamine B is a trihydroxamic derivative, whose structural formula is



It reacts stoichiometrically with Fe(III) to form feroxamine B, an octahedral iron complex [7]:



The pH range in which feroxamine B formation is rapid and quantitative is 2 to 4.5. Between pH 4.5 and 7.0 complex formation becomes increasingly incomplete, in direct relation to the pH and buffer capacity. Above pH 8 practically no feroxamine B is formed [7].

Lentz et al. [8] have studied the kinetics of complex formation and found that the second-order reaction had a rate constant of $2.5 \times 10^3 \text{ M}^{-1} \text{ sec}^{-1}$. The half life for the reaction is about 2.5 sec and the activation energy is about 12 kcal.

Studies of Whitten et al. [9] showed that equimolar quantities of Fe(II) and deferoxamine B at pH 6 yield as much complex as is formed by equimolar quantities of Fe(III). This is due either to the rapid oxidation of Fe(II) to Fe(III) in the presence of deferoxamine B, or the latter forms an unstable complex with Fe(II) which is rapidly converted to stable Fe(III) complex.

When serum iron levels exceed $500 \mu\text{g} \%$, the serum iron-binding proteins become saturated, thus free iron is present. Iron levels in the 500 to $1000 \mu\text{g} \%$ range are considered high and dangerous. Levels substantially above this are potentially lethal. Serum irons as high as $30,000 \mu\text{g} \%$ have been measured. In most iron poisoning situations deferoxamine B can be applied quite successfully and with minimal side effects [2, 10]; however, both the drug and its iron complex are toxic if present in large amounts. They have been shown to produce hypotension and tachycardia in dogs, cats, and rabbits [11], and in children [9, 12]. The use of deferoxamine B is thus dose-restricted [10]. In very severe poisoning cases the maximum amount of drug which can safely be used may not be sufficient for the removal of the required amounts of iron.

To avoid the problem of toxicity of large doses of deferoxamine B and its iron complex, we have bonded the drug to a polymer, thus rendering it insoluble. We propose that the chelating polymer can be fabricated in bead form; the patient's blood can then be perfused through a column packed with this material to chelate and retain the iron, thus purifying the blood from plasma iron, analogous to the method described by Andrade et al. [13, 14] for the removal of uremic toxins and certain poisons. Deferoxamine B has a free NH_2 group that is apt to react with other functional groups. This NH_2 group in the deferoxamine B molecule is not directly involved in the formation of the octahedral complex [2], since this compound acts as a hexadentate chelating agent, according to the structure described by Schwarzenbach [7].

Thus it would be possible to react polyacrolein with deferoxamine B to obtain an insoluble polymer that is able to remove iron from solution. We used polyacrolein as our polymeric substrate since it reacts with amines in the presence of organic solvents [15] without introducing acids or bases that may either hydrolyze the trihydroxamic acid or produce aldol condensation reactions [16].

Acrolein may be polymerized in two ways: by free radical polymerization to form addition polymers through the C=C double bond, and by ionic (both cationic and anionic) polymerization, where the addition is to the C=C double bond and to the C=O double bond.

In the free radical polymerization the structure of the polymer has been shown to contain free carbonyl groups (Fig. 1a) as well as hydrated carbonyl groups (Fig. 1b) and cyclic hemiacetals (Fig. 1c) [15].

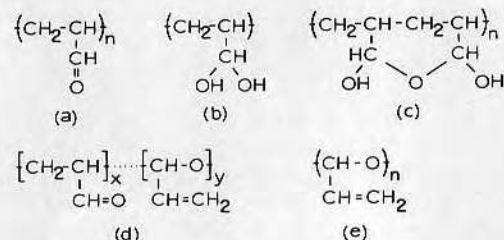


FIG. 1. Representative forms of polyacrolein polymerized under different conditions. Free radical polymerization produces a polymer containing free carbonyls (a), hydrated carbonyls (b), and cyclic hemiacetals (c). Ionic polymerization produces free vinyl and free aldehyde groups (d). The polymer can also be formed with free vinyl groups (e); see text.

Ionic polymerization of acrolein leads to the formation of polymers with free vinyl and aldehyde groups (Fig. 1d). The exception is when the polymerization is carried out with sodium or sodium cyanide in tetrahydrofuran or toluene at low temperatures [16]. In this case the polymers contain only vinyl groups (Fig. 1e).

The three different groups present in the polyacrolein obtained by free radical polymerization may react with amines as was shown by Schulz et al. [15]. By using low molecular weight model compounds they demonstrated that polyacrolein reacts with amines or hydrazines to form, in addition to azomethine groups (Fig. 2b), N-acetal groups (Fig. 2a).

EXPERIMENTAL

Polyacrolein [16]

Polyacrolein was prepared by free radical polymerization of acrolein (Polysciences, Inc., Warrington, Pennsylvania). Fifty grams

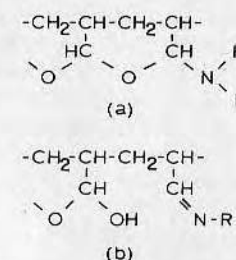


FIG. 2. Structures of the reaction products of polyacrolein and primary amines: (a) N-acetals, (b) azomethines (see Ref. 16).

of freshly distilled acrolein was dissolved in 200 ml of benzene and then 0.3 g of 2,2'-azo-bis-(2-methyl-propionitrile) (Eastman Kodak, Rochester, New York) was added to the solution. The mixture was refluxed for about 72 hr and the polymer precipitated out. A white, fine dustless powder was obtained in about 90% yield. The IR spectrum of the polyacrolein (Fig. 3) was identical to that reported in the literature [16].

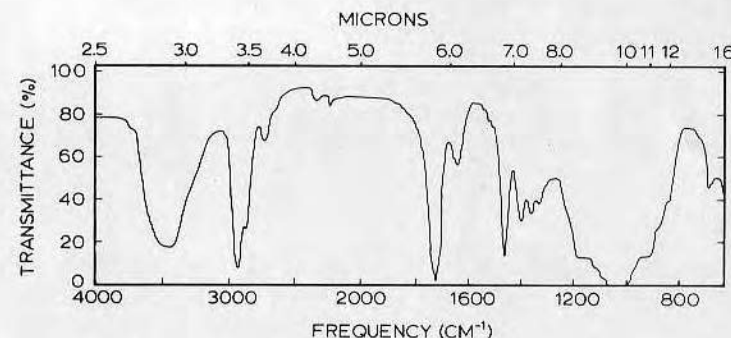


FIG. 3. IR spectrum of polyacrolein obtained by free radical polymerization in benzene (KBr pellet).

Intrinsic Viscosity

The intrinsic viscosity of polyacrolein was determined according to the procedure described by Seibert [17] by using the one point relation:

$$[\eta] = 0.96897\eta_{sp} - 0.30936\eta_{sp}^2 + 0.09064\eta_{sp}^3 \quad (1)$$

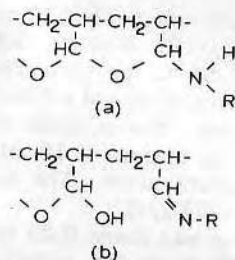


FIG. 2. Structures of the reaction products of polyacrolein and primary amines: (a) N-acetals, (b) azomethines (see Ref. 16).

of freshly distilled acrolein was dissolved in 200 ml of benzene and then 0.3 g of 2,2'-azo-bis-(2-methyl-propionitrile) (Eastman Kodak, Rochester, New York) was added to the solution. The mixture was refluxed for about 72 hr and the polymer precipitated out. A white, fine dustless powder was obtained in about 90% yield. The IR spectrum of the polyacrolein (Fig. 3) was identical to that reported in the literature [16].

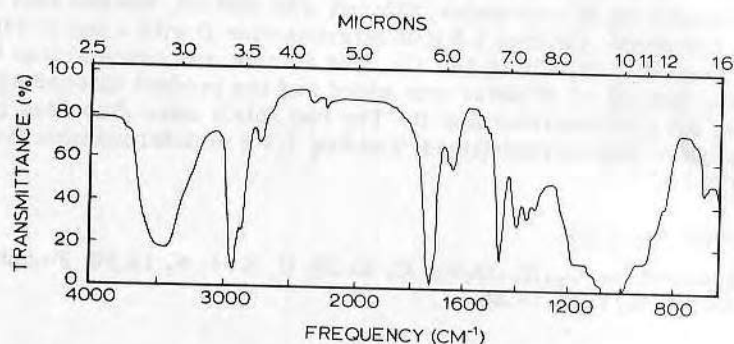


FIG. 3. IR spectrum of polyacrolein obtained by free radical polymerization in benzene (KBr pellet).

Intrinsic Viscosity

The intrinsic viscosity of polyacrolein was determined according to the procedure described by Seibert [17] by using the one point relation:

$$[\eta] = 0.96897\eta_{sp} - 0.30936\eta_{sp}^2 + 0.09064\eta_{sp}^3 \quad (1)$$

The polyacrolein (2.0 g) was suspended in water (50 ml) and the suspension saturated with sulfur dioxide. After 1 hr the polyacrolein was completely dissolved due to the formation of the polyacrolein-SO₂ adduct. The excess SO₂ was stripped off by bubbling nitrogen into the solution and then by vacuum. The solution was filtered through a sintered glass funnel and an aliquot of 10 ml was evaporated to dryness to determine the concentration. The concentration *c* measured by this procedure was 0.4288 g/dl.

The rest of the solution was made 0.25 M with sodium sulfate and diluted to 100 ml with 0.25 M Na₂SO₄ solution. The viscosity measurements were made on the polyacrolein-SO₂ solution and on the 0.25 M Na₂SO₄ solution used as solvent; the result was $\eta_{sp} = 0.16$. The intrinsic viscosity as calculated from Eq. (1) was $[\eta] = 0.38$.

Deferoxamine B

Liberation from Its Methane Sulfonate Salt (Desferal) [18, 19]

Desferal (3.9 g) was dissolved in warm water (12.5 ml). After cooling the solution in an ice bath, 2.5 ml of 2 N potassium bicarbonate was added and the container scratched while cooling until precipitation started. The solution was left at room temperature for 2 hr and the diluted with 5 ml of cold water, filtered with suction, washed with cold water, and dried, yielding 1.5 g of deferoxamine B with a mp of 138–140°C (mp lit. [19] 138 to 140°C). The filtrate was concentrated to dryness, then 10 ml of water was added and the product filtered again yielding 0.6 g of deferoxamine B. The two solids were dissolved in hot methanol and recrystallized, yielding 1.9 g of deferoxamine B of 139 to 140°C.

Elemental Analysis

Calculated for C₂₅H₄₈O₈N₆: C, 53.38; H, 8.54; N, 14.95. Found: C, 52.01; H, 8.71; N, 14.86.

IR Spectrum

The IR spectrum of deferoxamine B is shown in Fig. 4. This spectrum is consistent with the structure of deferoxamine B, having —NH₂ group bands (3440 and 3320 cm⁻¹) overlapped with the strong OH bands of the hydroxamic acids; —CH₂— groups (2940 and 2860 cm⁻¹) and —N—C=O groups (1650 cm⁻¹) [20, 21].

Polyacrolein-Deferoximine (PADFI)

Polyacrolein was reacted with deferoxamine B by a procedure similar to that used by Schulz et al. [22] for the reaction of polyacrolein

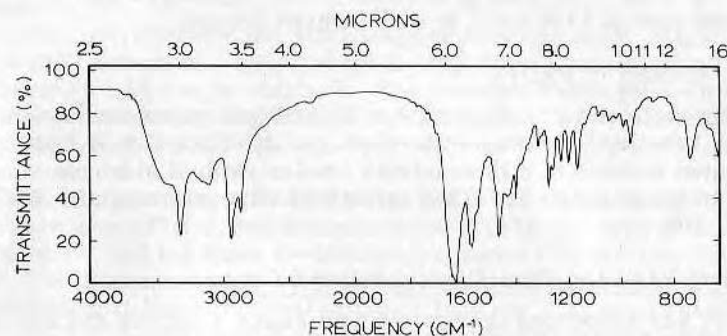


FIG. 4. IR spectrum of deferoxamine B (KBr pellet).

and amines. Thus 1 g of polyacrolein was let swell in 50 ml of dimethylformamide (DMF) and heated to 60°C; then a solution of 1 g of deferoxamine B in 50 ml of DMF at 60°C was added to the partly swollen, partly dissolved polyacrolein. The mixture was kept at 60°C for 2 hr, during which it took on a brownish color, and then stirred at room temperature overnight. Then water was added to precipitate the polymer in solution. The brown polymer was filtered, washed with water, dried, and triturated with hot methanol to eliminate the unreacted deferoxamine B, then filtered, washed with water, and dried under vacuum at 60°C.

IR Spectrum

The IR spectrum of PADFI is shown in Fig. 5. The broad, strong band centered at 3400 cm^{-1} indicates the presence of hydrogen bonded

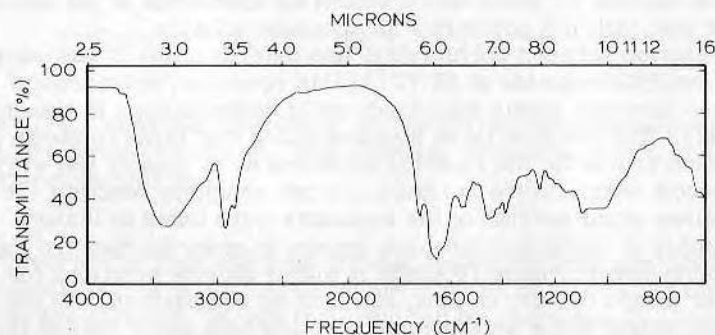


FIG. 5. IR spectrum of polyacrolein-deferoximine (PADFI), (KBr pellet).

hydroxyl groups. The band at 1650 cm^{-1} corresponds to the $-\text{N}=\text{C}=\text{O}$ groups and that at 1720 cm^{-1} to the aldehyde groups.

Nitrogen Content of PADFI

The theoretical nitrogen content of PADFI was calculated assuming complete reaction between polyacrolein and deferoxamine B. By taking equal weights of both reactants (molar ratio of aldehyde groups/amino groups = 10/1) the calculated nitrogen content is 8.4%. Found: 7.16%.

Stability of PADFI in Physiological Saline Solution

PADFI was suspended in physiological saline solutions and stirred at 36 to 37°C for 24 hr. After this period, PADFI was filtered, washed with water, and dried. The IR spectrum of this product is identical to that of untreated material, the solution showed a decrease in Fe(III) content and when left in contact with ferric chloride solution.

Iron Chelation Test for PADFI

A sample of 0.3000 g of PADFI was left in contact with 10 ml of a solution of 0.0290 g of ferric chloride in 100 ml water for 16 hr. After this period the PADFI was filtered and the filtrate analyzed for Fe(III) at 396 $\text{m}\mu$ [23], giving an absorbance of 0.92 whereas the standard ferric chloride solution gave an absorbance of 1.5. This value corresponds to a 40% decrease in Fe(III) concentration.

RESULTS AND DISCUSSION

Polyacrolein, prepared by free radical polymerization of acrolein with 2,2'-azo-bis-(2-methyl-propionitrile) as initiator, was reacted with deferoxamine B, which was obtained by hydrolysis of its methane sulfonate salt with 2 N potassium bicarbonate solution.

The reaction between polyacrolein and deferoxamine B was carried out in dimethylformamide at 60°C. In this condition, polyacrolein swells and becomes partly dissolved, while deferoxamine B dissolves completely. The solution takes a yellow color that turns to brown as the reaction proceeds; the reaction mixtures were usually left overnight at room temperature to insure a more complete reaction. In all the reactions equal weights of the reactants were taken to leave a large number of unreacted aldehyde groups in order to dissolve the polyacrolein-deferoximine (PADFI) in sulfur dioxide solutions for molecular weight determinations, and then by comparison with the molecular weight of the starting polyacrolein have some idea of the extent of the reaction. Unfortunately, the polyacrolein-deferoximine

did not form clear solutions even after filtration through sintered glass.

When polyacrolein and deferoxamine B are in equal weight, the ratio of $-CHO$ groups to $-NH_2$ groups is 10:1, thus a maximum nitrogen content of 8.4% can be obtained. The measured nitrogen content of 7.16% indicates that under these conditions PADFI is obtained with an aldehyde/amine ratio of about 14/1, and that the reaction is about 70% complete.

The IR spectrum of PADFI (Fig. 5) showed the features of both polyacrolein (Fig. 3) and deferoxamine B (Fig. 4). The $-NH_2$ band at 3320 cm^{-1} and the three $C-N$ vibration bands [7] at 1230, 1200, and 1165 cm^{-1} of deferoxamine B have disappeared, while the absorption corresponding to the $-N-C=O$ group at 1650 cm^{-1} is now present. The band at 1720 cm^{-1} corresponds to unreacted aldehyde groups. The bands in the range 900 to 1200 cm^{-1} have the same appearance as those of polyacrolein. After trituration with boiling methanol to dissolve any unreacted deferoxamine B, the IR spectrum of the PADFI was identical to that before, meaning that deferoxamine B had reacted with polyacrolein, probably through an imine, or N-acetal, or both.

Two possible structures for PADFI are presented in Fig. 6. Unfortunately it is not possible to distinguish them from the IR data, since the absorption bands for the $-C=N$ groups (1690 to 1640 cm^{-1} [21]) overlaps with that of the hydroxamic acid groups, and the band of the $-NHR$ overlaps with the hydroxyl group absorption. Since the IR shows

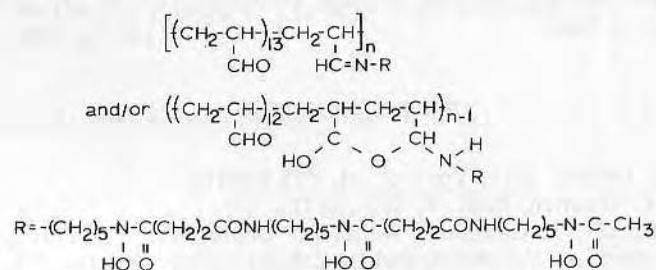


FIG. 6. Possible structures for the polyacrolein-deferoximine (PADFI) graft copolymer. The aldehyde groups may be forming cyclic hemiacetals; see text.

the presence of free aldehyde groups, they have been indicated as such in the structures of Fig. 6, but some of them may be in the form of cyclic hemiacetals, as was indicated for polyacrolein.

PADFI is insoluble in water and in common organic solvents, showing

some solubility in dimethylformamide. No change in the IR spectrum was evident after the polymer was left in contact with physiological saline solution for 24 hr at 36 to 37°C .

The iron binding capacity of PADFI was determined on samples with and without saline solution treatment by leaving them in contact with a dilute ferric chloride solution for about 20 hr. In both cases there was a decrease in the iron concentration of the solution. The 40% decrease in solution iron tends to indicate that 1) the $-NH_2$ group of deferoxamine B does not participate in the complex formation, and 2) deferoxamine B maintains its chelating affinity when attached to a polymer backbone. Polyacrolein exhibited no iron removal when tested under the same conditions.

ACKNOWLEDGMENTS

We thank Dr. Anthony Temple, Poison Control Center, University of Utah for many helpful discussions and encouragement. CIBA Pharmaceutical Co., Summit, New Jersey graciously provided samples of Desferal. Dr. Carl Rehm, CIBA Pharmaceutical Co., advised us on a number of points and has been most helpful. Professor Donald Lyman, Dr. David Lentz, and Dr. Gary Henderson, University of Utah have advised and aided us in this work. The financial support of the Universidad Católica de Chile given to R. S. Ramirez is appreciated. Portions of this work were supported by Biomedical Sciences Support Grant FR-07092 and National Science Foundation Grant GK 29382, University of Utah.

REFERENCES

- [1] J. J. Crotty, *Clin. Toxicol.*, **4**, 615 (1971).
- [2] W. F. Westlin, *Ibid.*, **4**, 597 (1971).
- [3] H. Bickel, E. Gaumann, W. Keller-Schierlein, V. Prelog, E. Vischer, A. Wettstein, and H. Zahner, *Experientia*, **16**, 129 (1960).
- [4] H. Bickel, G. E. Hall, W. Keller-Schierlein, V. Prelog, E. Vischer, and A. Wettstein, *Helv. Chim. Acta*, **43**, 2129 (1960).
- [5] H. S. Waxman and E. B. Brown, in *Progress in Hematology*, Vol. 6 (E. B. Brown and C. V. Moore, eds.), Grune and Stratton, New York, 1969.
- [6] J. C. Bailor, *Amer. Sci.*, **59**, 586 (1971).
- [7] G. Schwarzenbach and K. Schwarzenbach, *Helv. Chim. Acta*, **46**, 1390 (1963).
- [8] D. Lentz, G. Henderson, and E. Eyring, *Abstracts*, 164th American Chemical Society Meeting, New York, August 1972.

Ab-Rami 2
Polymer Drug '74

Polymer Preprints, 15 (1974) 391

POLYMER-DRUG GRAFTS FOR IRON CHELATION

by
R.S. Ramirez and J.D. Andrade
Division of Materials Science and Engineering
and
Institute for Biomedical Engineering
University of Utah, Salt Lake City, Utah 84112

INTRODUCTION

Deferoxamine B (DFA) is a chelating agent isolated from an iron-bearing metabolite of a group of natural substances, the sideramines (1,2). DFA has a strong affinity and selectivity for iron. The stability constant of the Fe(III) complex is about 10^{31} in solutions of pH from 3 to 8. This value is approximately 10^{15} times higher than the stability constants of other metallic complexes of DFA (3), and the difference is greater than for other synthetic chelating agents. The kinetics of the DFA-Fe(III) complex formation has been reported (4). Moreover, the DFA-Fe(III) complex is of relatively low molecular weight, water soluble, and excreted by the kidneys. For these reasons DFA is used in the treatment of severe acute iron poisoning in small children (5).

In most severe iron poisoning cases DFA can be applied quite successfully and with minimal side effects (5); however, both the drug and its iron complex are toxic if present in very large amounts. The use of DFA is thus dose restricted (6), and in very severe cases the maximum amount of drug which can safely be used may not be sufficient for the removal of the required amounts of iron.

The use of an extracorporeal system to remove excess iron from blood would avoid the problem of toxicity of large doses of DFA. Andrade et.al. (7) and Chang et.al. (8) have used this principle for the removal of uremic toxins and certain poisons.

The chemical structure of DFA, containing a free NH_2 group allows it to be reactive to other functional groups, such as $-\text{COCl}$, $-\text{CH}_2\text{Cl}$, $-\text{CHO}$. In a previous work we have described the synthesis of a polyacrolein-deferoximine copolymer (9) that maintained the chelation ability of DFA. In this paper we describe the synthesis and preliminary characterization of two new polymer-DFA grafts and further characterization done on a new polyacrolein-DFA system. These polymers may prove to be useful in extracorporeal systems for iron detoxification.

EXPERIMENTAL

Materials. Monomers were obtained from Polysciences, Inc. Warrington, Penna. and purified according to standard procedures (10). Polystyrene resin was Styron 678U-26-7 (M.W. ca.200,000), generously donated by Dow Chemical Co. Midland Michigan.

Polymer Synthesis.

Polyacrolein (PA).

Polyacrolein was prepared by Redox initiation (11).

Acrolein (36g) was dissolved in water (120ml) and polymerized in the presence of *tert*-butyl-hydroperoxide (0.5ml) and a 20% polyacrolein-bisulfite solution (2ml). The temperature was 60°C and the reaction time 4 days. Yield, 15g. $[\eta]$ of polyacrolein- SO_2 adduct was 0.59.

Polyacrolein-Deferoximine (PADFI).

The reaction between PA and DFA was carried out following the procedure previously described (9). A weight ratio of 2:1 of DFA to PA was used. Thus 3.9g of DFA were reacted with 1.8g

of PA in dimethylformamide (DMF). The yield was 2.8g. Elemental Analysis: C, 57.89; H, 7.46; N, 7.81%.

Poly(methacrylyl chloride-co-styrene) (PMACS).

This copolymer was prepared by reacting the monomers in equal molar ratio. Styrene (20.8g) and methacrylyl chloride (20.1g) were dissolved in CCl_4 (150ml) and the polymerization initiated with 2,2'-Azo-bis[2-methyl-propionitrile] (0.21g), in a nitrogen current. The polymer was precipitated onto petroleum ether. The yield was 13.8g. Elemental Analysis: C, 70.00; H, 6.42; Cl, 17.52%. $[\eta]$ in DMF was 0.53.

Poly(methacrylyl chloride-co-styrene) PMADFS.

The reaction between PMACS and DFA was carried out in DMF solution at 100°C. A solution of PMACS (2.96g) in DMF (50ml) was added to a solution of DFA (4.0g) in DMF (50ml) containing triethylamine (TEA) (2.15g). The polymer was precipitated onto 10% HCl solution. The yield was 4.0g. A portion of the reacted polymer was extracted with ethanol for 24 hours. Elemental Analysis: Unextracted: C, 67.29; H, 7.58; N, 6.17; Cl, 0.96%. Extracted: C, 68.76; H, 8.08; N, 6.05; Cl, 0.19%.

Chloromethylated Polystyrene (CMPS).

Polystyrene was chloromethylated in the following procedure (14). Styrene (5g) dissolved in chloromethyl methyl ether (50ml) was maintained for 4 hours at room temperature in the presence of anhydrous $ZnCl_2$ (2.5g). The polymer was precipitated onto absolute ethanol. The yield was 5.7g. The elemental analysis gave 12.56% of Cl.

Reaction between Chloromethylated Polystyrene and Deferoxamine B

DFA (5.61g) dissolved in DMF (100ml) containing TEA (3.1g) was added to CMPS (2.58g) swollen in DMF (100ml). The mixture was kept at 120°C for 16 hours. A solid polymer was present after this time. The yield was 2.1g after extracting the product with ethanol. Elemental Analysis: C, 77.99; H, 8.30; N, 4.53; Cl, 2.73%.

Iron Chelating capacity of the polymers.

Samples of the polymer-DFA grafts, placed in ethanol for 5 minutes, stayed in contact with a 2% ferric ammonium sulfate solution for 24 hours. In all cases the polymers took a red-brown color. After several washings with water and drying the analysis gave the following iron contents:

PADFI: 1.88%

PMADFS: 0.651%

CMPS-DFA: 1.29%

DISCUSSION

Polyacrolein System.

Polyacrolein was reacted with DFA in several weight ratios besides the 1:1 ratio. Ratios of PA:DFA of 1:2, 1:3, 1:4 and 1:5 were tried. Only the reaction with ratio 1:2 gave good yield in precipitated polymer. It seems that if too many DFA groups are introduced in the polymer chain the product becomes more soluble. The nitrogen content of 7.81% indicates that about 60% of the carbonyl groups have reacted with DFA when the reaction mixture had 1:2 weight ratio, and this percentage does not differ greatly from that obtained in the 1:1 weight ratio reactions previously reported (9).

Poly(methacrylyl chloride-co-styrene) System.

The copolymerization of methacrylyl chloride and styrene was carried out with a feed mole ratio of 1:1. The expected ideal repeating unit, which contains one of each monomer units, would have an empirical formula of $C_{12}H_{13}ClO$. The empirical formula for the repeating unit calculated from the elemental

analysis is $C_{16}H_{17}ClO$, meaning that there are 4C and 4H more per repeating unit. This result gives a ratio of styrene units to methacrylyl chloride units of 3 to 2 in the copolymer chains.

The reaction between PMACS and DFA was carried out in DMF solution in the presence of triethylamine to prevent the hydroxamic acid groups from reacting with acid chloride groups of the polymer. The IR spectrum of the product showed the typical carbonyl band in secondary amide at $1700cm^{-1}$ and no band in the $1770-1800cm^{-1}$ range corresponding to acid chlorides (15). The nitrogen content of 6.17% indicates that the reaction between PMACS and DFA was about 55% complete with respect to the Cl content of PMACS. When PMADFS was extracted with ethanol, the unreacted chlorine decreased from 0.96% to 0.19% while carbon and hydrogen contents increased. This shows that some of the acid chloride groups that did not react with DFA reacted with the extracting ethanol, converting them to ethyl esters groups, although most of the unreacted acid chloride groups suffer hydrolysis during the washing procedure.

Chloromethylated Polystyrene System.

Chloromethylated polystyrene was prepared using chloromethyl methyl ether and $ZnCl_2$. The reaction time was longer than the one normally used (10,14) in order to obtain a relatively high chlorine content. The percentage of chlorine of 12.56 means that about 50% of the phenyl rings had been chloromethylated. The IR spectrum of this polymer is different from that of starting polystyrene, showing a broad absorption band at $3400cm^{-1}$ corresponding to hydroxyl groups from partial hydrolysis of the chloromethyl groups. The appearance of the out of plane C-H deformation band of 2 adjacent hydrogens in aromatic rings at $850cm^{-1}$ is conclusive that a second substitution in some aromatic rings have occurred (15). The presence of strong bands at 700 and $760cm^{-1}$ shows that monosubstituted benzene rings are present in the polymer chains.

CMPS thus prepared failed to dissolve in DMF, becoming swollen when heated. The reaction with DFA was carried out in these conditions and in the presence of TEA to prevent the hydroxamic acid groups from reacting with the chloromethyl groups, since the latter are very reactive with groups that contain active hydrogens. A long reaction time, about 16 hours, was given to this reaction because of the insolubility of the polymer. The nitrogen content of 4.53% corresponds to a 40% conversion.

There was a 2.73% unreacted chlorine, which suggests that probably longer reaction time is needed for higher conversions. The IR spectrum of the CMPS-DFA graft showed a strong -OH band at $3400cm^{-1}$, that overlaps with -NH absorption, a C=O in hydroxamic acids at $1630cm^{-1}$ (15) and the characteristic bands of monosubstituted and p-substituted benzene rings at 700, 760 and $850cm^{-1}$ respectively.

Iron chelation capacity of the polymers.

Energy Dispersive Analysis of X-rays (EDAX) done on the polymer-drug grafts that were exposed to a Fe(III) solution showed the corresponding peaks for iron. Roughly CMPS-DFA graft showed the highest relative iron peak. The elemental analysis gave the highest iron content for PADFI.

CONCLUSION

Polymer-Deferoxamine B grafts that maintain the chelating ability of the drug have been prepared. The polymer-drug grafts readily form polymeric chelates when placed in contact with an Fe(III) solution. EDAX studies and elemental analysis are evidences of the complex formation.

Further experiments are being carried out to completely characterize the different polymer-drug systems and determine the rate of iron removal.

Acknowledgement. We thank Dr. Anthony Temple, Poison Control Center, University of Utah, for his encouragement in doing this work. CIBA Pharmaceutical Co., Summit, New Jersey graciously provided samples of Desferal.

Dr. Donald T. Warner, The Upjohn Co. Kalamazoo, Michigan advised and aided us with many helpful suggestions.

REFERENCES

- (1). H. Bickel, E. Gaumann, W. Keller-Schierlein, V. Prelog, E. Vischer, A. Wettstein and H. Zahner, Experimentia, **16**, 129 (1960).
- (2). H. Bickel, G. E. Hall, W. Keller-Schierlein, V. Prelog, E. Vischer, and A. Wettstein, Helv. Chim. Acta, **43**, 2129 (1960).
- (3). H. S. Waxman and E. B. Brown, in Progress in Hematology, Vol. 6, edited by E. B. Brown and C. V. Moore, Grune and Stratton, New York, 1969.
- (4). D. J. Lentz, G. Henderson, and E. M. Eyring, Molecular Pharmacol., **2**, 514 (1973).
- (5). W. F. Westlin, Clin. Toxicol., **4**, 597 (1971).
- (6). J. T. McEnery, Clin. Toxicol., **4**, 603 (1971).
- (7). J. D. Andrade, K. Kunitomo, R. Van Wagenen, B. Kastagir, D. Gough, and W. J. Kolff, Trans. Amer. Soc. Artif. Int. Organs, **17**, 222 (1971).
- (8). T. M. S. Chang, J. P. Coffey, C. Lister, E. Taroy, and A. Stark, Trans. Amer. Soc. Artif. Int. Organs, **19**, 87 (1973).
- (9). R. S. Ramirez and J. D. Andrade, J. Macromol. Sci. - Chem., **A7**, 1035 (1973).
- (10). D. Brown, H. Cherdron and W. Kern, Techniques of Polymer Synthesis and Characterization, Wiley - Interscience, New York, 1972.
- (11). E. E. Ryder, Jr. and P. Pezzaglia, J. Polymer Sci., Part A **3**, 3459 (1965).
- (12). E. E. Siebert, J. Polymer Sci., Part C, **8**, 87 (1965).
- (13). R. C. Schulz, in Vinyl Polymerization, Vol. 1, Part I (G. E. Ham, ed.) Dekker, New York, 1967, Chap. 7.
- (14). D. T. Warner, The Upjohn Company, Kalamazoo, Michigan, personal communication, September 1973.
- (15). L. J. Bellamy, The Infrared Spectra of Complex Molecules, Methuen and Co., Ltd, and J. Wiley and Sons, New York, 1958.

last page

168. G. T. Tucker, R. M. Boyes, P. O. Bridenbaugh, and D. C. Moore, Anesthesiology, **33**, 287 (1970).
169. L. E. Mather, G. J. Long, and J. Thomas, J. Pharm. Pharmacol., **23**, 359 (1971).
170. G. D. Olsen, Science, **176**, 525 (1972).
171. R. C. Schulz, R. Hollander, and W. Kern, Makromol. Chem., **40**, 16 (1960).
172. R. S. Ramirez and J. D. Andrade, Unpublished Results.
173. O. Zaborsky, Immobilized Enzymes, CRC Press, Cleveland, 1973.
174. K. W. Pepper, H. M. Paisley, and M. A. Young, J. Chem. Soc., **1953**, 4097.
175. Amberlite XAD-2 Technical Bulletin, Ion Exchange Department, Rohm and Haas Co., Philadelphia, July 1971.
176. Preliminary Technical Notes. Amberlite XAD-4, Rohm and Haas Co., Philadelphia, July 1971.
177. E. E. Ryder and P. Pezzaglia, J. Polym. Sci., **A3** 3459 (1965).
178. R. C. Schulz, "Polymerization of Acrolein," in Vinyl Polymerization, Part 1 (G. E. Ham ed.), Dekker, New York, 1967, p. 403.
179. R. C. Schulz, K. Meyersen, and W. Kern, Makromol. Chem., **54**, 156 (1962); **59**, 123 (1962).
180. Styron 678-U, Dow Chemical Co., Midland, Michigan.
181. D. Brown, H. Cherdon, and W. Kern, Techniques of Polymer Synthesis and Characterization, Wiley-Interscience, New York, 1972.
182. D. T. Warner, The Upjohn Company, Kalamazoo, Michigan, Person Communication.
183. Gailbraith Laboratories, Knoxville, Tennessee.
184. EDAX Peak Identification Chart, EDAX Laboratories, EDAX International Inc., Raleigh, North Carolina.

POLYMER-DRUG GRAFTS FOR IRON CHELATION

Rene S. Ramirez and Joseph D. Andrade

Department of Materials Science and Engineering
University of Utah
Salt Lake City, Utah 84112

INTRODUCTION

Accidental poisonings account for a large proportion of children's accidents. There is a need to improve the emergency treatment of poisonings, particularly to decrease the period of coma and to minimize mortality.

Iron poisoning is a common cause of poisoning among young children. Use of chelating agents, especially Deferoxamine B, to remove excess iron from the body is one of the most effective treatments. However, in very severe cases of acute iron overloads, the amount of deferoxamine required to remove the iron is so high that the drug and its iron chelate would be toxic.

Our objective is to develop a chelating polymer which could be used in extracorporeal detoxification of severe acute iron poisoning cases.

POLYMER CHELATESIon-Specific Resins

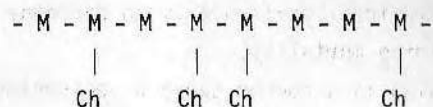
In the search for specific ion-exchange resins there has been a great deal of effort toward the synthesis of specific chelating

or complexing resins. The commercial manufacture of these resins has not yet been successful¹ with the exception of Dowex A-1².

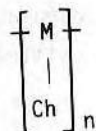
Polymer chelates consist of a polymer backbone and a grafted chelating group (Fig. 1a) although resins containing the chelating group as part of the repeat unit have been reported³⁻¹¹ (Fig. 1b). Resins of the first type may be considered as random graft copolymers and those of the second type as homopolymers.

Chelating resins differ from ion exchange resins in three properties⁹: greater selectivity, higher metal-polymer interaction energy, and slower kinetics.

Applications of chelating resins have been mainly in water purification (i.e., removal of heavy metals from water), analytical determination of metal ions, chromatographic separation of ions,



(a)



(b)

Fig. 1. General structure of polymer chelates. M = repeat unit; Ch = chelating group. (a) The chelating group is grafted on the polymer chain. (b) The chelating group is part of the monomer unit.

and recovery of metals from solutions. A number of chelating groups have been grafted onto polymers (Table I).

Synthesis of Polymer Chelates

There exist two general approaches for the synthesis of chelating polymers. One is the incorporation of the active (chelating) group in the polymer matrix by making use of reactive functional groups in the polymer. The second method is the transformation of the active group into a monomer with subsequent polymerization. In the first method the hydrophilicity of the chelating groups is sometimes incompatible with the polymer matrix (usually hydrophobic), and therefore the latter requires some modification. In the second method the presence of a larger group in a monomer may reduce and even prevent homopolymerization, making it necessary to copolymerize the transformed monomer. It is possible that some bulky chelating monomers may not polymerize or copolymerize at all.

Gregor et al.³⁸ suggested four conditions that the chelating group should fulfill:

1. It should be able to react with a group and become attached to the polymer matrix, or be able to polymerize for resin formation.

TABLE I
Some Chelating Groups Grafted on Polymers

CHELATING GROUP	REFERENCES
Alpha-Amino acids	13-19
Iminodiacetic and/or Iminodipropionic acids	5, 7, 14, 15, 20-34, 36
Nitrilotriacetic acid	35-37
EDTA	37-39
Hydroxamic acid	40-42
Deferoxamine B	43
8-Hydroxyquinoline	44-47
Others	3, 8, 37, 48-80

2. If the latter is the case, it should be sufficiently stable to withstand the polymerization process without alteration of its chelating function.

3. The chelating group should be compact so as not to be sterically hindered by the polymer matrix.

4. The arms of the chelate structure should be present on the same monomer unit in proper spatial configuration, for preservation of specific arrangement of the ligand.

D'Alleia et al.²⁸ suggest that monomeric models for the chelating polymer should be constructed, and that for an effective chelating polymer the behavior of the active group in the polymer should be similar to that of the group in the monomeric segment. They proposed the following approach for the synthesis of a chelating polymer:

1. Synthesis and determination of chelating characteristics of a model monomeric compound.

2. Synthesis and characterization of an oligomer of low molecular weight (dimer, trimer, etc.) model compound, and determination of its chelating properties.

3. When the results of the second step confirm chelation, a high molecular weight polymer should be synthesized and characterized, and its chelation capacity should be determined.

D'Alleio et al.^{28,29,31-33} have followed this approach for the study of chelating polymers containing hydroxyarylaminoacetate groups as the chelating group.

A general sequence for the synthesis of grafted chelating polymers is shown in Fig. 2. In this case, polystyrene (1), usually cross-linked with divinylbenzene, is first chloromethylated, then transformed into a sulfonium salt (3), and finally reacted with sodium iminodiacetate to give the chelating polymer (4). The sulfonium salt is hydrophylic whereas the chloromethylated resin (2) is not and will not react appreciably with iminodiacetate salt.

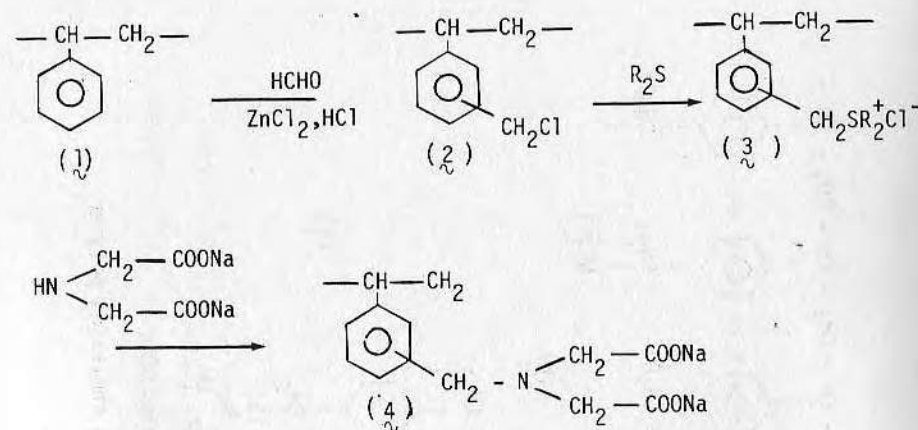


Fig. 2. Reaction sequence for the synthesis of an iminodiacetate chelating polymer¹.

Another approach to solve the problem of hydrophobicity of the chloromethylated polystyrene is to partially transform it into a quaternary salt with a tertiary amine (e.g., triethylamine), which makes the polymer more hydrophylic, and then to react it with the chelating group⁸¹. The reaction sequence for this process is shown in Fig. 3.

The transformation of the chelating group into a monomeric species is shown in Fig. 4²⁶. In this case methacrylchloride (8) reacts with the diethyl ester of iminodiacetic acid to give amide (9), which may be homopolymerized to give (10). Monomer (9) may also be copolymerized with other vinyl monomers⁹ or graft copolymerized with radiation on preformed polymers⁹ or fibers to produce chelating graft copolymers.

Distribution Coefficient and Selectivity Coefficient of a Chelating Resin

The distribution coefficient, K_D , or distribution ratio, and the selectivity coefficient, $K_{A/B}$, or concentration quotient⁸³,

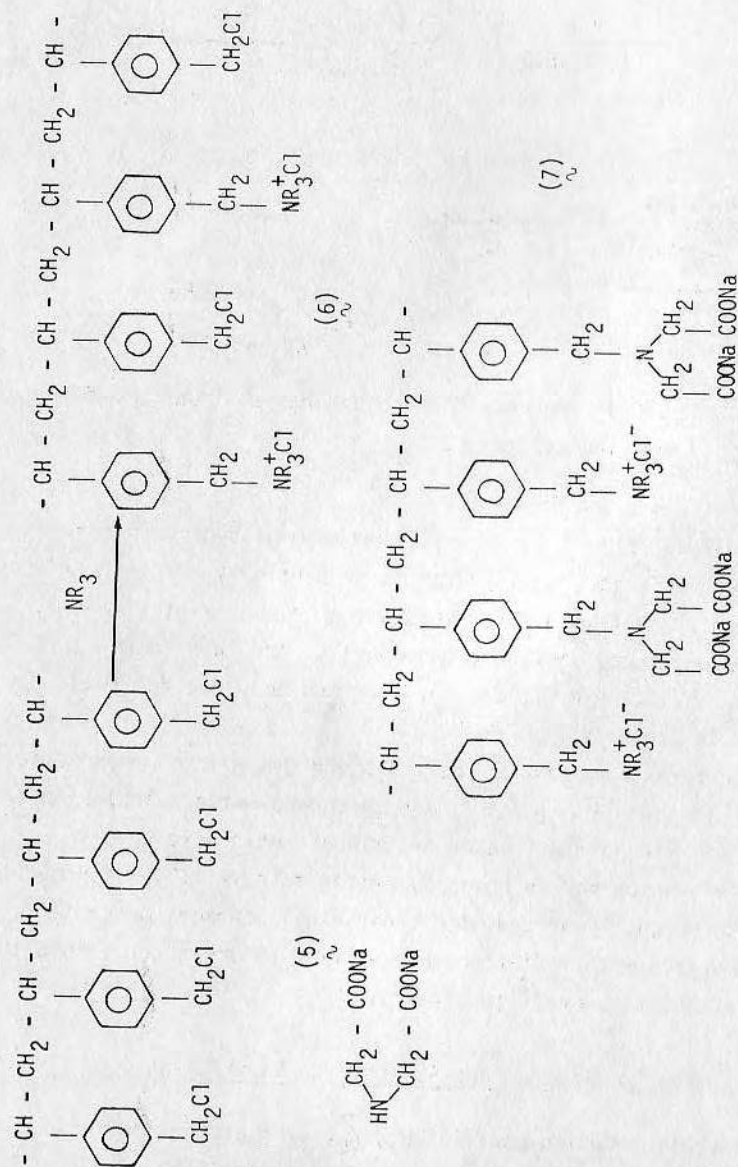


Fig. 3. Reaction sequence for the synthesis of a chelating polymer with partial substitution.

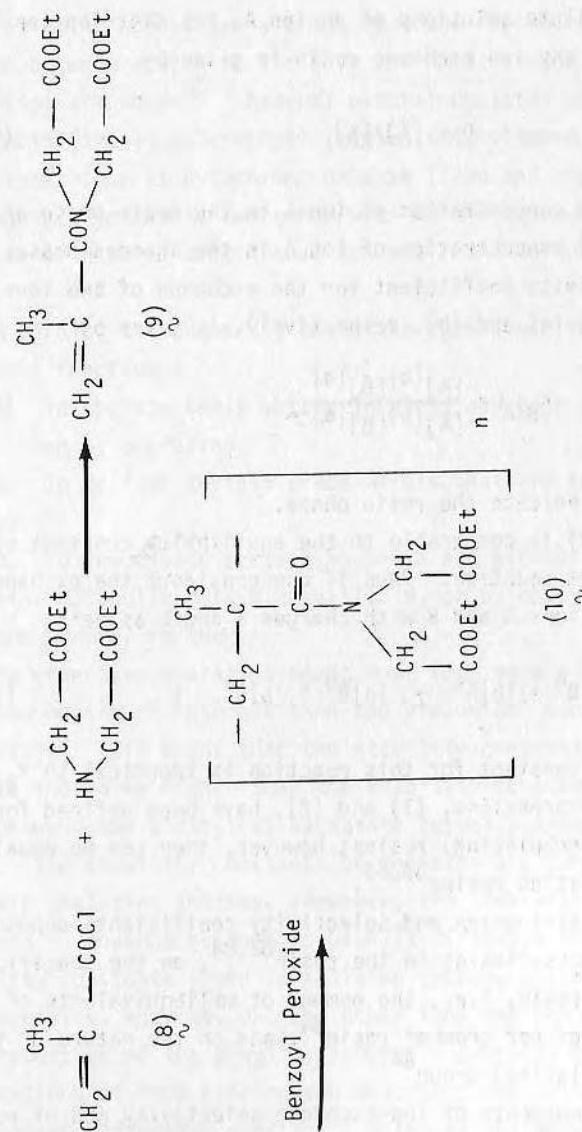


Fig. 4. Synthesis of a chelating polymer with one active group per monomer unit.

are important parameters in the characterization of ion-exchange and chelating resins.

For very dilute solutions of an ion A, the distribution coefficient for any ion exchange resin is given by

$$D = [\bar{A}]/[A] \quad (1)$$

where $[\bar{A}]$ is the concentration of ion A in the resin phase and $[A]$ is the concentration of ion A in the aqueous phase.

The selectivity coefficient for the exchange of two ions, A and B, of charge $|a|$ and $|b|$, respectively, is given by

$$K_{B/A} = \frac{[\bar{A}]^{|b|} [\bar{B}]^{|a|}}{[\bar{B}]^{|b|} [\bar{A}]^{|a|}} \quad (2)$$

where the bars indicate the resin phase.

Equation (2) is comparable to the equilibrium constant of an ionic equilibrium reaction. Thus if one considers the exchange reaction of two ions A and B with charges a and b as being



the equilibrium constant for this reaction is identical to $K_{B/A}$.

These two expressions, (1) and (2), have been defined for ion-exchange (nonchelating) resins; however, they can be equally applied for chelating resins^{33,83}.

Both the distribution and selectivity coefficients depend on the degree of cross-linking in the resin^{82,84}, on the specific capacity of the resin, i.e., the number of milliequivalents of fixed exchange groupings per gram of resin⁸⁴, and on the nature of the exchange (or chelating) group⁸⁴.

Detailed treatments of ion-exchange selectivity and of resin selectivity in aqueous solutions are given by Reichenberg⁸⁴ and by Diamond and Whitney⁸².

CHELATING AGENTS IN MEDICINE

Chelating agents are a class of drugs for which a clear connection between action in the body and physical and chemical properties are known⁸⁵. Several natural chelates are well known: hemoglobin (iron), chlorophyll (magnesium), vitamin B-12 (cobalt), and enzymes such as cytochrome oxidase (iron and copper). This section will be mainly concerned with synthetic chelating agents or those of natural origin that are not found in the human organism.

According to Schuber⁸⁵, chelating agents may accomplish three different functions:

1. To chelate toxic metals in blood and help the body get rid of them by excretion.
2. To deliver certain trace metals that are essential to tissues.
3. To inactivate certain bacteria and viruses by making essential metabolic metals unavailable, or by delivering metals that are harmful to them.

An effective chelating agent must form more stable complexes with the metals of interest than the biological substance holding the metals. This means that the stability constant of the metal chelate should be higher than the stability constant of the complex between the biological substance (usually proteins) and the metal. The stability constants of chelates are taken as a measure of their chelating ability. However, the stability constant determined in aqueous systems is usually different from the actual stability constants found in a living system, where interferences from proteins, enzymes, pH, and other ions may change the chelating properties of the drug⁸⁶. Shubert⁸⁷ examined the biological implications of iron binding and described chelating agents in terms of an "effective constant", which is not actually constant but varies with the media in which the chelating agent and the metal ion are in contact.

An important property that the chelating agent should have is selectivity. It should be able to chelate the metal of interest without influencing the other essential ions present, often in larger amounts, such as Ca and Mg, as well as the trace metals, such as Zn, Mn, and Cu, whose removal could be dangerous.

Solubility of both the chelating agent and the complex in various media are important. They should be water soluble, to permeate within the intra- and extravascular spaces but this may exclude them from penetrating into the intracellular space. Water solubility also allows a more rapid excretion of the drug and its chelate.

Chelating agents used as drugs should withstand metabolic processes, and if they undergo enzymatic or other degradation, the metabolites should not have toxic side effects⁸⁶.

The administration mode of a chelating agent is also very important. For example, EDTA and DTPA (see Table 2 for formulas and chemical names) must be administered by prolonged intravenous infusions, and temporarily immobilize the patient thus restricting their use to hospitals⁸⁶. An ideal chelating agent as a drug would be one that is taken orally, acts in the gastrointestinal tract, and is absorbed through the intestines, extending its action to the rest of the body⁸⁸.

Table 2 summarizes various chelating agents used in medicine. Some of these agents are still in the experimental stage, whereas others are presently being used for clinical treatment. Some of these chelating agents are used to remove metals from the organism (EDTA, DTPA, deferoxamine, BAL, etc.). Others are used to deliver metals into infected areas (Oxine) or to the brain to reduce fever and headaches (aspirin)⁸⁵.

One of the main uses of chelating agents in medicine has been in the treatment of acute metal poisoning, such as lead, mercury, and iron. The most success has been in the case of iron poisoning where DTPA and especially deferoxamine have proven very effective.

ACUTE IRON POISONING

Occurrence of Iron Poisoning

Young children may ingest large amounts of iron tablets (commonly ferrous sulfate) that are prescribed for their mothers. Adults less often take ferrous sulfate in suicide attempts. The estimated lethal dose of ferrous sulfate in children is 900 mg/kg of body weight⁹⁰. Some children have survived after ingesting 15 g, and sometimes as little as 1 g has been fatal⁹¹. Aréna⁹² stated that the average human fatal dose is 200 to 250 mg of iron per kilogram of body weight. For the average 2 year-old child, that dose means the ingestion of 3 g of iron.

Crotty⁹³ has summarized reports from the National Clearinghouse for Poison Control Centers over a period of 32 months. Of 292,060 poisoning reports, 1194 cases were of ingestion of medicinal preparations containing more than 65 mg of iron. Of these cases, 1024 were children under 5 years of age, and ferrous sulfate ranked 6th among the medicines that caused hospitalization of children under 5. According to Crotty⁹³, "the reported information that 179 of 654 cases (27%) were hospitalized places iron salts in the category of the most toxic substances." This is probably because of the consideration of iron as a "vitamin" and not as a potential poison; thus parents do not take the necessary precautions.

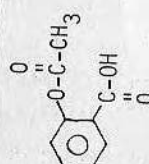
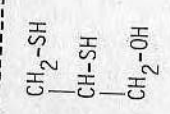
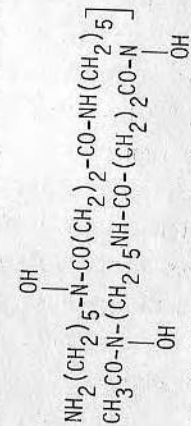
Until 1958, Aldrich⁹⁴ estimated the mortality rate of acute iron intoxication as 45%. Whitten et al.,⁹⁵ in 1965 proposed that mortality rates may be reduced with the appropriate therapy using deferoxamine as a chelating agent for iron.

Mechanism for Iron Toxicity from Iron Salt Ingestion

Iron overdoses are accompanied by both local and systematic effects. Significant amounts of either ferric or ferrous salts lead to rapid necrosis of the mucosa of the gastrointestinal tract⁹⁶. Absorbed iron soon exceeds the bonding capacity of iron

Table 2

Some chelating agents used in medicine 85,86

Name	Formula and Chemical Name	Uses
Aspirin	 <p>o-Acetylsalicylic acid</p>	To reduce fever and relief of headache, muscle and joint pain. Also for symptoms of rheumatic fever.
BAL (British Anti-Lewisite)	 <p>2,3-Dimercaptopropanol</p>	In cases of arsenic, antimony, mercury, and gold poisoning. Also in lead poisoning.
Deferoxamine B (DFA)	 <p>N-[5-[3-[(5-aminopentyl)hydroxycarbonyl]-propionamido]pentyl]-3-[[5-(N-hydroxyacetamido)-pentyl]carbonyl]-propionohydroxamic acid</p>	In iron poisoning cases.

RAMIREZ AND ANDRADE

POLYMER-DRUG GRAFTS FOR IRON CHELATION

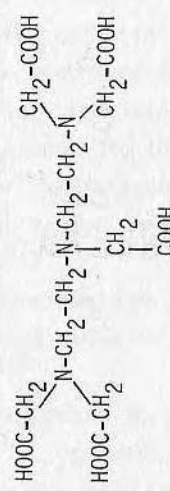
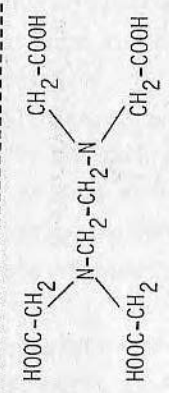
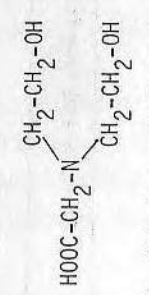
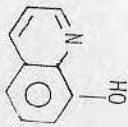
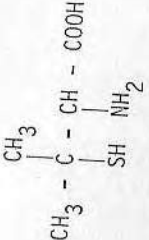
Name	Formula and Chemical Name	Uses
DTPA	 <p>Diethylenetriaminepentaacetic acid</p>	In poisoning by radioactive metals and in iron poisoning.
EDTA	 <p>Ethylenediaminetetraacetic acid</p>	In cases of lead poisoning. Treatment of skin irritation by metals. In treatment of atherosclerosis.
Fe-3 Specific (DHEG)	 <p>N,N-Dihydroxyethylglycine</p>	In iron poisoning.

Table 2 (concluded)

Name	Formula and Chemical Name	Uses
Oxine	 8-Hydroxyquinoline	Used for its antibacterial action.
Penicillamine	 2-Amino-3-mercapto-3-methyl butanoic acid	In cases of copper overloads (Wilson disease) and in lead poisoning. Inhibits tumor growth in mice.

proteins in blood; thus serum iron concentration increases rapidly. The liver and the spleen remove sizeable amounts of iron, and this often results in hepatic necrosis⁹⁷. Witzleben and Buck⁸⁹ proposed a hypothesis involving indirect lipid peroxidation. In the liver and elsewhere at the cellular level, iron is a potent protoplasmic poison due to its enzymatic impact⁹⁸. However, the biochemical mechanism of iron toxicity has not yet been well established.

Symptoms of Iron Poisoning

Symptoms of iron poisoning begin with vomiting, usually accompanied by abdominal pain and diarrhea, and followed by lethargy and a state of shock⁹⁶. Shock is attributed to hemorrhage and fluid loss from the necrotizing action of iron on the gastrointestinal tract⁹⁹.

Vasomotor collapse is explained by Smith¹⁰⁰ as produced by an excessive amount of ferritin formed from apoferritin in the mucosal cells. Ferritin, considered to be a vasodepressant¹⁰¹, is then released into the circulation, initiating and maintaining the state of cardiovascular collapse.

Hepatic damage, although it has been found in some fatal human cases^{97,100,102-105} and in some experimental studies^{97,106}, cannot be attributed as a causative factor in death from acute iron poisoning since no evidence of hepatic failure has been identified¹⁰⁴.

Other symptoms include coagulation defects reported in some cases^{105,107}. However, no systematic study of the various clotting factors has been reported in humans¹⁰⁴. Experimental iron poisoning has shown prolongation of clotting time or complete absence of coagulation in rabbits¹⁰⁸. Whitten¹⁰⁹ found alteration in the different stages of blood coagulation but the clotting time was not altered.

Metabolic acidosis in experimental iron poisoning is well known, and this is probably a common occurrence in lethal iron

poisoning in children¹⁰⁴. Metabolic acidosis may be explained by two factors: (1) The release of hydrogen ions from the conversion of iron(II) and iron(III) into the circulatory system¹¹⁰ and (2) the accumulation of lactic and citric acid from anerobic metabolism characteristic of shock^{110,111}.

Shock and coma are characteristic of all the fatal cases of acute iron intoxication reported until 1965⁹⁵.

Serum iron levels greatly increase in iron poisoning, and they are usually a measure of the degree of intoxication. Normal serum iron levels in humans fluctuate between 60 to 160 µg/100 ml of blood. In acute iron poisoning, serum iron levels cover a wide range from 200 to 5000 µg/100 ml, although one case with serum iron of 30,494 µg has been reported¹¹². Iron levels of 500 to 1000 µg/100 ml are considered dangerous, and above this range the iron level is potentially lethal.

Treatment of Acute Iron Poisoning

Emergency treatment of acute iron poisoning is described by many authors^{92,96,113,114,116,117}. In general, the treatment consists of induction of vomiting with an emetic, stomach lavage with sodium bicarbonate, intravenous fluid therapy (blood or plasma) to correct acidosis and dehydration, use of a chelating agent (Deferoxamine B) to remove "free iron" and peritoneal or hemo dialysis to help the removal of chelated ironn.

Waxman and Brown⁸⁶ have an excellent review of the various chelating agents that have been employed in iron overloads. The emphasis has been on deferoxamine though DTPA has also been evaluated¹¹⁸⁻¹²². Since its introduction in 1960¹²³, at least 700 papers have described different aspects of the application of deferoxamine.

DEFEROXAMINE B IN IRON POISONING

The major objective in the treatment of poisoning with most substances is the removal of the toxic substance from the organism.

The human body is not provided with an effective mechanism for eliminating excess iron. Therefore, in acute iron intoxication only two ways of increasing iron excretion exist: phlebotomy and the use of a chelating agent¹²⁴.

One of the most specific and irreversible of the iron chelating agents is deferoxamine B, commercially available as the methane sulfonate salt. This derivative of deferoxamine is produced by CIBA under the brand name of Desferal. (Trademark, CIBA Pharmaceutical Co. Summit, New Jersey).

The high solubility of the iron complex of deferoxamine and its low molecular weight allow it to pass easily through the kidneys, making deferoxamine of great value in the treatment of acute iron poisoning.

Deferoxamine was initially proposed by Moeschlin and Schnider¹²⁵ as a two-fold approach for the treatment of acute iron intoxication: externally and parenterally. Moeschlin et al.²⁶ showed in animal experiments that the survival rate can be greatly increased by the use of deferoxamine.

More recently, several authors^{86,95,112,113,115,124,127,128} have reviewed the clinical use of deferoxamine in acute iron overloads, and the question arises whether deferoxamine should be used orally at all since it is only slightly absorbed from the gastrointestinal tract¹²⁹. Oral deferoxamine would help to remove any iron that may still be in the intestines. However, more effective methods, such as use of emetics and lavage, exist for the evacuation of the gastrointestinal tract¹²⁸. Westlin¹¹² states that intramuscular deferoxamine is preferable to avoid drug-induced hypotension and recommends that the intravenous route be used for severely intoxicated patents that are in coma or cardiovascular collapse.

Rapid infusion of deferoxamine has been reported to induce hypotension and tachycardia in dogs, cats, rabbits¹³⁰, and children^{95,112}. Whitten et al.^{95,114} studied the toxicity of the iron-deferoxamine complex in children and dogs. Rapid intravenous

administration of 30 mg/kg of the complex produced a fall in mean arterial blood pressure in children. They gave a lethal dose of 225 mg/kg of iron-deferoxamine complex to dogs, which resulted in a fall of blood pressure, a decrease in hematocrit, a decrease of blood pH, and the development of renal shutdown.

These side effects of deferoxamine and its iron complex restricted the drug dose. An intramuscular dose¹³¹ can be given to patients not in shock (1g initial administration followed by 0.5 g every 4 hours, with the total amount not to exceed 6 g in 24 hours. The intravenous dose¹³¹ recommended for patients in a state of cardiovascular collapse should not exceed 15 mg/kg/hour by slow infusion, and a total dose of 6 g in 24 hours⁸⁶.

In summary, deferoxamine is very useful in the treatment of acute iron poisoning as shown by the reduction of mortality reported by several authors^{95,124,128}. However, delayed therapy with deferoxamine did not reduce mortality in several cases of iron overloads^{117,132,133}. Therefore, McEnery¹¹⁷ recommends to "treat all cases of acute iron ingestion vigorously with deferoxamine." However, there is evidence^{95,114} that deferoxamine and its iron complex are toxic when the drug is used in large amounts. The use of an extracorporeal system containing immobilized deferoxamine may prove to be useful in the treatment of very severe acute iron intoxication.

EXTRACORPOREAL TREATMENT OF ACUTE IRON POISONING

Deferoxamine may be covalently bonded to polymers containing reactive functional groups⁴³. These polymers act as solid supports for the drug, which maintain its chelation ability. A number of investigators^{134,135} have used an extracorporeal system based on activated carbon for the removal of certain uremic toxins and other poisons such as salicylates and barbiturates. Blood is perfused through a chamber containing the solid sorbent which removes the toxin from blood. In the case of iron poisoning, the excess iron

in blood would be complexed by the immobilized deferoxamine. Then neither the drug nor its iron complex would be released into the circulatory system, avoiding the problem of toxicity of large doses of deferoxamine.

This procedure would not replace the present use of soluble deferoxamine. Instead, it would help the soluble drug in removing iron from blood in those cases of very high serum iron levels.

DEFEROXAMINE B. ORIGIN AND CHEMISTRY

Deferoxamine B is isolated from feroxamine B, an iron-bearing metabolite belonging to sideramines obtained from *Streptomyces Pilosus*^{123,136,137}. The trivalent iron in feroxamine B is removed by chemical means¹³⁸, yielding deferoxamine.

The molecule of deferoxamine is composed of one residue of acetic acid, two residues of succinic acid, and three residues of 1-amino-5-hydroxylaminopentane, as shown in Fig. 5. The residues altogether form a trihydroxamic acid with a free amino group at one end of the molecule. This amino group gives its basic character to the molecule and allows it to react with acids (inorganic and organic) and acid derivatives (acyl chlorides and anhydrides) to form salts and amide derivatives, respectively¹³⁹.

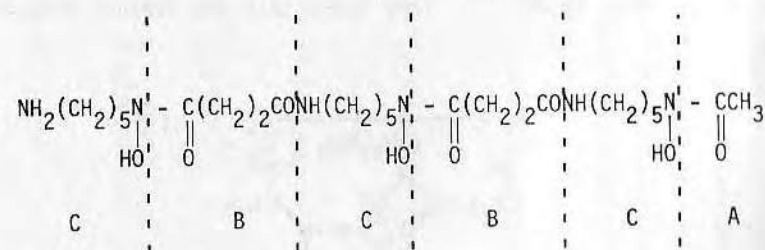


Fig. 5. Deferoxamine B, where A is acetic acid residue, B is succinic acid residue, and C is 1-amino-5-hydroxylaminopentane residue.

Deferoxamine B reacts stoichiometrically with Fe(III) to form feroxamine B, an octahedral iron complex, shown in Fig. 6. The ferric ion becomes attached to the three hydroxamic acid groups. The organic material surrounding the iron confers great stability to the complex¹²⁹.

The stability constant of the complex is of the order of 10^{31} in aqueous solutions ranging from pH 3 to pH 8. This value is at least 15 powers of 10 greater than for other complexes of deferoxamine and also greater than for other common chelating agents. Values of the stability constants for the complexes of various ions and chelating agents are given in Table 3.

Keberle¹²⁹ reported the effect of deferoxamine on the iron proteins ferritin, hemosiderin, transferrin, and hemoglobin. He found that deferoxamine removes iron from ferritin and hemosiderin until its maximum binding capacity is attained. He found, however, that deferoxamine removed only 10 to 15% of iron from saturated transferrin, and found no exchange from feroxamine to transferrin, showing that deferoxamine does not take up all the iron from transferrin under equilibrium conditions. These results are in disagreement with Bailar's conclusions¹⁴. He said that deferoxamine "is able to extract iron from nearly all of the tissues of the body, but not from transferrin or ferritin."

The kinetics of iron complexation of deferoxamine has been studied by Lentz et al.¹⁴². They found that the overall second-

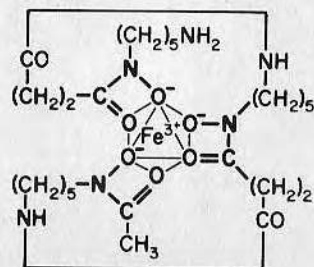


Fig. 6. Feroxamine B (also called ferrioxamine B).

TABLE III
Stability Constants for Some Metallic Complexes 86, 129, 140

Metallic Ion	Deferoxamine B (DFA)	EDTA (a)	DTPA (b)	HEDTA (c)	EDDA (d)	Fe-3-Specific (e)
Fe(III)	10^{31}	10^{25}	10^{29}	10^{20}	10^{32}	10^{30}
Fe(II)	10^{10}	10^{14}	10^{17}	10^{12}	-	10^4
Mg(II)	10^4	10^9	10^9	10^5	10^8	10
Ca(II)	10^2	10^{11}	10^{10}	10^8	10^7	-
Sr(II)	10	10^9	10^{11}	-	-	-
Co(II)	10^{11}	10^{16}	10^{19}	-	-	-
Ni(II)	10^{10}	10^{19}	10^{20}	-	-	-
Cu(II)	10^{14}	10^{19}	10^{21}	10^{17}	10^{16}	10^8
Cd(II)	10^8	10^{16}	-	-	-	-
Zn(II)	10^{11}	10^{16}	10^{18}	10^{14}	10^9	10^5

- a Ethylenediaminetetraacetic acid
- b Diethylenetriaminepentaacetic acid
- c Hydroxyethylethylenediaminetriacetic acid
- d Ethylenediamine-bis(o-hydroxyphenylacetic acid)
- e Bis-(hydroxyethyl)-glycine

POLYMERIC SUPPORTS FOR DEFEROXAMINE

The chemical structure of deferoxamine, which contains a primary amino group, allows it to react with other functional groups, such as chloroformyl ($-\text{COCl}$), benzyl chloride, and aldehyde ($-\text{CHO}$). Polymers and copolymers containing such functional groups were studied and the rationale for the selection of the various polymers is discussed.

Polyacrolein

In a previous paper we reported the synthesis of a polyacrolein-deferoxamine copolymer for potential use in the extracorporeal treatment of iron poisoning⁴³. Polyacrolein was selected because the aldehyde groups of the polymer react with amines in neutral or slightly basic solvents to form Schiff's bases¹⁷¹, while they do not react with hydroxamic acid groups, also present in the deferoxamine molecule, under these conditions.

Copolymers of Acrylyl Chloride and Methacrylyl Chloride with Styrene

Our interest in the poly(acid chlorides) is because of the high reactivity of these polymers which makes it possible to transform them into many polymeric derivatives. Copolymers are similarly useful because inclusion of only a small percent of acid chloride in a polymer chain provides sites which can be used for the attachment of grafts.

The inclusion of styrene as comonomer of the acid chloride is based on the hydrophobicity of styrene groups that renders the polymeric-deferoxamide insoluble in aqueous media. If homopoly (acid chlorides) are used and reacted with deferoxamine, a completely water-soluble system is obtained¹⁷².

Terpolymers of Methacrylyl Chloride, Vinyl Pyrrolidone, and Styrene

To allow a more open structure for easier access of the ferric ions into the chelating sites, a swellable network is

necessary. We expected that by introducing vinyl pyrrolidone units into the polymer chains we would obtain a more hydrophilic, swellable (but not soluble) polymer. Styrene was included to provide the hydrophobicity necessary to prevent complete solubility.

Chloromethylated Polystyrene

Chloromethylated polystyrene is very commonly used as a support for the immobilization of enzymes¹⁷³ and for the preparation of ion-exchange resins¹. The chlorobenzyl groups are very reactive with other groups containing active hydrogens, such as amine and hydroxyl groups¹⁷⁴. Thus the low molecular weight analog, benzyl chloride, reacts with primary amines to form secondary amines, the polymer reacting in a similar way.

The bond that is formed in the reaction of chlorobenzyl and primary amine groups is very stable to hydrolysis. Therefore, if deferoxamine were reacted with chloromethylated polystyrene, the drug would not be released from the polymer even in conditions more severe than those found in blood.

Chloromethylated Amberlites

Amberlites XAD-2 and XAD-4, trademark of Rohm and Haas Company, Philadelphia, Pennsylvania 19105, are divinylbenzene cross-linked polystyrene resins available as porous beads^{175,176}. The presence of styrene groups and the relatively high surface area of these beads allow them to be chloromethylated and aminated. Deferoxamine may be attached to the beads since the size of the pores is greater than the size of the deferoxamine molecule. This would allow us to prepare chelating resins without disturbing the scope of the beads and without having to fabricate the polymers into an appropriate physical form that would permit a good perfusion of blood.

EXPERIMENTAL RESULTS

SYNTHESIS OF POLYMER-DEFEROXAMINE GRAFTS

The reaction between the polymers or copolymers with deferoxamine utilized N,N-dimethylformamide (DMF) as solvent and triethylamine (TEA) as basic catalyst in order to prevent reaction of the hydroxamic acid groups with functional groups of the polymers. With the exception of the chloromethylated polystyrene-based polymers, they were soluble in DMF at the temperature of the reaction, 100-110°C.

Polyacrolein-Deferoxamine (VIII)⁴³

Polyacrolein (I), prepared by free radical redox polymerization of acrolein¹⁷⁷, contains free aldehyde groups, hydrated aldehyde groups, and cyclic hemiacetal groups¹⁷⁸, all of which may react with an amine^{171,179}. This is shown in Fig. 7, where after the reaction with a primary amine three types of groups may be found: azomethine, N-acetal, and tetrahydropyran. Thus, in the reaction of polyacrolein and deferoxamine all the possible structures may be found. Table 4 shows the yield and elemental analysis of the various polymer-deferoxamine grafts. The IR spectra of polyacrolein and polyacrolein-deferoxamine graft (VIII) are given in Fig. 8.

Poly(acrylyl chloride-co-styrene)-Deferoxamine (IX) and Poly(methacrylyl chloride-co-styrene)-Deferoxamine (X)

The poly(acid chloride-co-styrene) copolymers were synthesized using a comonomer feed mole ratio of 1:1. The copolymer of acrylyl chloride and styrene (II) showed more styrene units than acid chloride units, as shown in Table 4. The reaction between the copolymers and deferoxamine proceeds with the formation of an amide linkage between the acid chloride group and the amine group of the drug, as shown in Fig. 9.

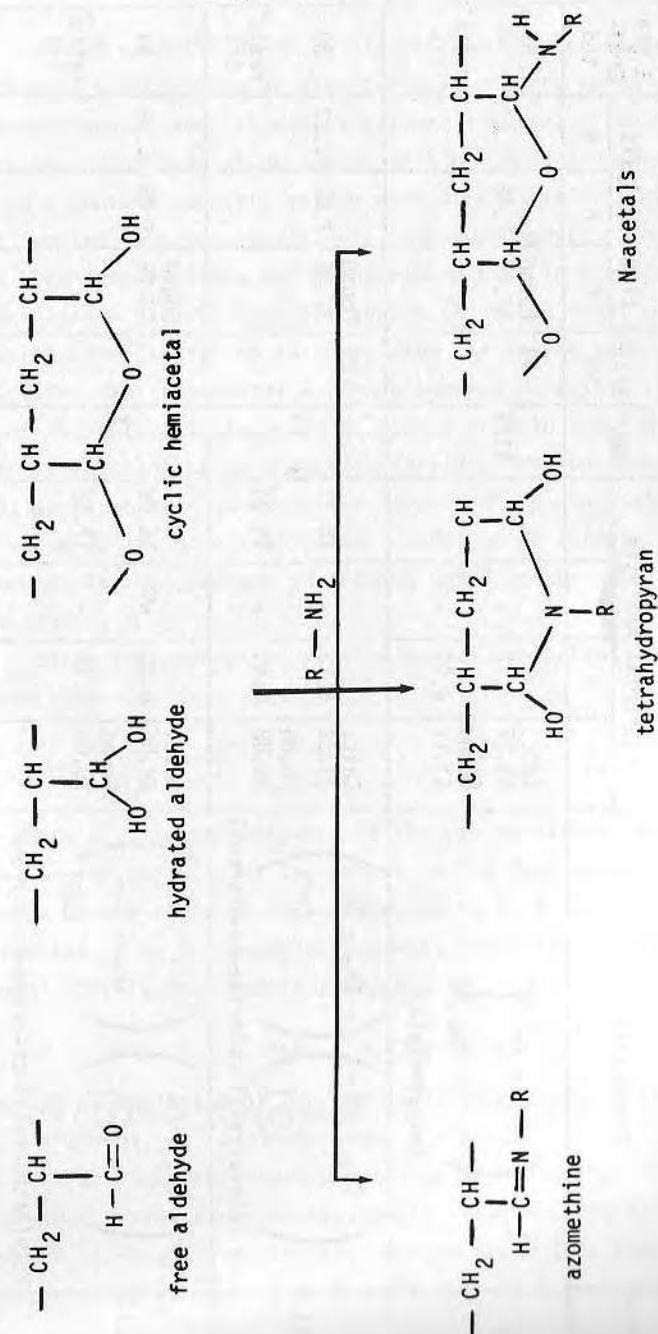


Fig. 7. Functional groups of polyacrolein and their reaction with an amine¹⁷⁸.

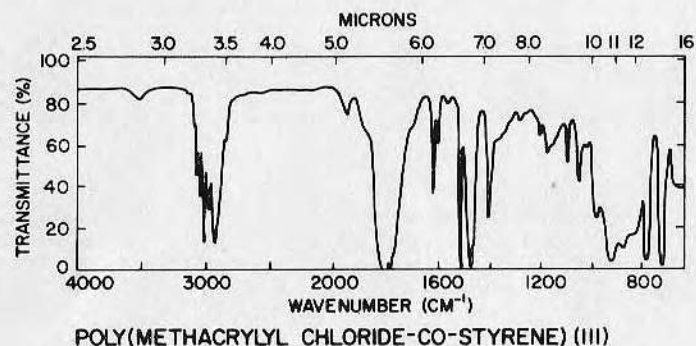
Table 4

Results of the synthesis of various polymers

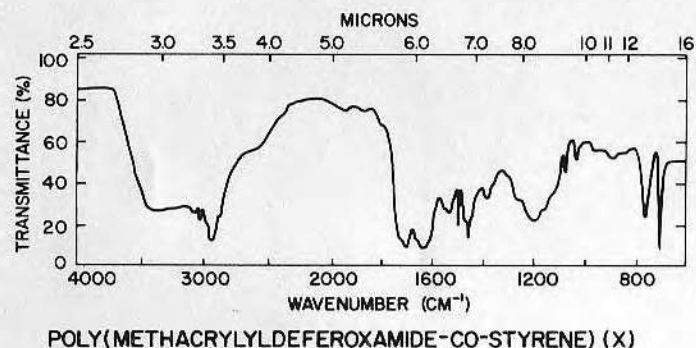
Base Polymer		Graft Polymer						
No.	Composition	Elemental Analysis				No.	Yield %	% DFA Grafted
		C	H	N	Cl			
I	$\left(\begin{array}{c} -CH_2-CH- \\ \\ CHO \end{array} \right)_n$ Polyacrolein	Calc. 64.27 Found 61.17	7.19	-	-	VIII	49	57 ratio* 1:5
II	$\left(\begin{array}{c} -CH_2-CH- \\ \\ \text{C}_6\text{H}_5 \end{array} \right)_3 \left(\begin{array}{c} -CH_2-CH- \\ \\ COCl \end{array} \right)_2$ Poly(acrylyl chloride-co-styrene)	Calc. 73.02 Found 70.88	6.13	-	14.37 14.24	IX	27	30 ratio* 1:1
III	$\left(\begin{array}{c} -CH_2-CH- \\ \\ \text{C}_6\text{H}_5 \end{array} \right) \left(\begin{array}{c} CH_3 \\ \\ -CH_2-C- \\ \\ COCl \end{array} \right)$ Poly(methacrylyl chloride-co-styrene)	Calc. 69.06 Found 70.00	6.28 6.42	-	16.99 17.52	X	51	53 ratio* 1:1

Base Polymer		Graft Polymer						
No.	Composition	Elemental Analysis				No.	Yield %	% DFA Grafted
		C	H	N	Cl			
IV	$\left(\begin{array}{c} -CH_2-CH- \\ \\ \text{C}_6\text{H}_5 \end{array} \right) \left(\begin{array}{c} CH_3 \\ \\ -CH_2-CH- \\ \\ \text{C}_6\text{H}_5 \end{array} \right)_2 \left(\begin{array}{c} CH_2-CH- \\ \\ COCl \end{array} \right)_2$ Poly(methacrylyl chloride-co-styrene co-vinyl pyrrolidone)	Calc. 62.79 Found 59.14	6.78 6.62	5.23 4.75	13.24 13.31	XI	55	60 ratio* 1:1
V	$\left(\begin{array}{c} -CH_2-CH- \\ \\ \text{C}_6\text{H}_5 \end{array} \right) \left(\begin{array}{c} -CH_2-CH- \\ \\ \text{C}_6\text{H}_4 \end{array} \right) \left(\begin{array}{c} CH_2Cl \end{array} \right)$ Chloromethylated polystyrene	Calc. 73.95 Found 77.23	6.20 6.07	-	18.85 19.86	XII	63	68 ratio* 1:2
VI	Chloromethylated Amberlite XAD-2 (Amberlite XAD-2 is polystyrene crosslinked with divinylbenzene)	Found -	-	-	6.77	XIII	97	28 ratio* 1:1
VII	Chloromethylated (Amberlite XAD-4 Amberlite XAD-4 is polystyrene crosslinked with divinylbenzene).	Found -	-	-	11.14	XIV	96	33 ratio* 1:1

* Mole ratio of reactants = polymer:DFA



(a)



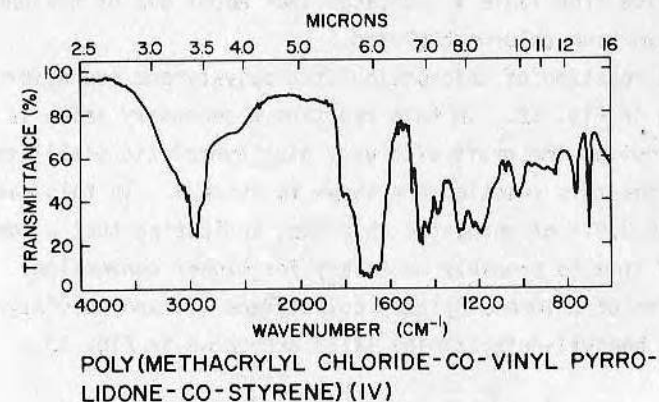
(b)

Fig.10. IR spectra of (a) poly(methacrylyl-chloride-co-styrene) (III) and (b) its deferoxamine graft (X).

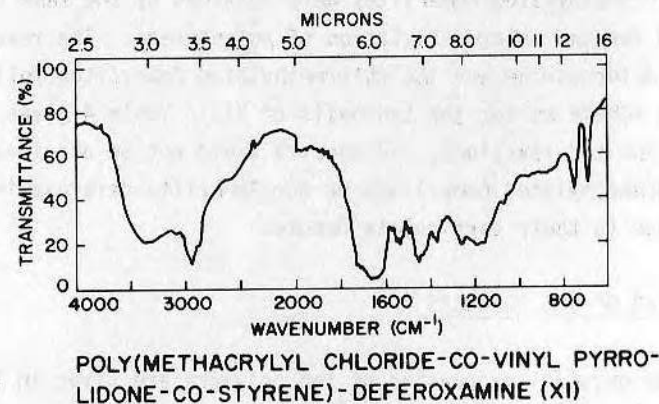
Poly(methacrylyl chloride-co-vinyl pyrrolidone-co-styrene)-Deferoxamine (XI)

The terpolymer (IV) was obtained by free radical co polymerization of methacryl chloride, N-vinyl pyrrolidone, and styrene in a 2:2:1 feed mole ratio. A ratio of 2 acid chloride units, 2 vinyl pyrrolidone units, and 1 styrene unit is obtained from elemental analysis (Table 4). The reaction of the terpolymer with deferoxamine proceeds with the formation of an amide linkage. The

chemical equation for the reaction is similar to that of Fig. 9. Results for this reaction are summarized in Table 4, and the IR spectra of both the terpolymer (IV) and terpolymer-drug graft (XI) are shown in Fig. 11.



(a)



(b)

Fig.11. IR spectra of (a) the terpolymer (IV) and (b) its deferoxamine graft (XI).

Chloromethylated Polystyrene-Deferoxamine (XII)

Chloromethylated polystyrene (V) was prepared by the reaction of commercial polystyrene¹⁸⁰ with chloromethyl methyl ether and zinc chloride. To obtain a high chlorine content, the reaction time was longer than the one normally used^{181,182}. The percentage of chlorine from Table 4 indicates that about 80% of the phenyl rings have been chloromethylated.

The reaction of chloromethylated polystyrene and deferoxamine is shown in Fig. 12. In this reaction a secondary amine is formed, which provides the graft with very high hydrolytic stability. The results for this reaction are shown in Table 4. In this case, there was 3.91% of unreacted chlorine, indicating that a longer reaction time is probably necessary for higher conversion. The IR spectra of chloromethylated polystyrene (V) and poly(styrene-co-vinyl benzyl)-deferaxamine (XII) are shown in Fig. 13.

Chloromethylated Amberlite XAD-2- and XAD-4-Deferoxamine (XIII) and (XIV)

Chloromethylated Amberlites were obtained by the same procedure used for the chloromethylation of polystyrene. The reaction between deferoxamine and the chloromethylated Amberlites follows the same scheme as for the synthesis of XII. Table 4 gives the results for the reactions. IR spectra could not be obtained for the chloromethylated Amberlites or the Amberlite-deferaxamine grafts due to their particulate nature.

PROPERTIES OF THE POLYMERS

Some physical properties of the polymers are given in Table 5. Viscosity measurements could be done only on those polymers that were soluble in appropriate concentrations.

Stability of the Grafts in Saline Solutions

Stability of the grafts in the present case refers to the degree of deferoxamine liberation when the polymers are placed in

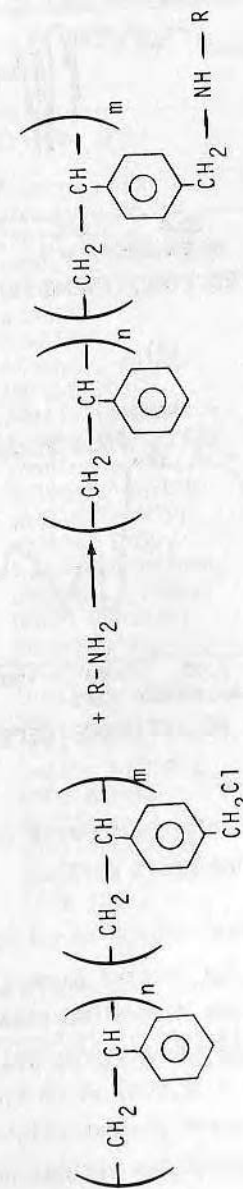
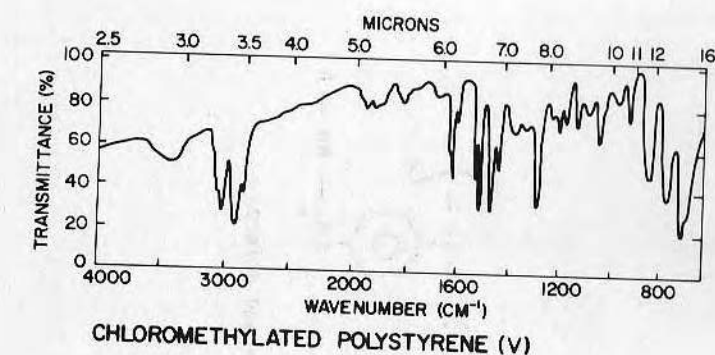
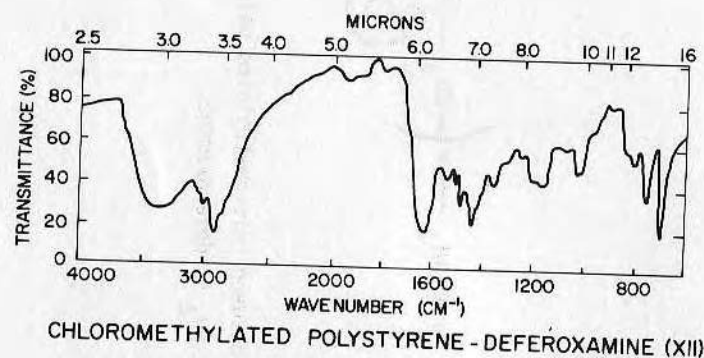


Fig. 12. Reaction between chloromethylated polystyrene and deferoxamine. R-NH₂ is deferoxamine.



(a)



(b)

Fig.13. IR spectra of (a) chloromethylated polystyrene (V) and (b) its deferoxamine graft (XII).

contact with saline solutions for several days. The presence of deferoxamine in the solutions was determined quantitatively by UV spectrophotometry. Deferoxamine has a strong absorption with a maximum of 210 nm ($\epsilon_{\text{max}} = 32,000$) at pH 5.6, allowing a rapid determination of deferoxamine concentration in solution.

Fig. 14 shows the stability of the various polymer grafts in normal saline (0.9% NaCl) solution (pH 5.6). The stability of the grafts in phosphate-buffered saline solution (pH 7.4) is shown

TABLE V
Some Physical Properties of the Various Polymers

Polymer No.	$[\eta]$ (Solvent)	Solubility	Transition Temperature(b) (°C)	Density(c) (g/cm ³)
I	0.38(a) (water)	Xylene, DMSO	M.T. 126(d)	1.196
II	1.05 (CHCl ₃)	Acetone, iso-propanol, CHCl ₃	M.T. 224	0.700
III	0.53 (DMF)	CHCl ₃ , xylene, DMF, DMSO, 1,2-dichloroethane, dioxane, CCl ₄ , acetone	M.T. 302 (some decomposition)	-
IV	0.11 (dioxane)	Swells in ethanol, xylene, DMF, DMSO	T _g 282; Dec. 358(e)	0.751
V	-	Swells in DMF(hot), xylene, DMSO, CHCl ₃	Dec. 252	0.915
VI	-	Insoluble in all solvents tested	Dec. 335	-
VII	-	Swells in DMSO	Dec. 227	0.943
VIII	-	Xylene, DMSO, 1,2-dichloroethane	Dec. 203	1.158
IX	-	Ethanol, xylene, DMSO, Dioxane, acetone, isopropanol	M.T. 352 (with dec.)	-
X	-	Xylene, DMF	Dec. 357	1.041
XI	-	Swells in DMSO, DMF, xylene, CCl ₄	T _g 261	0.964
XII	-	Swells in DMSO, DMF, xylene	Dec. 374	1.016
XIII	-	Swells in 1,2-dichloroethane	Dec. 327	0.967
XIV	-	Swells in DMSO, CCl ₄ (hot)	T _g 212; Dec. 262	0.883

a Intrinsic viscosity of a polyacrolein-bisulfite adduct solution

b Determined by differential scanning calorimetry (DSC)

c Determined by pycnometry

d M.T.: Melt temperature (center of peak in DSC thermogram)

e Dec.: Temperature at which decomposition started

in Fig. 15. In both cases, the graft with the lowest stability was VIII. This is due to the easier hydrolysis of the carbon-nitrogen double bonds. In the case of graft XII, the relatively high

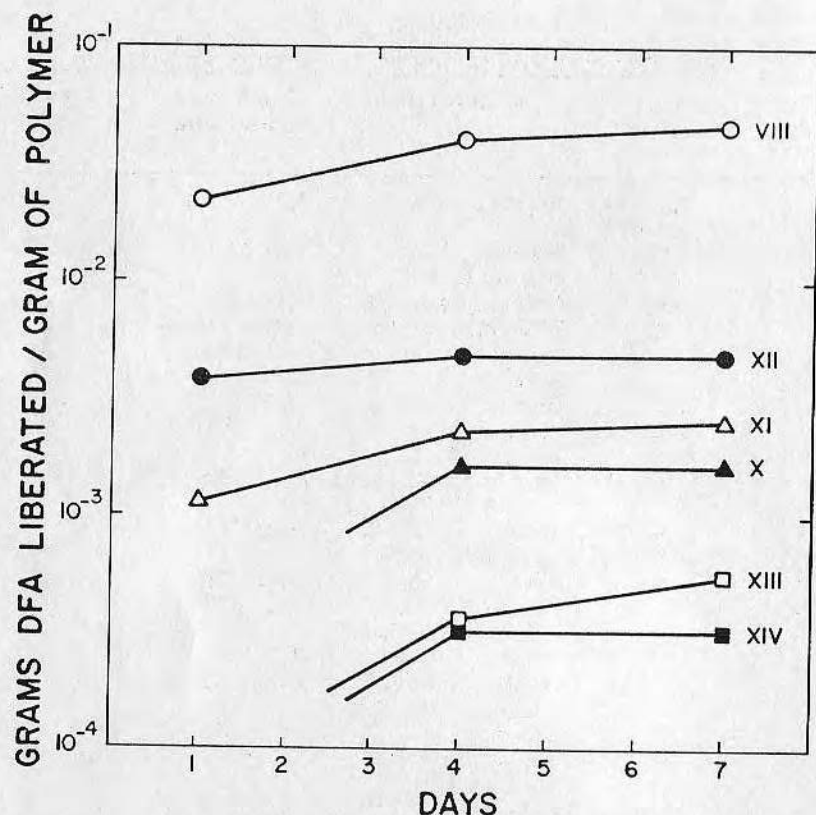


Fig. 14. Stability of the various polymer-deferoxamine grafts in normal saline solution.

concentration of liberated deferoxamine is probably due to some unreacted drug entrapped in the polymer network.

The amounts of deferoxamine liberated from the polymers were low enough to allow us to expect similar behavior in biological media. Blood plasma was used to determine the stability of the grafts in the presence of other molecules, such as proteins and enzymes, which may promote or enhance degradation of the grafts.

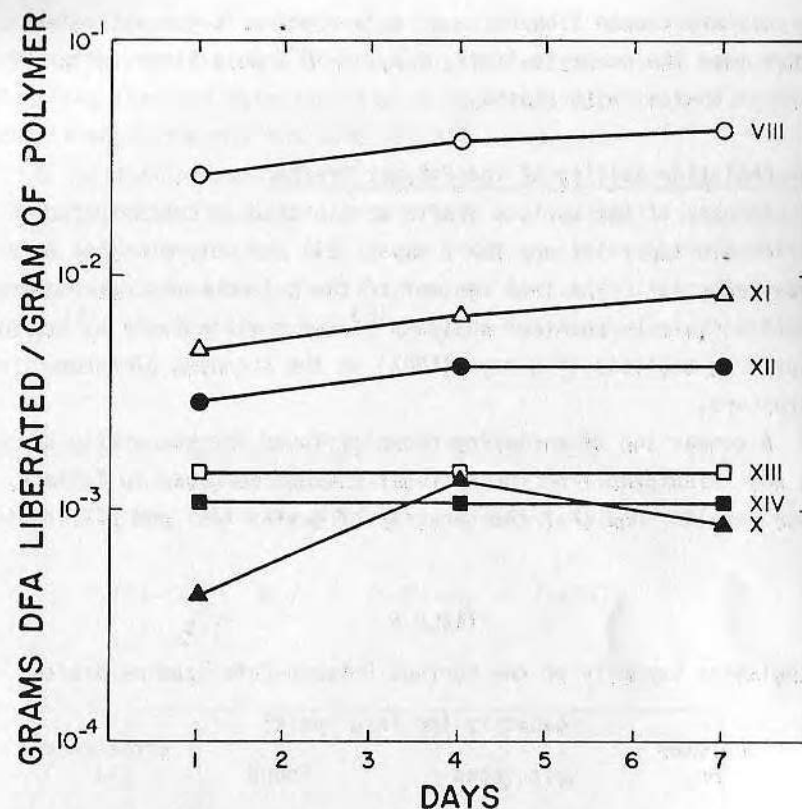


Fig. 15. Stability of the various polymer-deferoxamine grafts in phosphate buffered saline solution.

Stability of the Grafts in Plasma

The same principle, deferoxamine liberation, was used to determine the stability of the polymers in plasma. In this case the liberated drug was analyzed spectrophotometrically by forming its Fe^{3+} complex and measuring absorbances at 430 nm. This method is only accurate for concentrations not lower than $9 \cdot 10^{-5}$ mole/liter as determined from a standard calibration curve. None of

the polymers showed liberation of deferoxamine in concentrations higher than the accurate limit, i.e., $9 \cdot 10^{-5}$ mole/liter, after 27 hours in contact with plasma.

Iron Chelation Ability of the Polymer Grafts

Samples of the various grafts were placed in concentrated ferric chloride solutions for 3 days. All the polymers took on a brown-red color. The iron content of the polymers was determined quantitatively by chemical analysis¹⁸³ and qualitatively by energy dispersive analysis of x-rays (EDAX) in the scanning electron microscope.

A comparison of chelating capacity found for the grafts and the one calculated from the nitrogen content is given in Table 6. These results show that the capacity of grafts XIII and XIV (derived

TABLE 6

Chelating Capacity of the Various Polymer-Deferoxamine Grafts

Polymer No.	Capacity (mg Fe/g resin)		Efficiency ^a (%)
	Calculated	Found	
VIII	49.3	18.8	38
IX	20.8	-	-
X	40.4	17.7	44
XI	30.2	10.3	34
XII	41.6	12.9	31
XIII	14.8	6.0	41
XIV	18.6	6.2	33

a Efficiency = mg Fe found/mg Fe calculated.

from Amberlite XAD-2 and XAD-4, respectively) is about half of the capacity for other polymers. However, the efficiency is comparable, indicating that the accessibility of the iron into the chelating sites is approximately the same for all the grafts.

A qualitative analysis of the iron in the polymers is given in Fig. 16. The traces on the left side are controls, i.e., grafts without exposure to iron, and at the right are the results for iron-containing grafts. The peaks at 6.4 keV reveal the presence of iron¹⁸⁴, whereas the controls do not present any peak in that position.

Stability Constants of the Polymer Iron Chelates

When a polymer-deferoxamine iron complex (P-DFA-Fe) is placed in water, the following reaction takes place:

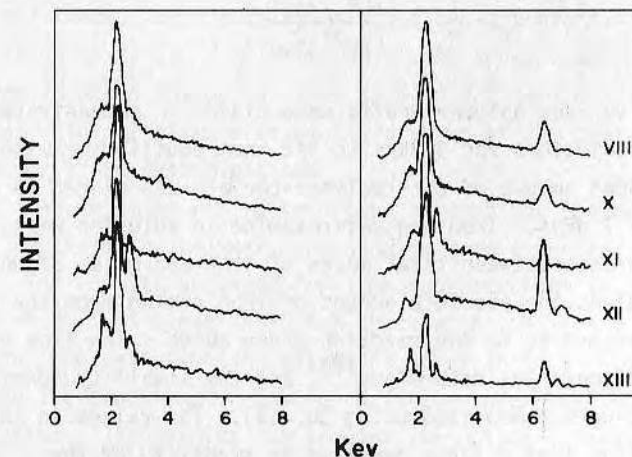


Fig.16. Energy dispersive analysis of X-rays (EDAX) of various polymer-deferoxamine-iron complexes. At the right are the traces for iron complexes, and at the left for the controls.

The equilibrium constant for this reaction is

$$K_e = \frac{[P-DFA-H_3] [Fe(OH)_3]}{[P-DFA-Fe]}, \text{ where} \quad (4)$$

$[Fe(OH)_3] = [Fe^{3+}]_{sol}$ = iron concentration in solution, and

$[P-DFA-Fe] = [Fe^{3+}]_{pol}$ = iron concentration in the polymer.

Therefore

$$K_e = \frac{[Fe^{3+}]_{sol}^2}{[Fe^{3+}]_{pol}} \quad (5)$$

and the stability constant would be

$$K_s = \frac{1}{K_e} = \frac{[Fe^{3+}]_{pol}}{[Fe^{3+}]_{sol}^2} \quad (6)$$

The various polymer grafts were placed in concentrated ferric chloride solutions for 4 days to let them equilibrate with iron. Then a known amount of each polymer-chelate was placed in distilled water for 7 days. Iron and deferoxamine in solution were analyzed. The difference between total moles of iron and moles of deferoxamine gives the absolute amount of iron coming from the polymer-chelate according to the reaction given above. The iron content of the polymers was determined¹⁸³, and the stability constants (Table 7) were calculated using Eq. (6). The values in Table 7 demonstrates that a large decrease in stability of the deferoxamine-iron complex occurs when the drug is bound to a polymer backbone. This is probably due to steric hindrance from the polymer and a decrease in mobility of the drug molecule.

TABLE 7

Stability Constants of the Polymer-Deferoxamine-Iron Complexes

Polymer	K_s (liter/mole)
X	10^6
XI	10^5
XII	10^5
XIII	10^4
XIV	10^4

REMOVAL OF IRON FROM SOLUTION IN RECIRCULATING SYSTEMS

Iron in Aqueous Solutions

Preliminary experiments for iron removal were carried out in aqueous solutions. Ferric chloride solutions of relatively high concentration ($1.2 \cdot 10^{-3}$ M) compared to the concentration of serum iron in acute poisoning cases ($4.5 \cdot 10^{-5}$ to $1.8 \cdot 10^{-4}$ M) were used. Fig. 17 gives a schematic diagram of the system employed for these determinations.

The iron solution was recirculated through the chamber containing the chelating polymer, and samples were taken in the outflow. The results obtained for iron concentration in the solution at various times indicated that, with the iron concentrations used, the resins became saturated after 15 to 20 min. of initiating the experiment, showing no further decrease in iron concentration. The results for some of the polymers tested in these conditions are given in Table 8.

The polymer grafts that were obtained in powder form (VIII-XII) became agglomerated as a hard cylinder, and the solution could not penetrate into the bulk of the resin, flowing only through

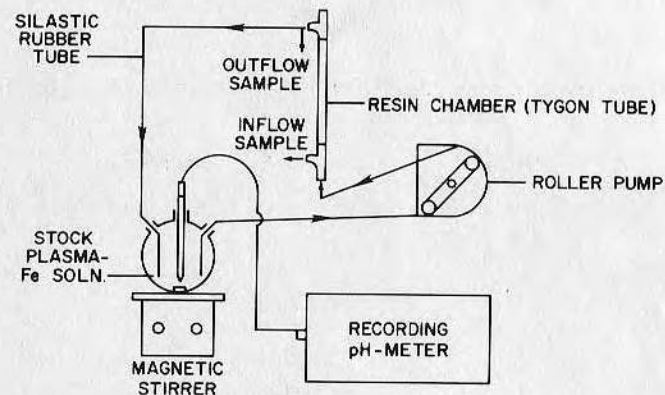


Fig.17. Diagram of the system employed in the experiments for iron removal from water and plasma.

the outer parts next to the walls of the chamber. This agglomeration effect was not present in those polymers in bead form (XIII and XIV).

Iron in Plasma Solutions

Iron was added to plasma in the form of ferric chloride in concentrations of 500 to 800 $\mu\text{g Fe}/100\text{ ml plasma}$ (i.e., $8.9 \cdot 10^{-5}$

TABLE 8

Iron Removed from Aqueous Solutions by Various Polymer-Deferoxamine Grafts

Polymer	$\mu\text{g Fe removed/g resin}$
X	792
XII	2196
XIII	661
XIV	900

to $1.4 \cdot 10^{-4}\text{ M}$). Polymer X and XII gave scattered results for the rate of iron removal. Polymers VIII, IX, and XI were not tested.

Results for grafts XIII and XIV (in bead form) are shown on Figs. 18 and 19. The plot on Fig. 18 is the rate of iron removal, i.e., decrease of iron concentration in plasma with time. The two polymers show approximately the same rate. A better comparison is given on Fig. 19 where the amount of iron removed is observed during the first hours of the experiments. Then the iron removed by graft XIV starts leveling off, while the iron removed by grafts XIII continues to increase. This result agrees with the higher chelating efficiency determined for XIII (Table 6).

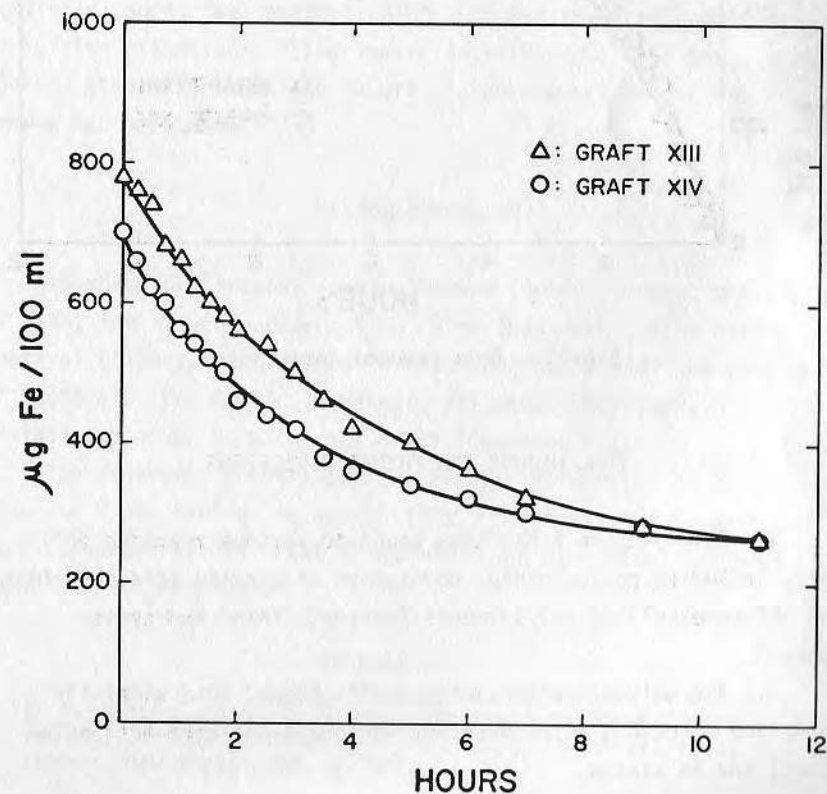


Fig.18. Rate of iron removal from plasma.

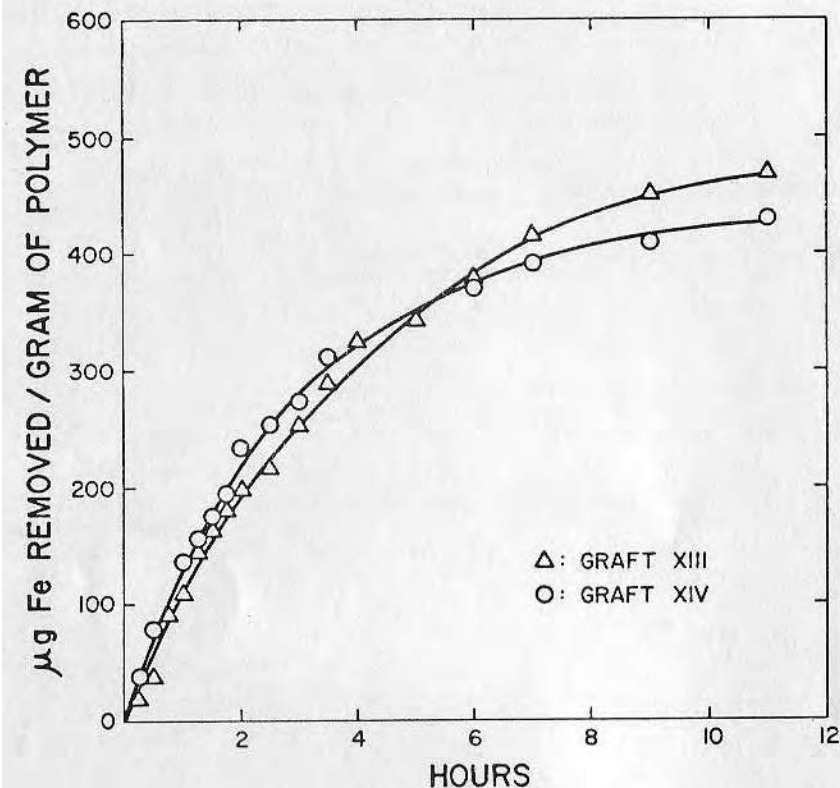


Fig.19. Iron removed from plasma.

CONCLUSIONS AND FUTURE DIRECTIONS

1. Deferoxamine B has been bound to various reactive polymers, including polyacrolein, copolymers of acrylic acid chlorides, and chloromethylated polystyrenes (uncross-linked and cross-linked).

2. The polymer-deferoxamine grafts showed good stability in saline solutions (0.9% NaCl and phosphate-buffered NaCl solutions) and in plasma.

3. The polymer-deferoxamine grafts maintained the chelation ability of the drug, although the stability of the polymer-drug-iron complex was decreased compared to the stability of deferoxamine (the soluble deferoxamine-iron complex).

4. The chelation capacity of the polymer varies from 6 to 19 mg of Fe/g of resin. This value is in the range necessary for their application in acute iron poisoning where the serum iron levels vary from 0.2 to 5 mg/100 ml of blood.

5. Additional experiments should be performed in order to study the effect of the different variables that affect the chelation process in recirculating systems.

6. The ability of the polymer-deferoxamine grafts to remove iron from plasma, a protein-rich medium where iron becomes less available, opens the possibility of applying the graft copolymer to in-vivo situations. Experiments in animals will be the next logical step after complete in-vitro characterization of the grafts has been made.

ACKNOWLEDGEMENTS

We thank Dr. Anthony Temple, Poison Control Center, University of Utah, for his encouragement in doing this work. CIBA Pharmaceutical Company, Summit, New Jersey, graciously provided samples of Desferal. Dr. Donald T. Warner, Kalamazoo, Michigan, advised and aided us with many helpful suggestions.

The financial support of the Catholic University of Chile given to R. S. Ramirez is appreciated. Portions of this work were supported by NIH Grant FD 00480-01 and Biomedical Sciences Support Grant FR-07092.

REFERENCES

1. R. M. Weaton and M. J. Hatch, "Synthesis of Ion-exchange Resins," in *Ion Exchange*, Vol. 2, (J. A. Marinsky, ed.), Dekker, New York, 1969, p. 221.

2. Dowex A-1 Chelating Resin, Dow Chemical Co., Midland, Michigan, 1964.
3. E. M. Vasil'eva, R. K. Gavurina, and O. P. Kalomeitsev, U.S.S.R. Patent 184,451 (1966); Chem. Abstr., **66**, 29770 (1966).
4. O. E. Paris (to E. I. Du Pont de Nemours & Co.) U.S. Patent 3,035,022 (1962).
5. R. Hering, J. Prakt. Chem., **32**, 291 (1966).
6. W. Sterner and L. Loveless, Sci. Techn. Aerospace Rept., **4**, 534 (1966).
7. R. Hering, J. Prakt. Chem., **34**, 69 (1966).
8. T. R. Norton, U.S. Patent 3,362,935 (1968), to Dow Chemical Co.
9. G. F. D'Alelio, U.S. Patents 3,395,134 (1968) and 3,395,197 (1968).
10. A. Zlatkis, W. Bruening, and E. Bayer, Anal. Chim. Acta, **56**, 399 (1971).
11. A. M. Talati and V. N. Mistry, Mater. Sci. Eng., **10**, 287 (1972).
12. G. Schumckler, Talanta, **12**, 281 (1965).
13. I. Shondak and A. F. Nikolaev, Vysokomol. Soedin., **7**, 1835 (1965).
14. E. B. Trostyanskaya and G. F. Nefedova, Zh. Anal. Khim., **20**, 775 (1965); Chem. Abstr., 872 (1966).
15. P. Hering, German (East) Patent 42,086 (1965).
16. G. Maura and F. Pochetti, Ann. Chim., **55**, 1000 (1965).
17. S. S. Ivanov, L. P. Gavryuchenkova, and M. M. Koton, Vysokomol. Soedin., **8**, 470 (1966).
18. Y. Matsunaga, T. Itagaki, and T. Katsuura, German Patent 2,258,535 (1973), to Mitsubishi Chemical Industries Co. Ltd., Chem. Abstr., **79**, 67075 (1973).
19. S. V. Rogozhin, V. A. Davankov, and I. A. Yamskov, Vysokomol. Soedin., Ser. B., **15**, 216 (1973).

20. K. W. Pepper and D. K. Hale, Ion Exchange and Its Applications, Society of Chemical Industry, London, 1955.
21. R. A. Mock, C. A. Marshall, and L. R. Morris, U.S. Patent 2,910,445 (1959).
22. R. Hering, Z. Chem., **5**, 29, 194 (1965).
23. G. F. D'Alelio, U.S. Patent 3,228,920 (1966).
25. A. Gabert and B. Foigt, German (East) Patent 44,124 (1965), Chem. Abstr., **64**, 19901 (1966).
26. L. O. Gunderson and H. Kerst, U. S. Patent 3,285,886 (1966), to W. R. Grace & Co.
27. R. Hering, Proc. Conf. Appl. Phys. Chem. Methods Chem. Anal., Budapest, **2**, 35 (1966).
28. G. F. D'Alelio, E. T. Hofman, and J. R. Zeman, J. Macromol. Sci. Chem., **A3**, 959 (1969).
29. G. F. D'Alelio, E. T. Hofman, and F. J. Mevers, Ibid., **A4**, 361 (1970).
30. E. Dabrunz and H. Reuter, German (East) Patent 79,152 (1971); Chem. Abstr., **76**, 60464 (1972).
31. G. F. D'Alelio, E. T. Hofman, and T. R. Dehner, J. Macromol. Sci. Chem., **A4**, 897 (1970).
32. G. F. D'Alelio, E. T. Hofman, and W. F. Strazik, Ibid., **A6**, 471 (1972).
33. G. F. D'Alelio, E. T. Hofman, and W. F. Strazik, Ibid., **A6**, 513 (1972).
34. T. Nakanishi, H. Kawamura, and H. Kakita, Japanese Patent 73 47,993 (1973), to Matsushita Electrical Industry Co. Ltd.
35. R. Hering, J. Prakt. Chem., **14**, 285 (1961).
36. E. B. Trostyanskaya, I. P. Losev, A. S. Teulina, S. B. Makarova, G. Z. Nefedova, and H. J. Lu, J. Polym. Sci., **59**, 379 (1962).
37. W. Langenbeck, H. W. Krause, and J. Reihsig, German (East) Patent 24,421 (1962); Chem. Abstr., **59**, 8901 (1963).

38. H. P. Gregor, M. Taifer, L. Citarel, and E. I. Becker, Ind. Eng. Chem., **44**, 2834 (1952).
40. J. P. Cornaz and H. Ducl, Experientia, **10**, 137 (1954).
41. G. Petrie, D. Locke, and C. Meloan, Anal. Chem., **37**, 919 (1965).
42. G. Petrie, D. Locke, and C. Meloan, Anal. Biochem., **11**, 919 (1965).
43. R. S. Ramirez and J. D. Andrade, J. Macromol. Sci. Chem., **A7**, 1035 (1973).
44. L. D. Pennington and M. B. Williams, Ind. Eng. Chem., **51**, 759 (1959).
45. R. C. DeGeiso, L. G. Donamura, and E. A. Tomic, J. Appl. Polym. Sci., **9**, 411 (1965).
46. F. Vernon and H. Eccles, Anal. Chim. Acta, **63**, 403 (1973).
47. K. F. Sugawara, H. H. Weetall, and G. D. Schucker, Anal. Chem., **46**, 489 (1974).
48. F. Wolf and M. Morgner, German Patent 1,056,825 (1959).
49. J. A. Mikes and L. Kovacs, J. Polym. Sci., **59**, 209 (1962).
50. G. Manecke and A. Gorchmann, Makromol. Chem., **82**, 146 (1965).
51. G. Manecke and H. Heller, Angew. Chem., **72**, 523 (1960).
52. E. Blasius and B. Brozio, J. Chromatog., **18**, 572 (1965).
53. V. M. Tolmachov, L. A. Lomako, and L. A. Gurskaya, Vysokomol. Soedin., **5**, 512 (1963).
54. M. J. Hatch, U. S. Patent 3,197,281 (1965), to Dow Chemical Co.
55. J. Krynicki, Polimery, **11**, 283 (1966).
56. S. B. Savvin, O. P. Eliseeva, and Y. G. Rozovskii, Dokl. Akad. Nauk SSSR, **180**(2), (1968), Chem. Abstr. **69**, 36663 (1968).
57. R. M. Genik-Sas-Berezowsky and I. H. Spinner, Can. J. Chem., **48**, 163 (1970).

58. A. B. Dovankov, Tr. Mosk. Khim. Tekhnol. Inst., **64**, 118 (1970); Chem. Abstr., **75**, 77568 (1971).
59. S. V. Vinogrova, V. A. Vasner, and V. V. Korshak, Vysokomol. Soedin. Ser. B., **13**, 805 (1971); Chem. Abstr., **76**, 86173 (1972).
60. V. D. Kopylova, K. M. Saldadze, and G. D. Azambadze, Zh. Prikl. Khim. (Leningrad), **44**, 2512 (1971); Chem. Abstr. **76**, 113823 (1972).
61. C. H. Budeanu and A. Gavriliuof, An. Stiint. Univ. "Al. I. Cuza" Iasi, Sect. 1c, **17**, 197 (1971), Chem. Abstr., **76**, 45901 (1972).
62. R. Hering, Z. Chem., **12**, 272 (1972); Chem. Abstr., **77**, 147188 (1972).
63. R. Hering and D. Haupt, German (East) Patent 88,780 (1972); Chem. Abstr., **77**, 115340 (1972).
64. Y. M. Dedk, O. P. Eliseeva, A. N. Ermakov, S. B. Savvin, and M. G. Slotintseva, Zh. Anal. Khim., **27**, 726 (1972); Chem. Abstr., 96530 (1972).
65. A. Erdelyi, S. Fustimolnar, K. Horvath, and M. Nyiro, Hungarian Patent 4,123 (1972); Chem. Abstr., **77**, 62768 (1972).
66. B. A. Zhubanov and A. K. Zharmagambetov, Izv. Akad. Nauk Kaz. SSSR, Ser. Khim., **22**, 83 (1972); Chem. Abstr., **78**, 98043 (1973).
67. G. F. D'Allelio, U.S. Patent 3,700,671 (1972).
68. G. V. Nyasoedva, L. I. Bol'shakova, and S. F. Savvin, Izv. Akad. Nauk SSSR, Ser. Khim., **1972**(9), 2033 (1972); Chem. Abstr. **78**, 59093 (1973).
69. J. Ritz, and J. Reese, German Patent 2,164,489 (1973); Chem. Abstr., **79**, 27005 (1973).
70. A. Warshawsky, German Patent 2,236,335 (1973); Chem. Abstr., **79**, 116082 (1973).
71. M. Haruta, K. Kageno, and S. Harada, Makromol. Chem., **167**, 95 (1973).
72. M. Haruta, K. Kageno, and S. Harada, Ibid., **170**, 11 (1973).

73. Y. G. Rozovskii, N. N. Basargin, N. I. Ivanova, and O. S. Ermakova, Zh. Vses. Khim. Obsch., 18, 359 (1973); Chem. Abstr., 79, 99567 (1973).
74. W. Szczepaniak and J. Siepak, Chem. Anal. (Warsaw), 18, 1019 (1973).
75. G. Manecke and E. Graudenz, Makromol. Chem., 170, 51 (1973).
76. H. Eccles and F. Vernon, Anal. Chim. Acta, 66, 231 (1973).
77. Y. Kobayashi, A. Tanaka, and M. Sugai, Bull. Fac. Eng. Yokohama Nat. Univ., 22, 45 (1973); Chem. Abstr., 80 30409 (1974).
78. B. Rodriguez Rios, A. Perlonso Uruena, and A. Maderos Perez, An. R. Soc. Esp. Fis. Quim., 61, 723 (1965).
79. P. Teyssie, C. Decoene, and M. T. Teyssie, Macromol Chem., 84, 51 (1965).
80. J. L. Sides and C. T. Kenner, Anal. Chem., 38, 707 (1966).
81. H. Small, Ind. Eng. Chem., 59, 147 (1967).
82. R. M. Diamond and D. C. Whitney, "Resin Selectivity in Dilute to Concentrated Aqueous Solutions," in Ion Exchange, (J. A. Markinsky, ed.), Dekker, New York, 1966, Vol. 1, p. 277.
83. R. C. DeGeiso, L. G. Donamura, and E. A. Tomic, Anal. Chem., 34, 845 (1962).
84. D. Reichenberg, "Ion Exchange Selectivity", in Ion Exchange, Vol 1 (J. A. Morinsky, ed.), Dekker, New York, 1966, p. 227.
85. J. Schubert, Sci. Am., 214, 40 (1966).
86. H. S. Waxman and E. B. Brown "Clinical Usefulness of Iron Chelating Agents," Prog. Hematol. 6 (1969).
87. J. Schubert, "The Chemical Basis of Chelations," in Iron Metabolism (F. Gross, ed.), Springer, Berlin, 1964, p. 466.
88. M. J. Seven, ed. Metal-Binding in Medicine, Linnincott, Philadelphia, 1960.
89. C. L. Witzleben and B. E. Buck, Clin. Toxicol., 4, 579 (1971).
90. B. E. Conley, J. Am. Med. Assoc., 170, 676 (1959).

91. R. D. Coli, L. A. Leone, and M. M. Albala, Rhode Island Med. J., 50, 549 (1967).
92. J. M. Arena, Poisoning, 2nd ed., Thomas, Springfield, Illinois, 1970, p. 369.
93. J. J. Crotty, Clin. Toxicol., 4, 615 (1971).
94. R. A. Aldrich, "Acute Iron Toxicity," in Iron in Clinical Medicine (R. E. Wallerstein and S. R. Mettler, eds.), University of California Press, Berkeley, 1958, p. 93.
95. C. F. Whitten, G. W. Gibson, M. H. Good, J. F. Goodwin, and J. Brough, Pediatrics, 36, 322 (1965).
96. W. O. Robertson, Mod. Treat., 8, 552 (1971).
97. M. A. Luongo and S. S. Bjornson, New Engl. J. Med., 251, 995 (1954).
98. W. O. Robertson, Ohio Med. J., 59, 1198 (1963).
99. I. O. B. Spencer, Br. Med. J., 1951-2, 1112.
100. J. P. Smith, J. Pathol. Bacteriol., 64, 467 (1952).
101. E. Short, B. W. Zweifach, and R. F. Furchgott, Science, 102, 489 (1945).
102. G. Forbes, Br. Med. J., 1947-1, 367.
103. J. H. Prain, Ibid, 1949-2, 1019.
104. C. F. Whitten and A. J. Brough, Clin. Toxicol., 4, 585 (1971).
105. E. Charney, J. Am. Med. Assoc., 178, 326 (1961).
106. K. R. Reissmann, T. J. Coleman, B. S. Berdai, and L. R. Morcarty, Blood, 10, 35 (1955).
107. R. Richards and S. E. H. Broosk, West Indian Med. J., 15, 134 (1966).
108. S. J. Wilson, H. E. Heath, P. L. Nelson, and G. G. Ens, Blood, 13, 483 (1958).
109. C. F. Whitten, Am. J. Dis. Child., 104, 538 (1962).
110. K. R. Reissmann and T. J. Coleman, Blood, 10, 46 (1955).

111. C. F. Whitten, Y. C. Chen, and G. W. Gibson, Pediatr. Res., 2, 479 (1968).
112. W. Westlin, Clin. Pediatr., 5, 531 (1966).
113. J. R. Walsh and J. B. Gillick, Ibid., 4, 633 (1965).
114. C. F. Whitten, Y. Cohen, and G. W. Gibson, Pediatrics, 38, 103 (1966).
115. J. T. McEnery and J. Greengard, J. Pediatr., 68, 773 (1966).
116. S. Moeschlin, Poisoning, Grune and Stratton, New York, 1965, p. 128.
117. J. T. McEnery, Clin. Toxicol., 4, 603 (1971).
118. P. D. Doolan, S. L. Schwartz, J. R. Hayes, J. C. Mullen, and N. B. Cummings, Toxicol. Appl. Pharmacol., 10, 481 (1967).
119. J. L. Fahey, C. E. Rath, J. V. Princiotto, J. B. Brick, and M. Rubin, J. Lab. Clin. Med., 57, 436 (1961).
120. J. V. H. Kemble, Guy's Hosp. Rep., 113, 68 (1964).
121. E. F. Robertson, G. H. Maxwell, and R. B. Elliott, Med. J. Aust., 2, 705 (1963).
122. G. Whelam, V. Lazio, and J. C. Biggs, Am. J. Med., 41, 626 (1966).
123. H. Bickel, E. Gaumann, W. Keller-Schierlein, V. Prelog, E. Vischer, A. Wettstein, and H. Zahner, Experientia, 16, 129 (1960).
124. W. F. Westlin, Clin. Toxicol., 4, 597 (1971).
125. S. Moeschlin and U. Schnider, New Engl. J. Med., 269, 57 (1963).
126. S. Moeschlin and U. Schnider, Iron Metab., Intern. Symp., Aix-en-Provence, France, 1963, 525.
127. S. Leikin, P. Vossough, and F. Mochir-Fatemi, J. Pediatr., 71, 425 (1967).
128. N. Movassaghi, G. G. Purugganan, and S. Leikin, Ibid., 75, 604 (1969).
129. H. Keberle, Ann. N.Y. Acad. Sci., 119, 758 (1964).

130. H. Brunner, G. Peters, and R. Jaques, Helv. Physiol. Acta, 21, C3 (1963).
131. "Desferal Mesylate," CIBA Pharmaceutical Co., Summit, New Jersey, October 1971.
132. D. G. D. Barr and D. K. B. Fraser, Br. Med. J., 1968-1, 737.
133. T. J. Covey, J. Pediatr., 64, 218 (1964).
134. J. D. Andrade, K. Kunitomo, R. Van Wagenen, B. Kastagir, D. Gough, and W. J. Kolff, Trans Am. Soc. Artif. Int. Organs, 17, 222 (1971).
135. J. D. Andrade, K. Kopp, R. Van Wagenen, C. Chen, and W. J. Kolff, Proc. Eur. Dialysis Transplant Assoc., 4, 290 (1972).
136. H. Bickel, G. E. Hall, W. Keller-Schierlein, V. Prelog, E. Vischer, and A. Wettstein, Helv. Chim. Acta, 43, 2129 (1960).
137. H. Bicker, R. Bosshard, E. Gaumann, P. Reusser, E. Vischer, W. Vosch, A. Wettstein, and H. Zahner, Ibid., 43, 218 (1960).
138. H. Bickel, H. Beberle, and E. Vischer, Ibid., 46, 1385 (1963).
139. G. Schwarzenbach and K. Schwarzenbach, Ibid., 46, 1390 (1963).
140. A. E. Martell, Stability Constants of Metal-Ion Complexes, Section II, Organic Ligands, Special Publication No. 17, Chemical Society, London, 1964.
141. J. C. Bailar Jr., Am. Sci., 59, 586 (1971).
142. D. J. Lentz, G. H. Henderson, and E. M. Eyring, Mol. Pharmacol., 9, 514 (1973).
143. J. Tripod and H. Keberle, Helv. Physiol. Pharmacol. Acta, 20, 291 (1962).
144. R. J. Cornell and L. G. Donamura, J. Med. Chem., 8, 388 (1965).
145. R. J. Cornell and L. G. Donamura, J. Polym. Sci., 3A, 827 (1965).
146. L. G. Donamura and J. Razzano, J. Med. Chem., 9, 258 (1966).
147. J. R. Dombroski, L. G. Donamura, and J. Razzano, Ibid., 10, 963.
148. J. R. Dombroski, L. G. Donamura, and J. Razzano, Ibid., 10, 964 (1967).

149. L. G. Donamura and J. Razzano, Ibid., **14**, 244 (1971).
150. J. R. Dombroschi and L. G. Donamura, J. Appl. Polym. Sci., **15**, 2119 (1971).
151. J. R. Dombroschi and L. G. Donamura, J. Med. Chem., **14**, 460 (1971).
152. J. R. Dombroschi, L. G. Donamura, and J. Razzano, Ibid., **14**, 993 (1971).
153. M. Tahan, N. Lender, and A. Zilkha, Israel J. Chem., **10**, 835 (1972).
154. B. Z. Weiner, M. Tahan, and A. Zilkha, J. Med. Chem., **15**, 410 (1972).
155. B. Z. Weiner and A. Zilkha, Israel J. Chem., **11**, 567 (1973).
156. A. Heyd, J. Pharmacol. Sci., **60**, 1343 (1971).
157. H. G. Batz, G. Franzman, and H. Ringsdorf, Angew. Chem. Int. Ed., **11**, 1103 (1972).
158. H. G. Batz, V. Hofmann, and H. Ringsdorf, Makromol. Chem., **169**, 323 (1973).
159. B. Z. Weiner and A. Zilkha, J. Med. Chem., **16**, 573 (1973).
160. H. G. Batz, G. Franzmann, and H. Ringsdorf, Makromol. Chem., **172**, 27 (1973).
161. J. Coupek, J. Torkova, O. Haobalkova, and M. Kirvakova, German Patent 2,315,508 (1973); Chem. Abstr., **80**, 30723 (1974).
162. G. Pauli, A. Gabest, G. Langhammer, and M. Gommoll, German (East) Patent 90,197 (1972); Chem. Abstr., **77**, 143810 (1972).
163. A. Goldstein, Pharmacol. Rev., **1**, 102 (1949).
164. M. C. Meyer and D. E. Guttman, J. Pharmaceut. Sci., **57**, 895 (1968).
165. Y. Cohen, Int. Encycl. Pharmacol. Ther., **78**, 241 (1970).
166. D. Borga, D. L. Azarnoff, G. P. Forshell, and F. Sjoqvist, Biochem. Pharmacol. Toxicol., **18**, 2135 (1969).
167. G. Franksson and E. Angara, Acta Pharmacol Toxicol., **28**, 209 (1970).

Surface Raman Spectroscopy

W. M. Reichert and J. D. Andrade

1. INTRODUCTION

A large number of publications discuss the use of Raman spectroscopy as applied to the study of polymers in the bulk and in solution.⁽¹⁻⁷⁾ The principles of Raman scattering are thoroughly presented in modern textbooks.⁽⁷⁻¹⁰⁾ This technique is extremely valuable in many areas of polymer characterization, including polymer synthesis, composition, conformation, chain orientation, stress, crosslinking, morphology, and impurity analysis. Only recently has Raman scattering been applied to the study of polymer surfaces and thin films.

The Raman effect (section 2) relies on the interaction of monochromatic light, generally the output of a laser, with vibrational/rotational modes of molecules to produce scattered light shifted in frequency away from the incident radiation. The magnitude of the Raman shift away from the laser line corresponds directly to the vibrational/rotational modes which produced the scattered light. An analysis of the frequency components present in the Raman scattered light can provide information about the structure, concentration, and identity of the molecules present in the scattering volume. While the Raman process is a weak effect in terms of conversion efficiency from incident to scattered light ($\approx 10^{-6}$ of the laser line intensity), molecular constituents in the low-ppm range can often be identified using existing lasers and detectors.

Systems designed for the detection of Raman-scattered laser light have four basic components: (1) a monochromatic laser source to excite scattering, (2) an optical system for focusing the laser beam onto the sample and for directing the Raman-scattered light to the spectrometer entrance slit, (3) a monochromator to disperse the scattered light into a frequency spec-

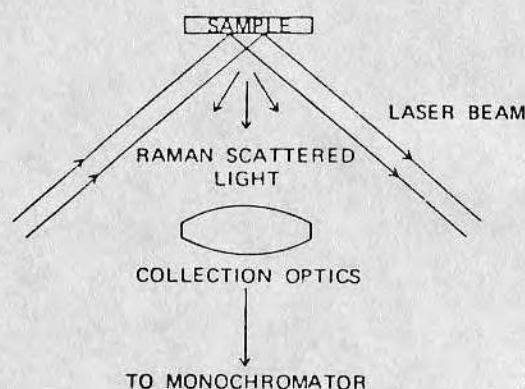


FIGURE 1. Schematic of 90° collection optics for a Raman system.

trum, and (4) a photon counter to measure the intensity of the scattered light dispersed by the monochromator. The four components are, in general, arranged into one of three collection geometries, the most common being the collection of scattered light at 90° to the sample surface (Figure 1).

The use of Raman scattered light for the characterization of surfaces and thin films is thus limited by the power of the laser light, the presence of a sufficient number of sample scattering sites within the scattering volume, and the efficiency with which the scattered light is collected.

2. RAMAN SCATTERING EFFECT

When monochromatic light of frequency ν_0 encounters a molecule the energy level of the molecule is increased by $h\nu_0$ where h is Plank's constant. This acquisition of energy causes the molecule to reach an excited virtual state. Upon relaxation the molecule can elastically return to an energy level equal to its original state, emitting light of energy $h\nu_0$, or the molecule can inelastically return to an energy level higher or lower than its original state emitting light of energy $h(\nu_0 - \nu_1)$ or $h(\nu_0 + \nu_1)$, respectively (Figure 2).

The vast majority of such molecular transitions emit light at the same frequency as the incident light (ν_0). This elastic emission of light is called Rayleigh scattering. The small number of inelastic transitions which cause light to be scattered at frequencies away from the Rayleigh line produce Raman-scattered light. The light scattered below ν_0 gives rise to Stokes lines ($\nu_0 - \nu_1$) and that scattered above ν_0 the anti-Stokes lines ($\nu_0 + \nu_1$) (Figures 2 and 3).

Molecular transitions resulting in scattered light occur when the oscillating electric field vector of the incident light exerts oppositely directed forces on the electrons and nuclei of the illuminated molecule, thus inducing

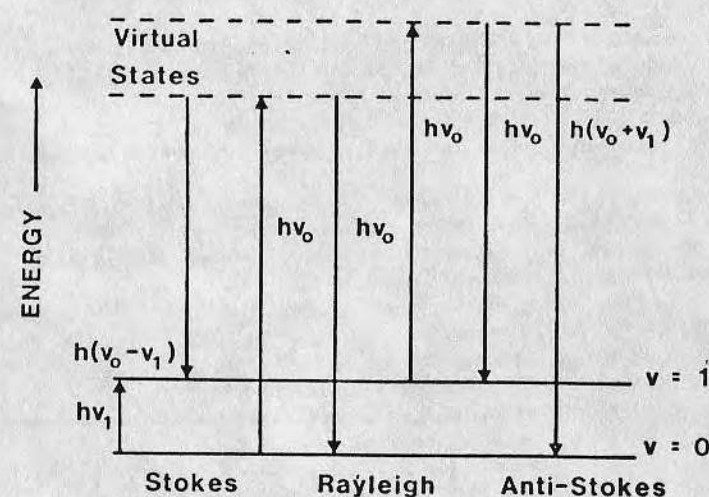


FIGURE 2. Energy level diagram showing elastic ($h\nu_0$) and inelastic [$h(\nu_0 - \nu_1)$ and $h(\nu_0 + \nu_1)$] molecular transitions.

an alternating dipole moment. The alternating dipole in turn emits the radiation detected as scattered light. If the polarizability of the molecule remains constant during illumination then the emitted radiation will have the same frequency as the incident light (Rayleigh scattering). However, if the molecule has a periodic change in polarizability (via vibrational or rotational modes) a small portion of the emitted dipole radiation will be

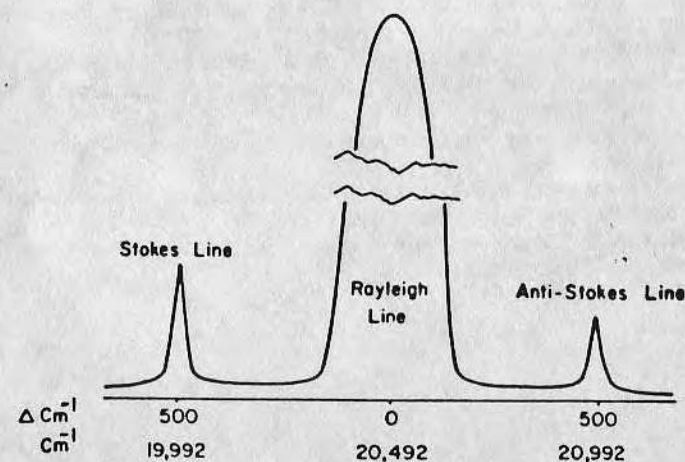


FIGURE 3. A hypothetical Raman spectrum displaying the Rayleigh line (ν_0), Stokes line ($\nu_0 - \nu_1$), and anti-Stokes line ($\nu_0 + \nu_1$). Note the relative intensities and symmetrical distribution. [Reprinted from Reference (9), p. 9, by permission.]

shifted away from the Rayleigh line. The frequency shift results from a loss $[h(\nu_0 - \nu_1)]$ or gain $[h(\nu_0 + \nu_1)]$ of energy equal to an energy level increase or decrease of the mode which altered the molecular polarizability. This altered dipole radiation is emitted as Raman-scattered light. Because an energy level increase and decrease are both probable the Raman-scattered light is shifted symmetrically with respect to the Rayleigh line (Figure 3). The magnitude of the frequency shift away from ν_0 is characteristic of specific modes. This fact makes Raman scattering a powerful characterization technique. An excellent overview of the Raman effect is given in Reference (9).

The ability of a molecule or molecular substituent to emit Raman scattered light can (in theory) be considered in terms of a polarizability interaction parameter called the Raman cross section.⁽⁸⁾ This term measures the rate at which a given scattering site removes energy from the incident beam, relative to the intensity of the incident beam. Using this concept the Raman signal intensity, I_s , in counts per second is given by

$$I_s = \frac{N\Phi\Omega I_L \epsilon}{E_p} \frac{d\sigma}{d\Omega} \quad (1)$$

where N = concentration of scatterers in number of scatterers per cm^3 , Φ = total scattering volume imaged onto the spectrometer entrance slit in cm^3 , Ω = solid angle of the collection optics in steradians, I_L = average intensity of the laser within the volume Φ in watts/cm^2 , ϵ = overall efficiency of the Raman spectrometer including lens reflection losses, spectrometer throughput, and the quantum efficiency of the photodetector, E_p = energy of a laser photon in joules, and $d\sigma/d\Omega$ = differential Raman cross section of a single scatterer per unit solid angle of collection in units of $\text{cm}^2/\text{steradians}$. The Raman cross section of many gases are readily available;⁽¹¹⁾ however, the values pertaining to solids and liquids have to be estimated from similar bands found in the gas literature.

3. SURFACE AND THIN FILM RAMAN SPECTROSCOPY

3.1. EXTERNAL REFLECTION

The majority of surface Raman studies have used an externally reflected laser beam (Figure 1) to excite Raman scattering from sample molecules adsorbed onto various substrates. The choice of substrate and sample is dependent upon: (1) the ability of the substrate to absorb a large number of sample molecules within the scattering volume of the reflected beam, and (2) on the ability of the sample to scatter light which is easily distinguished from the light scattered by the substrate. Generally the substrates

were high-surface area oxides or silicates whose Raman spectra were sufficiently weak or simple to allow detection of the Raman lines arising from the sample. In most cases the spectrum of the adsorbed sample was compared to the bulk sample spectrum to detect shifts in the Raman bands that could give information about the adsorption process. These studies, their results, and problems have been reviewed in detail by several authors.⁽¹²⁻¹⁶⁾

The application of external reflection Raman to the study of surface-adsorbed polymers has been limited. Koenig and Shih⁽¹⁷⁻¹⁹⁾ used this technique to study glass and silica fibers treated with vinylsilane and methyl methacrylate. In these studies it was found that treatment of the fibers with silane produced a chemically bound surface coat of poly(vinylsilane) (PVS), and that polymerization of methyl methacrylate (MMA) in the presence of the PVS-coated fibers resulted in a chemically bound PMMA/PVS copolymer on the fiber surface. Rives-Arnaud and Sheppard⁽²⁰⁾ and Tsai *et al.*⁽²¹⁾ used external reflection Raman to study the polymerization of acetylene on rutile (TiO_2) surfaces and its decomposition in the presence of oxygen.

Although the external reflection technique has been relatively fruitful, the adsorbed species produce inherently weak bands, usually $10^{-7} I_0$, where I_0 is the intensity of the reflecting laser beam.

In addition to increasing the number of sample scatterers present within the scattering volume, some methods exist for improving the collection of the light scattered by the sample. One approach is to use high laser power, high signal amplification, long photon counting times, or slow scanning speeds. The use of repeated scans for signal averaging purposes often produces high levels of background scattering which can swamp out the weak bands of the adsorbed molecules. Another option is the use of tunable dye lasers to obtain a resonance Raman effect which can enhance Raman bands of certain samples by a factor of up to 10^5 .⁽¹⁰⁾ Other investigators have attempted to improve the inefficient use of the incident beam intensity in generating scattered radiation.

Connel *et al.*⁽²²⁾ developed a system where the thickness of the sample and an underlying dielectric layer are adjusted such that the beam reflected from the sample is exactly cancelled by the light reflected at least once from a metallic reflector base upon which the sample and dielectric film rest (Figure 4). Furthermore, the conditions which allow the sample to have a zero reflectance are exactly those required to create an in-phase addition of the scattered radiation emitted from the sample, thus producing a stronger Raman signal.

Greenler and coworkers^(23,24) used a multi-reflection technique to improve the exposure of the incident laser light by coating samples onto the surface of two parallel silver mirrors (Figure 5). Here a large standing wave is established at the mirror surface whose intensity is proportional to

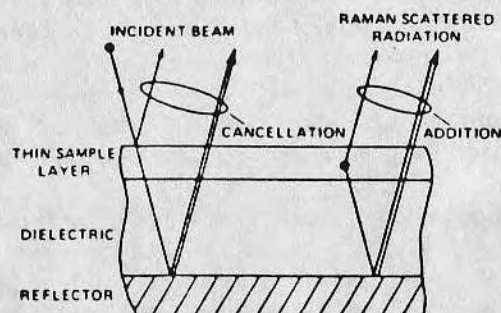


FIGURE 4. Schematic of in-phase addition geometry to enhance the Raman signal from thin film samples. [Reprinted from Reference (22), p. 31, by permission.]

the Raman scattering of the sample. This intensity is maximized through proper selection of the laser beam incident angle and the mirror separation. Additionally, the intensity of the collected scattered light could be maximized at a certain collection angle. This study⁽²⁴⁾ is of particular interest because the 1002 cm^{-1} Raman line of polystyrene was observed in films as thin as 50 and 200 Å (Figure 6). However, Greenler and coworkers did note that this technique is perhaps an order of magnitude less sensitive than that required for polymer surface and monolayer investigations.

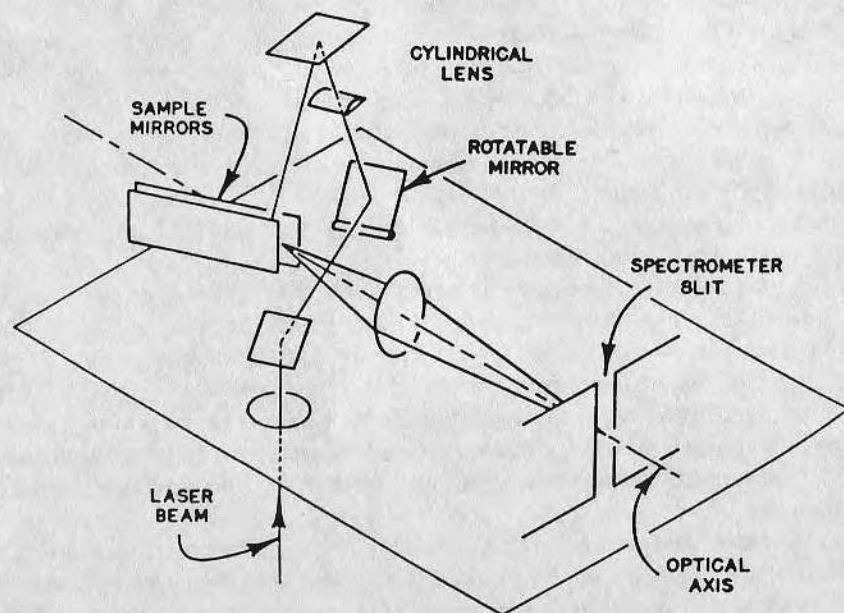


FIGURE 5. Schematic of the system used to record the Raman spectrum of polystyrene on silver mirrors. [Reprinted from Reference (24), p. 384, by permission.]

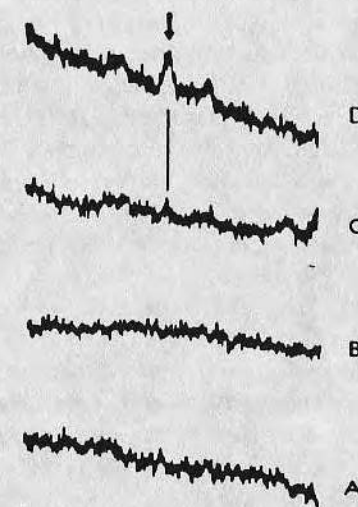


FIGURE 6. Raman spectra of polystyrene on silver mirrors. Band marked by the arrow is at 1005 cm^{-1} . (A) Spectrum of clean silver mirrors; (B) spectrum of silver mirrors rinsed with benzene; (C) spectrum of 50-Å layer of polystyrene on silver mirrors; (D) spectrum of 200-Å layer of polystyrene on silver mirrors. [Reprinted from Reference (24), p. 384, by permission.]

3.2. TOTAL INTERNAL REFLECTION (TIR)

Within the last five years or so several groups have been exploiting total internal reflection (TIR) optics to investigate the Raman scattering from a small region extending from the sample surface to a depth of about one wavelength of the incident laser beam. The basic sample configuration of a TIR Raman experiment consists of a three-phase system, $n_1 > n_2 \geq n_3$ (Figure 7), where n_i is the index of refraction of the three phases. In general, n_1 is the semi-infinite incident medium, usually an internal reflection element, n_2 is the thin film sample of thickness d_2 , and n_3 is the semi-infinite final phase.

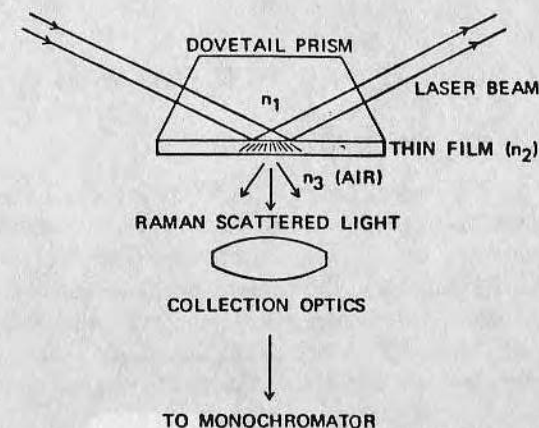


FIGURE 7. Schematic of basic three-phase sample configuration of a TIR Raman experiment.

TABLE 1
 TIR Raman of Thin Films

Incident phase (n_1)	Sample film (n_2) ^a	Final phase (n_3)	Reference
Flint glass	CS ₂	Air	26
Water	CO dye	Air	29
CCl ₄	BRBS dye	Water	30, 31
Flint glass*	Hemin, bilirubin, cobalamin	Air	32
Quartz	C ₂ H ₅ OH	Air	32
Fused silica	PVA	Water	33
Sapphire	Bovine albumin	Air	34
Sapphire	PS	Air	34
Sapphire	PS	PE	35, 36
Sapphire	PS	PC	36

^a BRBS = Brilliant Red BS, CO = Cetyl Orange, PVA = poly(vinyl alcohol), PS = polystyrene, PE = polyethylene, PC = polycarbonate.

TIR Raman was apparently first proposed by Hirschfeld in 1970.⁽²⁵⁾ Another early study was that of Ikeshoji *et al.*⁽²⁶⁾ Detailed theoretical treatments of TIR Raman are available in the literature.^(27,28) Table 1 lists the recently reported applications of TIR Raman to the study of thin films.

Briefly, the Raman scattering of thin film samples is excited by a partial penetration of the totally reflecting laser beam below the n_1/n_2 interface. This penetration produces an exponentially decaying, or evanescent, intensity field in n_2 and n_3 . From theory, the fraction of the evanescent intensity residing within the film (I_2) and the final medium (I_3) is proportional to

$$I_2 \propto 1 - \frac{|T|^2}{|t|^2} e^{-2d_2/d_p} \quad (2)$$

and

$$I_3 \propto e^{-2d_2/d_p} \quad (3)$$

respectively. The terms $|t|$ and $|T|$ are the transmitted interfacial electric field amplitudes during TIR at the n_1/n_3 interface in the absence of a film ($d_2 = 0$) and at the n_2/n_3 interface in the presence of a film of thickness d_2 , respectively. The value d_p is the depth of penetration of the final medium which defines the rate of the electric field decay from the n_2/n_3 interface into n_3 . The light scattered by the sample is proportional to this field intensity. The electromagnetic considerations of TIR have been discussed in detail by Knutson and Reichert.⁽³⁷⁾

Beyond such factors as collection optics and laser power, there are three basic considerations when designing a TIR Raman experiment: (1) the Raman spectra and background scattering of the incident and final phases, (2) the sample thickness, and (3) the angle of incidence of the laser beam at the n_1/n_2 interface (θ_1) which must be greater than the critical angle (θ_c) for total reflection [$\theta_1 > \theta_c = \sin^{-1}(n_2/n_1) \geq \sin^{-1}(n_3/n_1)$ where $n_1 > n_2 \geq n_3$].

The Raman bands from the incident and final phases mix with those arising from the sample film, thus presenting a problem when trying to isolate the sample spectrum. The optimum situation is one where n_1 and n_3 are colorless, transparent, possess no Raman bands within the region of the sample spectrum, and have no background scattering. For organic samples the incident phase is a high index material like flint glass or sapphire. Sapphire is particularly suitable because of its high purity (low background scattering) and lack of Raman bands above 800 cm⁻¹ which is the fingerprint region of most organic materials.⁽³⁶⁾ The final medium is generally air or water, both of which are poor scatterers of light and have relatively low refractive indices.

The application of TIR Raman to the study of thin polymer films has essentially been limited to the work of Iwamoto *et al.*⁽³³⁻³⁶⁾ This group has published the TIR Raman spectra of several polymers, most notably an investigation of polystyrene thin films (Figure 8).

The effect of sample thickness (d_2) and incident angle of the laser beam at the n_1/n_2 interface (θ_1) arises from their influence on the intensity distribution of the evanescent field and hence the intensity available to

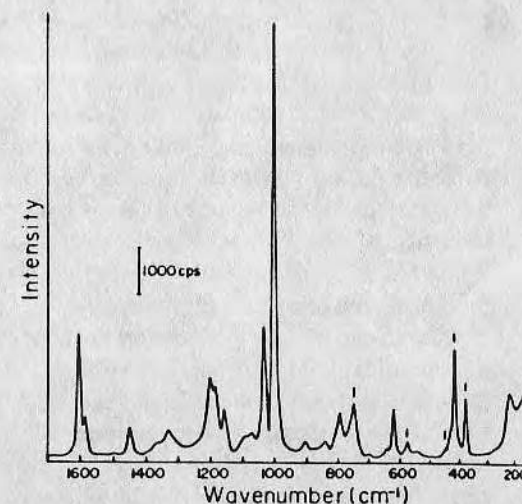


FIGURE 8. TIR Raman spectrum of a 0.7- μ m thick polystyrene film at the critical angle. Marked peaks are due to the sapphire internal reflection element. [Reprinted from Reference (34), p. 586, by permission.]

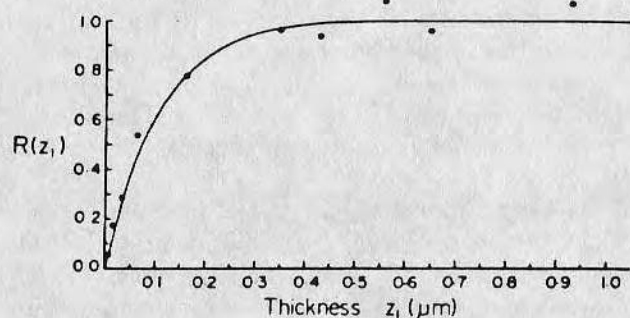


FIGURE 9. Relative TIR Raman intensity $R(z_1)$ of a polystyrene film as a function of film thickness z_1 . Incident laser light is 488 nm. Solid curve: theoretical; circles: experimental. [Reprinted from Reference (36), p. 4786, by permission.]

excite Raman scattering within the film. The variables in Eqs. (2) and (3) are all functions of sample thickness and/or incident angle.

Figure 9 is a plot from the work of Iwamoto *et al.*⁽³⁶⁾ showing theoretical and experimental TIR Raman intensities. The 1002 cm^{-1} polystyrene peak is plotted as a function of sample film thickness for a system where n_1 is sapphire, n_2 is the polystyrene film, and n_3 is a polycarbonate substrate. The experimental Raman intensities, $R(z_1)$, were scaled relative to the intensity of a polystyrene sample much thicker than the distance penetrated by the evanescent field intensity. The experimental intensities were calculated from Eq. (2). Here a system was chosen where $n_2 = n_3$. This simplifies Eq. (2) to $1 - e^{-2d_z/d_p}$, where d_p is now the depth of penetration for both the polystyrene film and the polycarbonate final phase.

For films much thinner than the laser wavelength ($z_1 = d_2 \ll \lambda$) the Raman intensity increases linearly with film thickness (Figure 9). In this linear region the sample comprises less than half of the total evanescent field intensity in n_2 and n_3 , thus making room for a considerable contribution from the final medium to the observed Raman spectrum. However, for film thickness on the order of a wavelength or greater ($z_1 = d_2 \geq \lambda$) the Raman intensity of the film levels off, thus indicating that the polystyrene film thickness is reaching and eventually extending past the volume occupied by the evanescent field intensity.

Iwamoto *et al.*⁽³⁶⁾ also demonstrated the effect of incident angle, θ_1 , on the measured Raman intensity of the polystyrene film (n_2) and the polycarbonate final phase (n_3). Figure 10 is an experimental and theoretical plot of the 890 cm^{-1} polycarbonate: 1002 cm^{-1} polystyrene band intensity ratio ($I_{PC}^{890}/I_{PS}^{1002}$) as a function of θ_1 , where θ_1 is greater than the critical angle for total reflection (θ_c). The theoretical intensity ratio was calculated from the ratio of Eq. (2) to Eq. (3) where $n_2 = n_3$. Theory states the

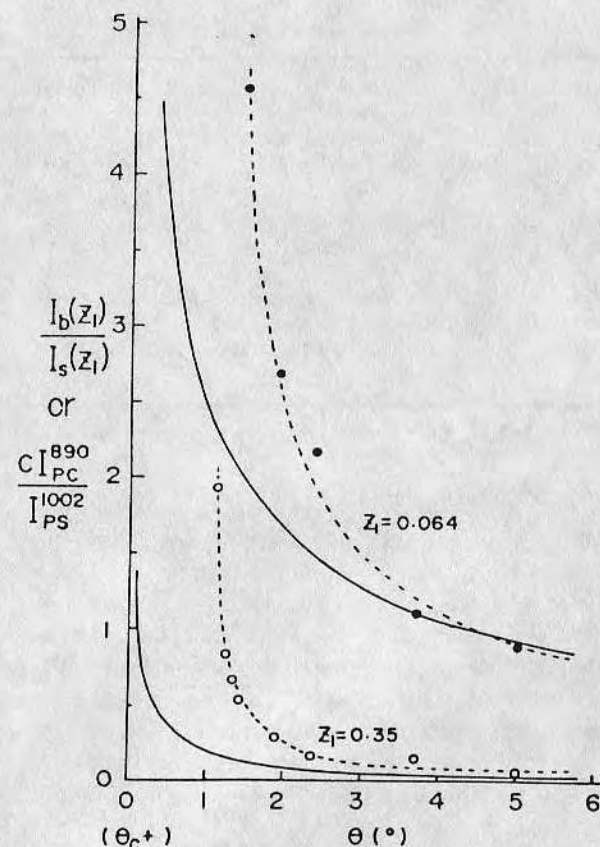


FIGURE 10. Dependence of relative TIR Raman intensities of the polycarbonate final phase (I_{PC}^{890}) to the polystyrene thin film (I_{PS}^{1002}) on the angle θ away from the critical angle θ_c ($\theta = \theta_1 - \theta_c$). Solid curve: theoretical; filled and open circles: experimental. Also note the effect of polystyrene film thickness. [Reprinted from Reference (36), p. 4789, by permission.]

evanescent field reaches its maximum scattering volume for $\theta_1 = \theta_c$ and decreases steadily as θ_1 increases away from θ_c .⁽³⁷⁾ This pattern is consistent with the data in Figure 10. With an increasing incident angle away from θ_c the scattering volume recedes away from the polycarbonate final phase into the polystyrene causing I_{PC}^{890} to decrease and the ratio of $I_{PC}^{890}/I_{PS}^{1002}$ to do likewise. Also note that in the thicker polystyrene film the intensity ratio goes to zero which indicates that at higher θ_1 values the evanescent field decays completely within the polystyrene film. The discrepancy between theory and experiment may be attributed to divergence of the laser beam and the fact that the Raman bands of polystyrene and polycarbonate have different Raman cross sections.⁽³⁶⁾

The use of single reflection TIR Raman for the study of polymer surfaces is limited by the need for ultra-thin films ($\sim 50 \text{ \AA}$) to increase the surface to volume ratio of the sample and hence the surface Raman signal. Unfortunately, this requirement produces a situation where the sample comprises a very small portion of the total evanescent scattering volume, thereby producing very weak Raman signals. Consequently, this technique is restricted to those transparent polymers with very strong scattering peaks. Polystyrene is a possible candidate for surface studies due to the identification of distinct Raman peaks in films as thin as 600 \AA .⁽³⁶⁾ Another potential solution to this dilemma is a multiple reflection configuration to increase the number of reflection sites that contribute to the sample spectrum.

3.3. WAVEGUIDE METHODS

Swalen *et al.*⁽³⁸⁻⁴¹⁾ have described waveguide integrated optics and its application to determining polymer film thickness and refractive index. As shown by Rabolt *et al.*⁽⁴⁴⁻⁴⁹⁾ and Levy *et al.*⁽⁵⁰⁾ the waveguide geometry provides an excellent technique to excite Raman scattering in micron and submicron polymer films (Figure 11a). The excitation source is the guided

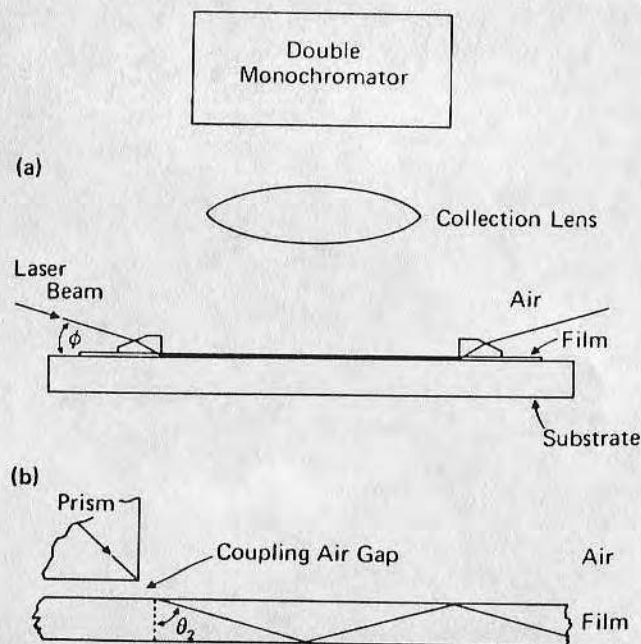


FIGURE 11. (a) Instrumental arrangement for recording the waveguide Raman spectrum of thin polymer films. (b) Laser beam coupled into a thin polymer film and undergoing multiple internal reflections. [Reprinted from Reference (44), p. 550, by permission.]

wave which propagates down the length of the polymer film by total internal reflection back and forth between the two film interfaces (Figure 11b). Here the refractive index of the film (n_2) must be greater than the refractive indices of the two adjacent media [n_1 (air) $< n_2$ (polymer waveguide) $> n_3$ (substrate)].

In addition to satisfying the critical conditions for total reflection at the n_1/n_2 and n_2/n_3 interfaces [$\sin^{-1}(n_1/n_2) < \theta_2 < \sin^{-1}(n_3/n_2)$] the angle of reflection within the film (θ_2) must equal one of the discrete angles associated with guided modes. The specific angles are required because the light wave in the film is not a single ray as shown in Figure 11b but a summation of light rays. The repeated reflection back and forth of these rays produces various interference patterns within the film depending upon the phase relationship between the reflecting rays. For a given set of n_1 , n_2 , n_3 , film thickness d_2 , and laser wavelength λ values there exists a finite set of θ_2 values which permit constructive interference patterns to develop, allowing the wave to propagate down the film. The propagating wave is called a guided mode.

More specifically, three events within the film alter the phase of the reflecting light rays: total reflection at the n_1/n_2 and n_2/n_3 interfaces, and traversing the film. If these phase changes sum to a multiple (m) of 2π then constructive interference results and a guided mode is launched. For a given mode number m , there are $(m + 1)$ field intensity modes across the film. Figure 12 shows the field intensity distribution across a poly(vinyl alcohol) wave guide (n_2) for the four guided modes which the waveguide will support. Also note the evanescent fields created in air (n_1) and the quartz substrate (n_3). Eigenvalue equations have been developed for calculating the mode-generating angles (θ_2) as a function of n_1 , n_2 , n_3 , d_2 , and λ . The theory of total internal reflection is discussed elsewhere.⁽³⁷⁾ The theory of optical waveguides has been presented by Marcuse⁽⁴²⁾ and Kapany and Burke.⁽⁴³⁾

The waveguide system shown schematically in Figure 11 couples the laser light into the polymer film by an evanescent field created in an approximately 500- \AA air gap between the polymer film and the high-index prism. The coupling angle ϕ is adjusted to obtain (via Snell's Law) the proper angle θ_2 that will allow the coupled beam to propagate down the film. The Raman scattered light is collected at an angle 90° to the direction of the guided mode. Through the principle of reciprocity, the beam can be coupled back out at the other end of the waveguide through another coupling prism.

In addition to collecting the Raman-scattered light directly from the polymer waveguide,^(44,46,50) this geometry has been used to obtain the Raman spectra of ultra-thin polymer films spun cast on top of the waveguide⁽⁴⁵⁻⁵⁸⁾ and the evanescently excited resonance Raman spectra of Langmuir-

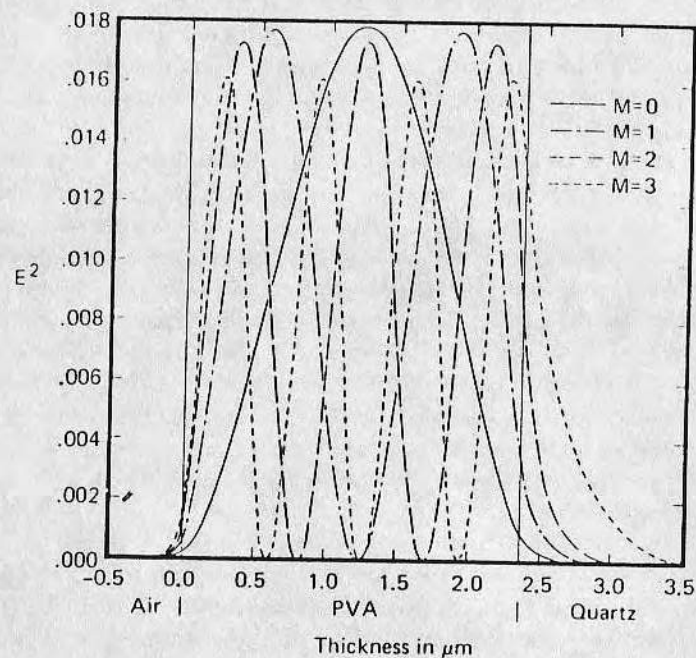


FIGURE 12. Mode intensity patterns for a 2.3- μm thick PVA waveguide. [Reprinted from Reference (41), p. 169, by permission.]

Blodgett dye monolayers deposited on the polymer waveguide surface.⁽⁴⁷⁻⁴⁹⁾ These studies are summarized in Table 2.

The advantages of the waveguide Raman technique lie in the efficient manner in which guided modes excite Raman scattering within polymer films. Different mode intensity patterns emphasize different portions of the polymer waveguide (Figure 12). This feature is particularly effective in the study of polymer laminate structures.⁽⁴⁵⁻⁴⁸⁾

Typically, one observes a factor of 10 to 100 more reflections/cm with a guided mode than from an attenuated total reflection experiment. These multiply reflected beams produce a large scattering volume inside the thin films which appears macroscopically as a streak. The streak then can be focused directly onto the monochromator slit. Figure 13 compares two Raman spectra taken by these authors of the same 1- μm polystyrene film using the conventional back-scattering (external reflection) and the waveguide-enhanced techniques. Note the excellent signal enhancement (~ 55) and signal-to-noise ratio of the waveguide-enhanced spectrum. Finally, the evanescent streak at the waveguide surface can be used to excite the Raman spectra of very thin films deposited on a polymer surface (Figure 14).

TABLE 2
Waveguide Raman Spectroscopy of Polymers and Langmuir-Blodgett Dye Monolayers

Substrate	Waveguide ^a	Spun cast polymer film ^a	Dye monolayer ^b	Reference
Pyrex	PS (1-2 μm)			44
Pyrex	PMMA (1-6 μm)			50
PMMA	PVA (1-2 μm)			46, 47
Pyrex	PVA (1-2 μm)	PS (0.25-0.5 μm)		45, 46, 47
Pyrex	PVA (1-2 μm)	PMMA (0.25-0.5 μm)		46, 47
Pyrex	Corning glass (1 μm)	PS (0.05-0.5 μm)		48
Pyrex	Corning glass (1 μm)		CP dye, SQ dye	47, 48, 49
Pyrex	PVA (1-2 μm)		CP dye	47, 49

^a PS = polystyrene, PVA = poly(vinyl alcohol), PMMA = poly(methyl methacrylate).
^b CP = 1, 1'-dioctadecyl-2,2'-cyanine perchlorate, SQ = Squarylium.

3.4. PLASMON ENHANCEMENT

Because the Raman signal intensity is directly proportional to the average laser intensity [Eq. (1)] any technique or trick which concentrates or otherwise enhances the laser intensity in the scattering volume will increase or enhance the signal. A number of metal thin films, in particular, silver, can be used for this purpose. Since the volume we are interested in

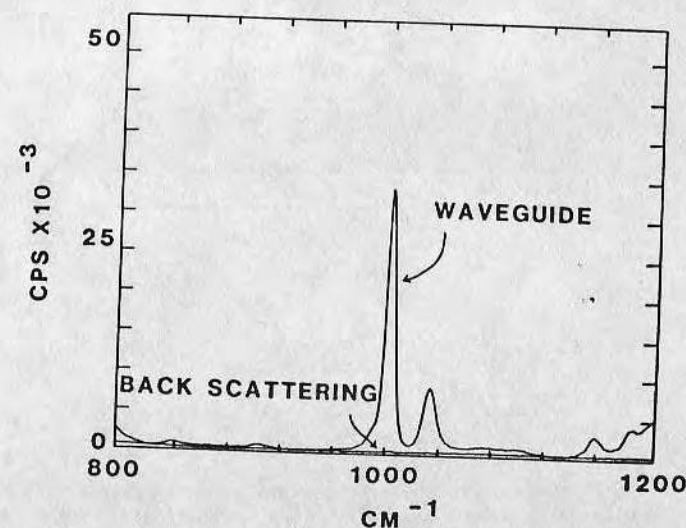


FIGURE 13. Comparison of waveguide and back-scattering Raman spectra of a 1- μm polystyrene film.

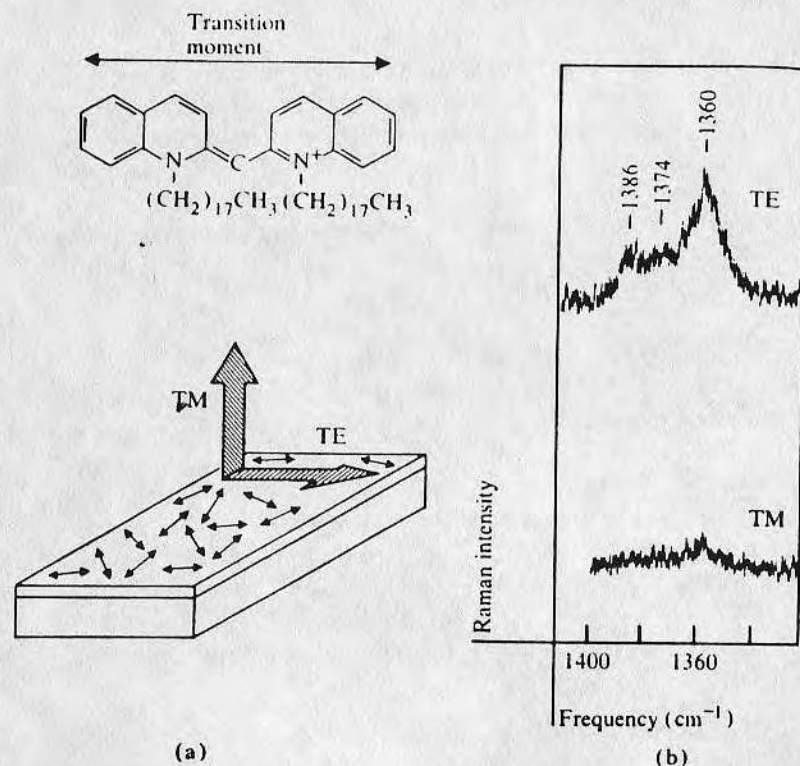


FIGURE 14. (a) Schematic of chromophore orientation on the waveguide surface and input laser polarization for TE and TM modes of propagation. (b) Resonant Raman spectra of the adsorbed chromophore in the 1320-1420 cm^{-1} range. [Reprinted from Reference (41), p. 7, by permission.]

is the interfacial volume, the trick is to couple or direct the laser beam energy only into the surface or interface of interest.

The optical and dielectric properties of matter are, to a large extent, determined by the interactions of the constituent atomic and molecular orbital electrons with the light. In the case of metals, the optical properties are dominated by the fact that one has a free electron gas in the bulk of the material. It can be shown that this free electron gas has its own resonance frequencies called plasma frequencies or plasmons. The plasma oscillation is a collective longitudinal excitation in the free electron gas. The energy associated with these plasma oscillations is directly measurable through electron energy loss measurements and is observed in XPS spectra (Chapter 5). These energies are in the range of roughly 4-15 eV for metals and 12-17 eV for various semiconductors.⁽⁵¹⁾ Because of the different bonding environments in the vicinity of any surface, the electrons near the surface of the

metal have different resonances or plasmon excitation energies from those in the bulk. Thus, surface plasmons are observed and can be readily measured by variable angle XPS (Chapter 5). Surface plasmons are generally several eV lower in energy than the bulk volume plasmons.

If one can direct a beam of light onto a metal surface or interface, such that the bulk or surface plasmons are excited, then this becomes a means of Raman signal enhancement. This is conveniently done in the case of silver films in the visible region by the use of total internal reflection optics which provide excitation of the bulk silver film plasmons through evanescent coupling.

The theory and mechanism of photon-excited bulk and surface plasmons has been extensively treated.⁽⁵¹⁻⁵³⁾ Chen *et al.* showed in 1976 that excitation of a 500-Å thick silver film, at the appropriate angle under total internal reflection conditions, resulted in the excitation of surface plasmons.⁽⁵⁴⁾ A specific well-defined angle of incidence is required in order to match the momentum components parallel to the surface for the photons and the surface plasmons. Under these conditions, the light intensity at the interface between the silver film and the ambient environment exceeds that of the incoming light up to two orders of magnitude, a substantial enhancement. Chen *et al.* suggested the application of this technique to Raman spectroscopy. In 1979 a number of groups demonstrated that this geometry can be used to obtain Raman and fluorescence spectra from thin films deposited on the silver support.⁽⁵⁵⁻⁵⁸⁾ A particularly nice demonstration is the study by Benner *et al.*,⁽⁵⁶⁾ using a strontium titanate hemi-cylinder with silver deposited on one part and not on the other. It is convenient to use a hemi-cylinder which facilitates determination of the precise coupling angle.

Although the silver plasmon enhancement method has not been used for the study of polymer monolayers to any great extent, it obviously has considerable potential. It has been used for the study of phospholipids and related monolayers by Dupeyrat and his coworkers where Raman spectra from films as thin as 75 Å have been detectable.⁽⁵⁷⁻⁵⁸⁾ A detailed treatment of the entire methodology has recently appeared.⁽⁵⁹⁾

As long as the coupling requirements are met, the surface plasmon will be excited. This condition can be achieved through the use of appropriate surface geometries, such as by putting the silver film on a suitably prepared diffraction grating. This technique has been pioneered by the group at IBM Research Labs in San Jose.⁽⁶⁰⁻⁶¹⁾ Another approach is to use evanescent coupling via the so called "Otto-geometry" as opposed to the Kretschmann geometry which used classical ATR methods.⁽⁵⁵⁾

It is generally accepted that a 500-Å uniform silver film deposited on the appropriate dielectric results in the optimum bulk and surface plasmon enhancement. Therefore, one can begin to consider the silver film as a

sensor or probe. If one now places a polymer surface in contact with it, in principle, one would obtain a spectrum of that interfacial region. Clearly this technique has some potential for polymer surface analysis.

3.5. SURFACE-ENHANCED RAMAN SPECTROSCOPY (SERS)

During the last ten years, a technique has become available which utilizes external reflection from silver island films (as opposed to the continuous film discussed in the previous section) producing enhancements in the Raman signal of 10^3 to 10^6 . This method, called surface-enhanced Raman scattering or SERS, is being studied as a means to greatly enhance the Raman scattering of monolayers and interfaces. The effect is believed to be due to at least two component mechanisms. One nonspecific component is due to the unique dielectric properties of very thin silver colloids which results in a local intensity enhancement of perhaps 10^3 to 10^4 . The other component may be due to more specific silver surface effects. Whatever the exact nature of the mechanisms, thin silver island films are useful as probes. Submonolayers of various species can be deposited on these films and respectable Raman spectra obtained in short times. This method has been used in a very limited way to study polymer surfaces by Murray and Allara at Bell Laboratories⁽⁶²⁾ and has been used to study biomolecules by Cotton *et al.*⁽⁶³⁾ The method is described in detail by Cotton in Volume 2. A recent monograph is also available.⁽⁶⁴⁾ It certainly merits consideration as a means for the study of polymer thin films.

4. INSTRUMENTAL IMPROVEMENTS

There have been significant advances in the last several years in the components of Raman spectrometer systems. Most notable has been the development of optical multichannel analyzers (OMA), which allows a significant proportion of the total Raman spectrum to be detected in real time through the use of intensified photodiode array or vidicon type detectors.⁽⁶⁵⁾ These OMA's allow an increased throughput and therefore an increase in signal-to-noise by a factor of approximately 100 or more.⁽⁶⁶⁾ Advances have been made in the design of spectrometers and their gratings which allow more efficient throughput of the Raman scattered light and more efficient rejection of the Rayleigh scattered line.

The collection optics on the front end of the spectrometer have been optimized and improved considerably. The use of microscope optics has not only permitted the development of micro-area or Raman probe techniques, which have been widely applied to polymer analysis, but has improved the overall collection efficiency for many Raman applications.⁽⁵⁹⁾

The continued extensive development in lasers and the recent development of truly simple trouble-free, easy to operate, tunable laser systems is making resonance Raman a useful routine analytical technique in many laboratories.

These many developments have permitted at least one group to obtain spectra of submonolayer quantities using conventional Raman, i.e., employing nonresonant methods and without any optical enhancements.⁽⁶⁷⁾

5. CONCLUSION

Although Raman spectroscopy is certainly not a routine or well-known technique for the characterization of polymer surfaces today, the methods we have outlined for enhancing the Raman signal, coupled with continued advances in instrumentation, certainly lead us to anticipate that Raman spectroscopy of polymer surfaces will be widely applied in the near future and can be expected to be a common routine polymer surface characterization method in the not very distant future.

ACKNOWLEDGMENTS

We acknowledge discussions with R. E. Benner and R. A. Van Wagenen, University of Utah, on various aspects of Raman and fluorescence spectroscopy; J. D. Andrade acknowledges discussions with P. Barber, Clarkson College, and R. K. Chang, Yale University. We also acknowledge discussions and assistance of J. Swalen and J. Raybolt, IBM, San Jose. Preparation of the chapter was aided in part by NIH grants HL18519 and HL07520. We thank R. E. Benner for assistance in the theoretical aspects of Raman spectroscopy, silver plasmon enhancement, and SERS.

REFERENCES

1. J. G. Grasselli, M. K. Snavely, and B. J. Bulkin, Applications of Raman spectroscopy, *Physics Reports* **65**, 231-344 (1980).
2. D. J. Cutler, P. J. Hendra, and G. Frasier, Laser Raman spectroscopy of synthetic polymers, in: *Developments in Polymer Characterisation* (J. V. Dawkins, ed.), Vol. 2, pp. 71-143, Applied Science, London (1978).
3. P. J. Hendra, Raman spectroscopy, in: *Polymer Spectroscopy* (D. O. Hummel, ed.), pp. 151-188, Verlag Chemie, Deerfield Beach, Florida (1980).
4. P. J. Hendra, Laser Raman study of polymers, *Adv. Polym. Sci.* **6**, 151-169 (1969).
5. R. G. Snyder, Infrared and Raman spectra and polymers, in: *Polymers, Part A* (R. A. Fava, ed.), pp. 73-148, Academic Press, New York (1980).
6. B. Jasse and J. L. Koenig, Orientational measurements in polymers using vibrational spectroscopy, *J. Macromol. Sci., Rev.* **C17**, 61-135 (1979).

Surface and Interfacial Aspects of Biomedical Polymers

Volume 1
Surface Chemistry and Physics

Edited by
Joseph D. Andrade

University of Utah
Salt Lake City, Utah

1985 470 P6

PLENUM PRESS • NEW YORK AND LONDON

58. M. Delhaye, M. Dupeyrat, R. Dupeyrat, and Y. Levy, An improvement in the Raman spectroscopy of very thin films, *J. Raman Spectrosc.* **8**, 351-353 (1979).
59. A. Aurengo, Y. Levy, and R. Dupeyrat, Optimization of ultrathin film nonresonant Raman spectra provided by combining a light-trapped device, a high N.A. objective and a spectrometer, *Appl. Opt.* **22**, 602-608 (1983).
60. A. Girlando, M. R. Philpott, D. Heitmann, J. D. Swalen, and R. Santo, Raman spectra of thin organic films enhanced by plasmon surface polaritons on holographic metal gratings, *J. Chem. Phys.* **72**, 5187-5191 (1980).
61. W. Kohl, M. R. Philpott, J. D. Swalen, and A. Girlando, Surface plasmon enhanced Raman spectra of monolayer assemblies, *J. Chem. Phys.* **77**, 2254-2260 (1982).
62. C. A. Murray and D. L. Allara, Measurement of the molecule-silver separation dependence of surface enhanced Raman scattering in multilayered structures, *J. Chem. Phys.* **76**, 1290-1303 (1982).
63. T. M. Cotton, S. G. Schultz, and R. R. Van Duyne, Surface-enhanced resonance Raman scattering from water-soluble porphyrins adsorbed on a silver electrode, *J. Am. Chem. Soc.* **104**, 6528-6533 (1982).
64. R. K. Chang and T. E. Furtak, *Surface Enhanced Raman Scattering*, Plenum Press, New York (1982).
65. Y. Talmi, ed., *Multichannel Image Detectors*, ACS Symp. Ser. **102** (1979).
66. J. J. Freeman, J. Heaviside, P. J. Hendra, J. Prior, and E. S. Reid, Raman spectroscopy with high sensitivity, *Appl. Opt.* **35**, 196-205 (1981).
67. A. Campin, J. K. Brown, and V. M. Orizzle, Surface Raman spectroscopy without enhancement, *Surface Sci.* **115**, 153-158 (1982).

Evanescent Detection of Adsorbed Protein Concentration-Distance Profiles: Fit of Simple Models to Variable-Angle Total Internal Reflection Fluorescence Data

W. M. REICHERT,* P. A. SUCI, J. T. IVES, and J. D. ANDRADE

Department of Bioengineering, and Center for Biopolymers at Interfaces, University of Utah, Salt Lake City, Utah 84112

Total internal reflection fluorescence spectroscopy (TIRF) is an established technique for following the course of interfacial reactions. Theoretically, by gathering TIRF data as a function of observation angle, one can obtain the density of fluorophores with respect to distance away from a solid/liquid interface. In order that the practical application of the theory might be explored, variable observation angle data from solutions of fluorescein and from adsorbed layers of fluorescein isothiocyanate labeled immunoglobulin have been analyzed in terms of simple concentration-distance profiles. In all cases the general shape of the data curves was found to conform to the theoretical expectation. Layer thickness determinations varied over a range of 20 to 100 nm, with concentrations in the layer ranging from 12 to 61 mg/mL. The theoretical background, sources of error, and system improvements are also discussed.

Index Headings: Analysis for protein adsorption; ATR spectroscopy; Fluorescence; Surface analysis.

INTRODUCTION

Total internal reflection fluorescence (TIRF) has provided a sensitive, real-time, interfacial technique for detecting the fluorescence of proteins as they adsorb from solution to the solid/liquid interface.^{1,2} Variable-angle total internal reflection fluorescence (VA-TIRF) has been used to determine the depletion layer thickness of fluorescent macromolecules near an interface.^{3,4} In the same manner VA-TIRF should provide a mechanism for calculating the concentration-distance profile of an interfacially adsorbed fluorescent protein layer. We contend that this variable-angle fluorescence technique is a quantitative alternative to fixed-angle TIRF, multiple total internal reflection infrared spectroscopy, and ellipsometry, as well as to the ultra-high-vacuum techniques of variable-angle x-ray and Auger photoelectron spectroscopy.

There exist two basic approaches for finding the concentration profile of fluors from VA-TIRF data: (1) make a guess of the general form of the profile, which can be expressed explicitly in an equation, $c(z)$, and then calculate how the estimated curve fits the data; or (2) use an inverse Laplace transform numerical method to construct $c(z)$ by expressing the fluorescence data in terms of the Laplace transform. Here we used the first approach to test the fit of VA-TIRF data to two simple concentration profiles: a fluorescein solution approximated by a constant function and a fluorescein labeled protein film approximated by a step function. This study concludes that VA-TIRF data from an adsorbed protein

layer conform to a Laplacian format. Application of the second approach for the numerical reconstruction of more complex protein concentration-distance profiles directly from the collected fluorescence data is discussed.

VA-TIRF THEORY

Fluorescence Excited Within the Evanescent Volume.

Consider two transparent dielectric media of different optical densities sharing a common boundary. The total internal reflection phenomenon occurs when light propagating the more optically dense medium (n_1) strikes the boundary with the less dense medium (n_2) at an incident angle (θ_i) greater than the critical angle (θ_c), which forces the refracted light to travel parallel to the interface (Fig. 1a). From Snell's law ($n_1 \sin \theta_i = n_2 \sin \theta_2$) this critical condition ($\theta_i = \theta_c$ and $\theta_2 = \pi/2$) is calculated as $\theta_c = \sin^{-1}(n_2/n_1)$, where n_1 and n_2 are the refractive indices of the more and less dense media, respectively ($n_1 > n_2$).

If θ_i is increased beyond θ_c then θ_2 becomes complex ($\theta_2 = \pi/2 + i\beta$, where $\beta = \cos^{-1}[n_1 \sin \theta_i/n_2]$), causing the refracted beam to rejoin the slightly shifted reflected beam (Fig. 1b).⁵⁻⁷ This situation produces a zero net flux of light energy across the interface because all of the incident light is eventually reflected back into the more dense medium; hence the term total internal reflection. However, the electromagnetic boundary conditions require a small fraction of the incident intensity to penetrate the interface into the less dense medium before rejoining the totally reflected beam. The intensity of this interfacial field, typically called the "evanescent wave," decays exponentially with distance away from the totally reflecting interface into the less dense medium (decays essentially to zero within one wavelength's distance normal to the interface). The absorption or scattering of the evanescent wave within the interfacial region of the less dense medium is the basis of all total internal reflection spectroscopies.

The fluorescence intensity excited in a given volume is proportional to the product of the fluor concentration and the intensity of the exciting light contained within that volume. In the TIRF configuration the fluorescence intensity emitted from a differential volume of the less dense medium a distance z below the totally reflecting interface is proportional to:

$$c(z)I_e(\theta_i)\exp[-s(\theta_i)z] \quad (1)$$

where $c(z)$ is the concentration of fluors in the plane defined by the distance z and $I_e(\theta_i)\exp[-s(\theta_i)z]$ is the light intensity (per unit area) of the evanescent wave at

Received 28 August 1986.

* Author to whom correspondence should be sent.

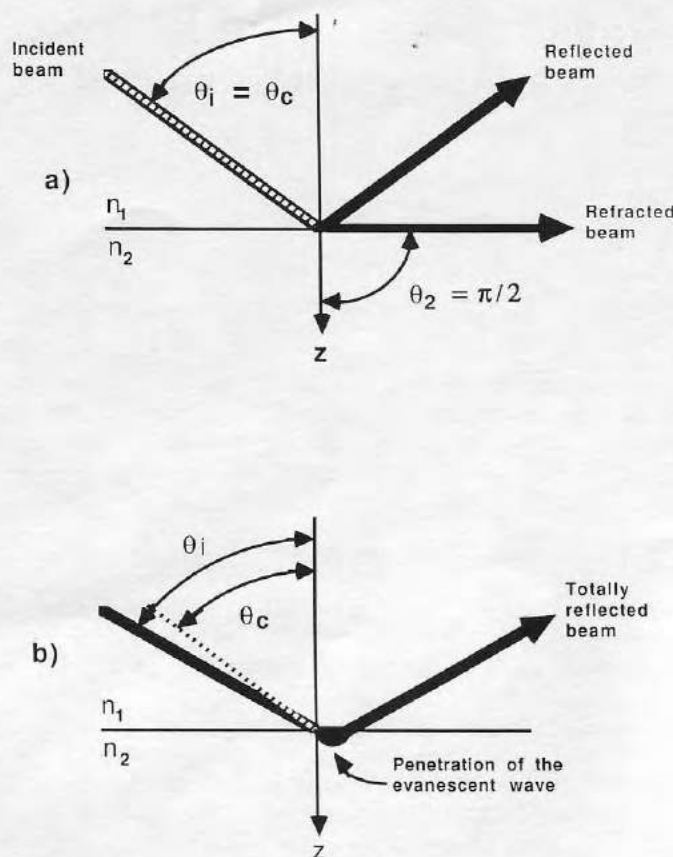


FIG. 1. Illustration of the total internal reflection phenomenon: (a) for incident angle equal to the critical angle and (b) for incident angle greater than the critical angle (note the penetration of light across the interface).

the distance z which has decayed exponentially from the value transmitted across the interface at $z = 0$. For transparent media where $n_1 > n_2$ and $\theta_i > \theta_c$, we have for perpendicular polarized light:

$$s(\theta_i) = (4\pi/\lambda_i) [(n_1 \sin \theta_i)^2 - n_2^2]^{1/2} \quad (2a)$$

$$l_i(\theta_i) = l_i |t(\theta_i)|^2 \quad (2b)$$

where λ_i is the vacuum wavelength of the totally reflected beam, l_i is the incident light intensity and $|t(\theta_i)|^2$ is the magnitude squared of the Fresnel transmission coefficient given by:

$$|t(\theta_i)|^2 = 4 \cos^2 \theta_i / [1 - (n_2/n_1)^2]. \quad (2c)$$

The total fluorescence is proportional to the summation of all of the fluorescing differential volumes in the region bounded by the intensity of the evanescent wave. In the limit, the total fluorescence excited in the "evanescent volume" is given by the integral (see Ref. 1, Chap. 2):

$$F(\theta_i) = k_i \epsilon \phi A_i I_i |t(\theta_i)|^2 \int_0^\infty c(z) \exp[-s(\theta_i)z] dz \quad (3)$$

where ϵ is the extinction coefficient and ϕ is the fluorescence quantum efficiency, A_i is the area illuminated by the totally reflected incident beam, and k_i is a proportionality constant.

From Eqs. 2a-2c it can be shown that a continual increase in θ_i beyond the critical angle for total reflection

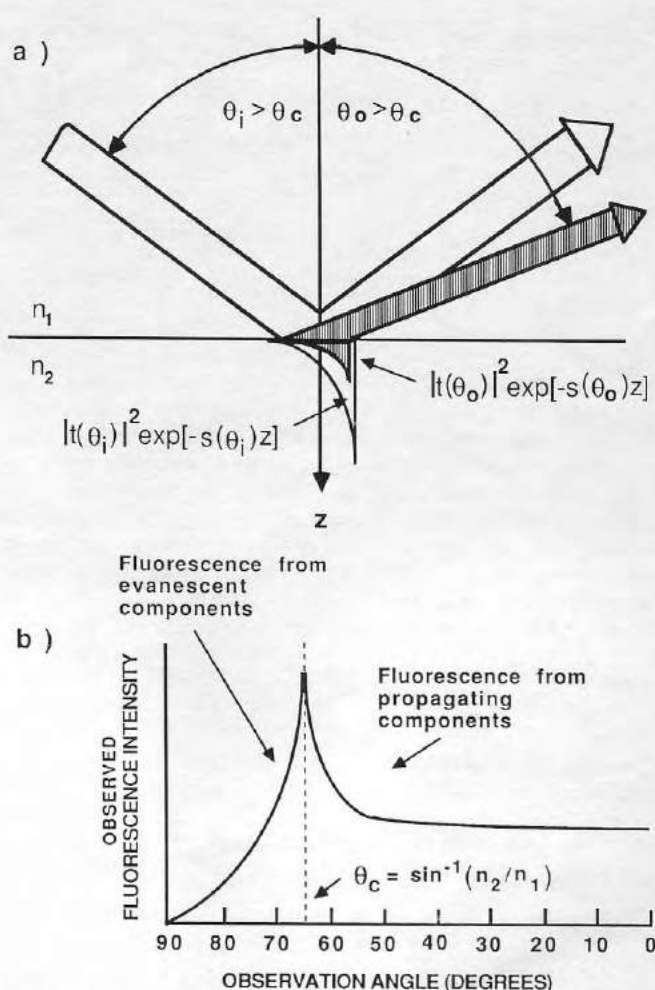


FIG. 2. Illustration of the principle of reciprocity as applied to VA-TIRF: (a) concept of the two superimposable evanescent fields representing the excitation and observation evanescent volumes (note: this is a simple construct presented for the purposes of illustration); and (b) calculated variable observation fluorescence spectrum from fluors emitting from the water side of a quartz/water interface.

simultaneously causes: (1) a decrease in the intensity transmitted across the interface into medium n_2 ($|t(\theta_i)|^2$ decreases); and (2) an increase in the decay rate of the evanescent wave in medium n_2 ($s(\theta_i)$ increases). These factors reduce the "size" of the evanescent volume, which, in turn, reduces the amount of evanescently excited fluorescence ($F(\theta_i)$). The above relationship between $F(\theta_i)$ and $s(\theta_i)$ means that Eq. 3 can also be expressed as a function of the decay factor $s(\theta_i)$:

$$F[s(\theta_i)] = k_i \epsilon \phi A_i I_i |t(\theta_i)|^2 \int_0^\infty c(z) \exp[-s(\theta_i)z] dz. \quad (4)$$

Observation of Evanescently Excited Fluorescence. Variable-angle TIRF (VA-TIRF) is based on the principle that the collected fluorescence intensity is a function of three parameters: (1) the amount of light intensity in the evanescent volume available to excite fluorescence, (2) the distribution of fluors in the evanescent volume, and (3) the amount of evanescently excited fluorescence that couples back across the totally reflecting interface and propagates at a given angle to the photodetector. The first and second parameters are ac-

counted for by Eq. 4. The third parameter, the observed fluorescence, is regulated by the observation angle θ_o through the principle of reciprocity, which, in this context, is essentially a reverse total reflection phenomenon.

In order to better understand the role of the observation angle, again consider the two transparent dielectric media $n_1 > n_2$ (Fig. 2a). Snell's law and basic electromagnetic theory state that light propagating from n_1 onto the n_1/n_2 interface at an angle $\theta_i > \theta_c$ will create an evanescent wave in n_2 confined to the equation $|t(\theta_i)|^2 \exp[-s(\theta_i)z]$ (see Eqs. 1 and 2). Conversely, light emanating from the n_2 side of the n_1/n_2 interface and propagating into n_1 at an angle $\theta_o > \theta_c$ must originate from an evanescent source in n_2 governed by the equation $|t(\theta_o)|^2 \exp[-s(\theta_o)z]$. The form of $|t(\theta_o)|^2$ and $s(\theta_o)$ for perpendicular polarized light is identical to that of Eq. 2 where θ_o and λ_o is substituted for θ_i and λ_i . This reciprocity argument can be applied to the field emitted by a fluor near a dielectric interface.

The angular spectrum representation of a plane wave decomposes the field emitted from a fluor into evanescent and propagating components.⁸ Therefore, it follows from the principle of reciprocity that the evanescent components of the fluorescence excited in n_2 will propagate in n_1 only at angles greater than the critical angle (Fig. 2b). A similar analysis of Snell's law concludes that the propagating dipole emission will be observed in n_1 only at angles less than the critical angle. In this paper the fluorescent emission is excited by the evanescent wave while the observed signal is collected from the evanescent components of the near field fluorescent dipole emission.^{9,10} This complicated process can be thought of as exciting and collecting fluorescence from two different evanescent volumes superimposed upon one another (Fig. 2a). Given a fixed incident angle θ_i and a fixed observation angle θ_o where $\theta_i > \theta_c < \theta_o$, one excites emission from the fluors contained within the evanescent excitation volume:

$$F[s(\theta_i)] = k_i \epsilon \phi A_i I_i |t(\theta_i)|^2 \int_0^\infty c(z) \exp[-s(\theta_i)z] dz \quad (5a)$$

and collects the fluorescence that is contained within the evanescent observation volume:

$$F[s(\theta_o)] = k_o A_o |t(\theta_o)|^2 \int_0^\infty \exp[-s(\theta_o)z] dz \quad (5b)$$

where A_o is the interfacial area subtended by the cone of collection and k_o is another proportionality constant. The fluorescence excited at θ_i and collected at θ_o is therefore given by the product of the two integrals in Eqs. 5a and 5b:

$$F[s(\theta_i) + s(\theta_o)] = K |t(\theta_i)|^2 |t(\theta_o)|^2 \int_0^\infty c(z) \exp[-[s(\theta_i) + s(\theta_o)]z] dz \quad (6)$$

where $K = k_i \epsilon \phi I_i A_i k_o A_o$.

In our VA-TIRF design one picks a fixed incident angle θ_i to produce a constant excitation evanescent volume and varies the observation angle from slightly less

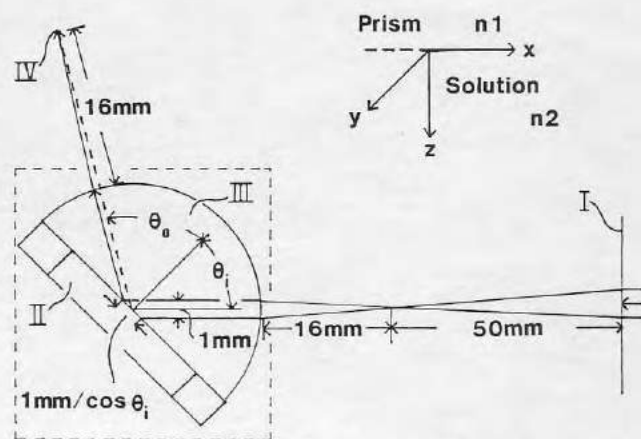


FIG. 3. Schematic of VA-TIRF design. Incident angle is adjusted by rotation of the prism. Observation angle is adjusted by rotation of the fiber around the prism. Sectioned-off segment is drawn to scale. Coordinate system located in upper right hand corner. I: 5-cm-focal-length cylindrical lens; II: solution chamber; III: cylindrical prism; IV: position of fiber at focal plane of prism.

than the critical angle ($\theta_o < \sin^{-1}(n_2/n_1)$) to the glancing angle ($\theta_o = \pi/2$). The resultant angular spectrum samples the fluorescence from molecules in a sequence of decreasing observation volumes (or near field emissions) that are increasingly confined to the interface with increasing observation angles.

VA-TIRF and the Laplace Transform. Normalization of the collected fluorescence to the incident and observation Fresnel terms yields:

$$F'[s(\theta_i) + s(\theta_o)] = F[s(\theta_i) + s(\theta_o)] / [K |t(\theta_i)|^2 |t(\theta_o)|^2] \\ = \int_0^\infty c(z) \exp[-[s(\theta_i) + s(\theta_o)]z] dz \quad (7)$$

The normalized fluorescence can be expressed in terms of the Laplace transform if we define the function s as:

$$s = s(\theta_i) + s(\theta_o). \quad (8)$$

Substitution of Eq. 8 into Eq. 7 yields:

$$L[c(z)] = \int_0^\infty c(z) \exp(-sz) dz = F'(s). \quad (9)$$

The Laplace transform (Eq. 9) maps the function c of the variable z into the function F' of the variable s . Therefore, the Laplace transform of the concentration-distance profile of fluors near the interface is the expression for the normalized VA-TIRF fluorescence spectrum.

EXPERIMENTAL

All of the experimental and theoretical work discussed in this paper is described in detail elsewhere.¹¹ Figure 3 illustrates the central components of the VA-TIRF apparatus. An argon laser provided the excitation light with an incident angle of 75° ($\lambda_i = 488$ nm). Incident angle variation was minimized by a cylindrical lens (5 cm f.l.)

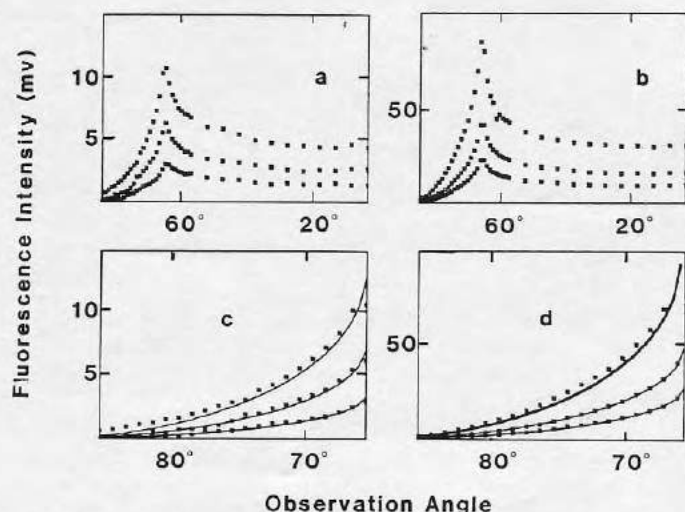


FIG. 4. VA-TIRF data for various concentrations of fluorescein. Concentrations (mg/mL) from top to bottom are 0.2, 0.1, and 0.05 for plots (a) and (c), and 3.125, 1.0, and 0.5 for plots (b) and (d). Solid lines in (c) and (d) are best fits of Eq. 13 to (a) and (b), respectively.

which focuses the beam on the focal plane of the hemicylindrical prism (Harrick Scientific; $n = 1.4633$ at 488 nm; $n = 1.46648$ at 514 nm). The focal plane refers to a cylindrical surface a distance d from the curved prism surface defined by $d = [n_1/(n_1 - n_2)]R$, where R is the prism radius. We mounted the prism on a rotation stage to adjust the incident angle and rotated the collection optics around the prism in order to adjust the observation angle. The fluorescence was detected at $\lambda_0 = 514$ nm by an IP-21 photomultiplier tube (PMT) with current-voltage electronics and a Hewlett-Packard 3478a multimeter. The laser light from the totally reflected laser beam was blocked from the collection device by two Pomfret 488-nm notch filters.

Fluorescence was gathered at the focal plane of the prism. Since all rays which leave the interface at one particular angle converge at an arc in this plane, the observation angle was well defined. A short optical fiber (2.2 cm long, 600 μ m core, plastic clad silica, step index, numerical aperture = 0.4) was used to collect flu-

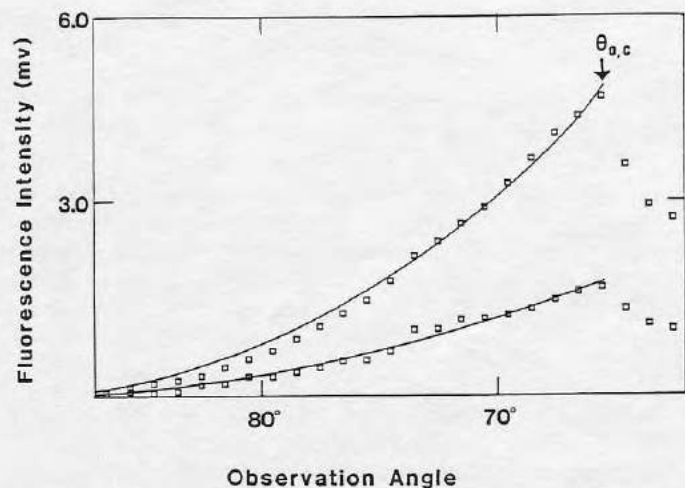


FIG. 5. VA-TIRF data taken from an adsorbed layer of FITC-IgG. Upper curve: after 30 min desorption, lower curve: after 60 min desorption. Solid lines are the best fits of Eq. 14 to these data.

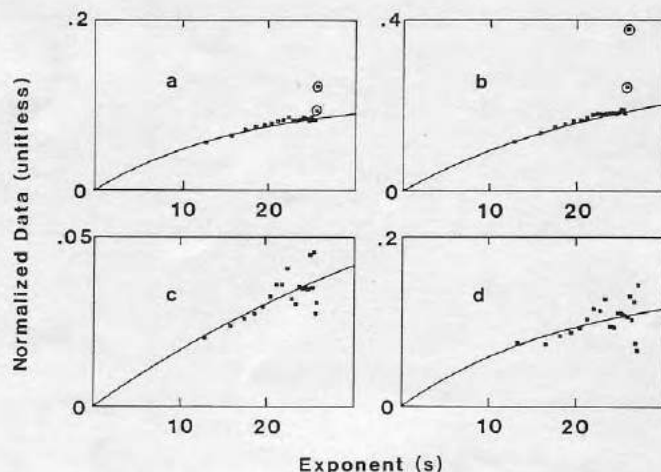


FIG. 6. VA-TIRF data from the protein layers (Fig. 5) normalized to the fluorescein solution data (Fig. 4): (a) first wash normalized to 3.125 mg/mL; (b) first wash normalized to 1.0 mg/mL; (c) second wash normalized to 3.125 mg/mL; and (d) second wash normalized to 0.5 mg/mL. Solid lines are best fits of Eq. 15 to the data. Circled points were disregarded. The exponent s is given in Eq. 8.

orescence in the focal plane. A grin lens (Selfoc), placed behind the fiber, was used to collimate and guide the light to the sensing device.

Fluorescein (Sigma) solutions were chosen as the bulk fluorescence substance. Goat immunoglobulin (Miles) labeled with fluorescein isothiocyanate (Sigma) was chosen as the fluorescent protein. The labeling procedure, described elsewhere,¹² produced a fluor-to-protein molar labeling ratio of 4.6. All experiments used a static solution in a chamber adjacent to the prism surface (Fig. 3). In the fluorescently labeled IgG (FITC-IgG) experiments the protein was allowed to adsorb for 30 min and then the solution in the chamber was twice replaced by buffer solution (phosphate buffered saline) at 30-min intervals (first and second wash). Data were collected after each wash.

RESULTS

Fit of VA-TIRF Data to Simple Concentration Profiles. Two simple forms of the concentration profile were considered that yielded analytical solutions to the Laplace transform. A constant function was used to represent the concentration profile of a bulk fluorescein solution:

$$c(z)_b = c_b \text{ for } z \geq 0, \quad (10)$$

and a step function was used to represent the concentration profile of the adsorbed FITC-IgG protein layer.

$$\begin{aligned} c(z)_p &= c_p & \text{for } 0 \leq z \leq t_p \\ c(z)_p &= 0 & \text{for } z < 0 \text{ and } z > t_p \end{aligned} \quad (11)$$

where t_p is the thickness of the protein film. Taking the Laplace transform of Eqs. 10 and 11 by the integration of Eq. 6 yields the following angular fluorescence profiles for the fluorescein solution and protein film, respectively:

$$F(s)_b = K_b c_b |t(\theta_i)|^2 |t(\theta_o)|^2 (1/s). \quad (12)$$

$$F(s)_p = K_p c_p |t(\theta_i)|^2 |t(\theta_o)|^2 (1/s) [1 - \exp(-st_p)] \quad (13)$$

where $K_b = k_i \epsilon_b \phi_b l_i A_i k_o A_o$, $K_p = k_i \epsilon_p \phi_p l_i A_i k_o A_o$, and s is given in Eq. 8.

Figure 4a and 4b are raw VA-TIRF data from various concentrations of fluorescein in solution. In accordance with the theory, all the fluorescence curves have a peak at the critical observation angle ($\theta_{c,o} = \sin^{-1}(n_2/n_1)$). Figure 4c and 4d are the "best fits" of Eq. 12 to the data presented in Fig. 4a and 4b for $\theta_{c,o} < \theta_o < \pi/2$. $|t(\theta_i)|^2$, $|t(\theta_o)|^2$, and $s(\theta_i, \theta_o)$ were calculated from Eqs. 2a–2c and Eq. 8, while the product $K_b c_b$ was adjusted (via a least-squares routine) until a best fit to the data was obtained. This analysis showed good adherence of the fluorescence data to the shape predicted from the Laplace transform.

Figure 5 presents VA-TIRF data from an adsorbed FITC-IgG layer. The variable-angle data from the IgG layer after both washes peaked at 65.5°, indicating that the effective interfacial refractive index remained at 1.333. Equation 13 was fit to the data in Fig. 5 (solid lines) in the same manner as above, except that the product $K_p c_p$ and the thickness t_p were adjusted until a best fit was obtained. Again we see a good approximation of the shape of the fluorescence curve as predicted from the Laplace transform.

Estimation of Protein Film Thickness and Concentration: Normalized VA-TIRF Data. The best fit of Eq. 13 to the data in Fig. 5, after the first wash, was obtained with a layer thickness of 18 nm. After the second wash, the layer thickness needed to achieve a best fit approached zero. A layer thickness of 18 nm is within the range expected on the basis of the size of IgG.¹³ However, a layer thickness which approaches zero means all of the functionality in the measured fluorescence values (with respect to angle) arises from the change in the observation Fresnel term, $|t(\theta_o)|^2$.¹¹ This result prompted an attempt to fit an analytical expression to values we obtained by normalizing the protein data to fluorescein solution data. It was anticipated that normalization would eliminate the erroneous effects attributed to the Fresnel terms.

If one assumes that the interfacial conditions for the fluorescein solution and protein film are the same (i.e., the interfacial refractive indices and Fresnel terms in all experiments are assumed to be identical and real), then from Eqs. 12 and 13 the normalization of the protein variable-angle data (Fig. 5) to the fluorescein solution data (Fig. 4) should fit the equation:

$$F(s)_p/F(s)_b = K'[1 - \exp(-st_p)] \quad (14)$$

where $K' = \epsilon_p \phi_p c_p / \epsilon_b \phi_b c_b$. The best fit of Eq. 14 to the normalized protein data was performed by the numerical adjustment of the constant K' and thickness t_p until the difference between theory and experiment reached a minimum. The most convincing fits of Eq. 14 to the normalized data sets are presented in Fig. 6. We present the abscissa points in Fig. 6 in terms of the exponent s (calculated from Eqs. 2 and 8) in order to present the data as a Laplace transform (see Eq. 9). At large observation angles the voltage signal from the PMT was quite small; thus the scatter in the data at large values of s . We calculated fits to three of the four normalized data sets by neglecting data points that deviated radically from the expected result. The parameter χ in Table I is

TABLE I. Estimated protein layer thickness and concentration.

c_b (mg/mL)	t_p (nm)	c_p (mg/mL)	κ_p ($\times 10^3$) ^a	κ_b ($\times 10^3$)	Angular range	χ^b
Wash 1						
3.125 (a) ^c	60	61	17.0	5.0	66.5–83.5	0.042
1.0 (b)	40	53	14.0	1.6	66.5–83.5	0.028
0.5	100	25	7.0	0.8	65.5–85.5	0.061
0.1	60	24	6.6	0.2	65.5–85.5	0.143
0.05	40	33	9.0	0.08	65.5–84.5	0.105
Wash 2						
3.125 (c)	20	52	14.0	5.0	66.5–85.5	0.223
1.0	20	36	9.8	1.6	66.5–83.5	0.004
0.5 (d)	50	13	3.6	0.8	65.5–85.5	0.231
0.1	40	12	3.3	0.2	65.5–84.5	0.316
0.05	40	12	3.3	0.08	65.5–85.5	0.099

^a Values of κ_p calculated from the protein solution absorption index value ratioed to the estimated surface concentration values listed above.

^b χ is the average distance of data points from the theoretical curve normalized to the average magnitude of the data points.

^c Values labeled (a), (b), (c), and (d) are plotted in Fig. 6a–6d, respectively.

a measure of closeness of the best fit of the curve to the data.

The protein layer concentration, c_p , was calculated from rearrangement of the constant K' :

$$c_p = K' c_b [\epsilon_b \phi_b / \epsilon_p \phi_p]. \quad (15)$$

The ratio $\epsilon_b \phi_b / \epsilon_p \phi_p$ was determined experimentally from the ratio of the quantum yields in a right-angle fluorescence configuration where the quantum yields of solution and adsorbed protein are assumed to be the same.¹¹ Table I lists all values of calculated protein film thickness and concentration of the protein layer normalized to each fluorescein solution concentration, the angular range over which the curve fitting was performed, and the absorption index, κ , calculated spectrophotometrically for the protein solution (κ_p) and for each fluorescein solution (κ_b) where $\kappa = \epsilon c \lambda_i / 4 \pi n$. Note that all calculated values of layer thickness yielded nonzero results. The accepted literature values for adsorbed IgG thickness and concentration are 10–15 nm and 100–200 mg/mL.^{1,12–14} A comparison of Table I with the literature indicates that our estimates of protein layer thickness and concentration are high and low, respectively.

DISCUSSION

Estimated Profiles: The Laplace Transform. Although the size of IgG is well known, its conformation on a given surface and the uniformity of its layer formation are not well characterized.^{13,14} As presented here, the variable-angle technique for obtaining concentration-distance profiles of proteins is based upon a relatively simple mathematical model: the Laplace transform of the concentration-distance profile results in the fluorescence data curve. This model is completely valid only when applied to measurements of materials which do not significantly alter: (1) the refractive index at the interface, (2) the intensity in the evanescent wave through the absorption of light, and (3) their interfacial concentration profile over the measurement duration.

Errors resulting from deviations in the interfacial refractive index or through optical absorption are apt to have a more pronounced effect when this model is applied to characterization of adsorbed layers than when applied to characterization of depletion layers.^{3,4} The observation angles at which peak fluorescence values are obtained (Fig. 5) indicate that the protein layers are hydrated, producing a refractive index at the interface that is not altered appreciably from that of a quartz/water interface. Additionally, the low values of κ listed in Table I for the protein layer and fluorescein solutions (on the order of 10^{-6} to 10^{-4}) are several orders of magnitude too small to have a significant effect.

Figure 5 presents the best fit of a step profile (Eq. 13) to the raw VA-TIRF data from the protein layer. Normalizing the protein data to fluorescein data (Eq. 14) should improve the fit of the collected fluorescence to the proposed model by elimination of the Fresnel term $|t(\theta_0)|^2$. This term (Eq. 2c) is responsible for a substantial amount of the change in fluorescence intensities at different observation angles, but does not contribute to concentration-distance profile information.¹¹ The shapes of the normalized data curves presented in Fig. 6 are also indicative of a step profile. Unfortunately, the relative weight of the noise increases upon normalization, especially with data curves of protein which have low fluorescence values. This effect could be reduced if it were possible to separate out a contribution to the error specifically attributable to the Fresnel term.

The desorption of the protein from the interface during the data collection process, the inherently diffuse nature of a protein layer, and the interfacial scatter of light are other possible sources of error. Efforts to determine their contribution would require an improved signal-to-noise ratio of the collected fluorescence and the testing of the improved system with samples having well-characterized interfacial concentration profiles.

Reconstructed Profiles: The Inverse Laplace Transform. It is generally accepted that proteins do not adsorb to surfaces in homogeneous dielectric films of uniform thickness, but are osmophilic and diffuse.¹ Unfortunately, virtually every technique used to quantitate the surface concentration of adsorbed protein films assumes that they adsorb in homogeneous films of uniform thickness and concentration. An exception is variable-angle x-ray photoelectron spectroscopy, which has been used to determine the concentration profile of surface films with the use of numerical techniques^{15,16} and models for patchy layers.¹⁷ However, ultra-high-vacuum techniques are a poor approximation of ambient conditions. It is therefore important to develop a method that is capable of quantitatively analyzing more complex interfacial concentration profiles of samples in the hydrated state.

If $F'(s)$ is the Laplace transform of $c(z)$, then it is possible to construct the function $c(z)$ from $F'(s)$ via the inverse Laplace transform:

$$L^{-1}[F'(s)] = c(z). \quad (16)$$

Theoretically, this approach provides a method for calculating the concentration profile of fluorescing molecules within the interfacial region directly from the inverse Laplace transform of the normalized VA-TIRF data (Eq. 9).

The conformity of the VA-TIRF data presented in this paper to the proposed simple solutions to the Laplace transform (Eqs. 12 and 13) was encouraging. However, the noise in the collected fluorescence data must be reduced before a numerical inverse transform will produce a meaningful result. Efforts to improve the signal-to-noise level are being made through the adaptation of an x-ray goniometer as the rotating sample stage and the development of a quartz fiber array collection system compatible with a double monochromator with photon counting. Finally, in order for the numerical inversion method to be useful quantitatively, it needs to be tested on systems with well-defined concentration-distance profiles. The current experimental effort involves construction of a standard set of concentration-distance profiles of dye-impregnated fatty acid layers with the use of the Langmuir-Blodgett technique.¹⁸ Existing software for inversion of the Laplace transform¹⁹ is being adapted to predict the shape of these profiles from the variable-angle data. If the standard profiles are reconstructed numerically with some degree of accuracy, then the more diffuse protein system will be re-examined in greater depth.

ACKNOWLEDGMENTS

This project was funded by University of Utah Research Committee seed grants and student fellowships (P.A.S.), by NIH grants HL-18519 and HL-23132, and by the Office of Naval Research. The current experimental effort is funded by the Center for Biopolymers at Interfaces at the University of Utah. Helpful discussions with V. Hlady and R. E. Benner were appreciated. Special appreciation is given to F. Rondelez, whose seminar inspired this project.

1. *Surface and Interfacial Aspects of Biomedical Polymers: Protein Adsorption*, J. D. Andrade, Ed. (Plenum Press, New York, 1985), Vol. 2.
2. D. Axelrod, T. P. Burghardt, and N. L. Thompson, *Ann. Rev. Biophys. Bioeng.* **13**, 247 (1984).
3. C. Allain, D. Ausserre, and F. Rondelez, *Physical Rev. Lett.* **49**, 1694 (1982).
4. J. M. Bloch, M. Sansone, F. Rondelez, D. G. Peiffer, P. Pincus, M. W. Kim, and P. M. Eisenberger, *Physical Rev. Lett.* **54**, 1039 (1985).
5. R. H. Renard, *J. Opt. Soc. Am.* **54**, 1190 (1964).
6. I. Godeny, F. J. Kedves, and D. Beke, *Am. J. Physics* **45**, 550 (1977).
7. A. I. Mahan and C. V. Bitterli, *Appl. Opt.* **17**, 509 (1978).
8. P. C. Clemmow, *The Plane Wave Spectrum Representation of Electromagnetic Fields* (Pergamon Press, New York, 1966).
9. C. K. Carniglia, L. Mandel, and K. H. Drexhage, *J. Opt. Soc. Am.* **62**, 479 (1972).
10. E. H. Lee, R. E. Benner, J. B. Fenn, and R. K. Chang, *Appl. Opt.* **18**, 862 (1979).
11. P. A. Suci, Master's Thesis, Department of Bioengineering, University of Utah, Salt Lake City (1985).
12. S. A. Rockhold, R. D. Quinn, R. A. Van Wagenen, J. D. Andrade, and W. M. Reichert, *J. Electroanal. Chem.* **150**, 261 (1983).
13. M. E. Sonderquist and A. G. Walton, *J. Colloid Interface Sci.* **75**, 386 (1980).
14. P. Bagchi and S. M. Birnbaum, *J. Colloid and Interface Sci.* **83**, 460 (1981).
15. T. D. Bussing and P. H. Holloway, *J. Vac. Sci. Techn. A*(3), 1355 (1985).
16. R. S. Yih and B. D. Ratner, "A Comparison of Two Angular Dependent ESCA Algorithms Useful for Constructing Depth Profiles of Surfaces," submitted to *J. Elect. Spectrosc. Relat. Phenom.*
17. B. D. Ratner, T. A. Horbett, D. Shuttleworth, and H. R. Thomas, *J. Colloid Interface Sci.* **83**, 630 (1981).
18. K. H. Drexhage, "Interaction of Light with Monomolecular Dye Layers," in *Progress in Optics*, XII, E. Wolf, Ed. (North-Holland Press, New York, 1974), pp. 164-232.
19. D. Davies and B. Martin, *J. Computational Meth.* **33**, 1 (1979).

TOTAL INTERNAL REFLECTION FLUORESCENCE (TIRF) AS A QUANTITATIVE PROBE OF PROTEIN ADSORPTION

S.A. ROCKHOLD *, R.D. QUINN, R.A. VAN WAGENEN, J.D. ANDRADE ** and M. REICHERT

Department of Bioengineering, College of Engineering, University of Utah, Salt Lake City, UT 84112 (U.S.A.)

(Received 1st November 1982; in revised form 4th February 1983)

ABSTRACT

Total internal reflection fluorescence (TIRF) is a powerful new method for probing protein adsorption at solid–liquid interfaces. A quantitation method for determining the amount of adsorbed protein on hydrophilic glass and quartz surfaces has been developed. This method utilizes fluorescent, non-adsorbing dextran as a calibration molecule which approximates the diffusive properties of the protein under study. Through the use of conventional bulk solution fluorescence of both protein and calibration molecules in conjunction with a TIRF calibration, graphical quantitation of the surface concentration of adsorbed protein can be performed. Quantitative results can be obtained either via a graphical procedure using fluorescence calibration standards or by a numerical method which accounts for the characteristics of the decaying evanescent, interfacial wave. The graphical quantitation procedure is outlined and demonstrated with data from five gamma-globulin adsorption experiments on hydrophilic glass and quartz surfaces. The results generated by this quantitation procedure are similar to values derived from the numerical quantitation calculation.

INTRODUCTION

Total internal reflection fluorescence (TIRF) is a sensitive, interfacial technique capable of detecting fluorescent molecules adsorbed on or located within several tens of nm of a surface [1]. This technique utilizes an interfacial, evanescent, standing electromagnetic wave to excite fluorescence near an optical interface. TIRF has been used primarily to study the adsorption properties of macromolecules on various surfaces [1–5].

Because protein adsorption is an important step in biomaterial-induced thrombosis, there has been an active search for techniques capable of accurately studying this phenomenon. Many adsorption monitoring techniques currently exist but each has drawbacks and limitations. Unlike most other adsorption monitoring techniques, TIRF offers real time, in situ monitoring of a surface in the presence of adsorbing

* Submitted as partial fulfillment of the requirements of the M.Sc. Degree in Bioengineering, August 1982.

** To whom correspondence should be addressed.

material. However, TIRF has been limited by the lack of simple, straightforward procedures for quantitating the amount of adsorbed protein. TIRF also offers a unique advantage in that one can monitor the intrinsic fluorescence of the amino acids tyrosine and tryptophan which are constituents of most proteins. Intrinsic TIRF has proven to be successful [5] and unique since it avoids the need to label the molecule of interest thus eliminating the possibility of altering the proteins' physicochemical properties. Disadvantages of intrinsic fluorescence include enhanced Rayleigh scattering in the ultraviolet, increased susceptibility to protein photobleaching and photodegradation and the need for quartz optical components.

We report a study of gamma-globulin (IgG) adsorption using intrinsic tryptophan fluorescence as well as extrinsic fluorescence from fluorescein-labeled IgG. The objective of this paper is to present and compare two quantitation procedures for determining the amount of adsorbed protein at hydrophilic glass and quartz surfaces using total internal reflection fluorescence (TIRF) instrumentation. We also present a comparison of adsorption values for extrinsically labeled and intrinsically fluorescent (tryptophan) IgG to provide insight as to the possible effects of extrinsic labels upon protein adsorption.

The primary goal was to develop a simple quantitation procedure which produced realistic adsorption values. An extrinsic adsorption study was done using FITC-labeled IgG at 1.0 mg/ml on hydrophilic glass. FITC-labeled dextran was chosen as the calibration molecule since its molecular weight could be chosen to approximate the diffusion coefficient of IgG [6].

Intrinsic TIRF studies of IgG adsorption at 1.0 mg/ml on hydrophilic quartz were also done. Tryptophan was chosen as the intrinsically fluorescent calibration molecule in the UV. Since the diffusion coefficients of tryptophan and gamma-globulin do not match, only steady state fluorescent modeling was possible.

Both studies were steady state in nature, with concentration of bulk solution in the flow cell allowed to completely equilibrate before data were taken. The transport of protein to the interface was mathematically modeled by the convective-diffusion equations of fluid dynamics [6].

A thorough mathematical development of Maxwell's wave equations under conditions of total internal reflection has been shown [7,8] to lead to the following equation for the perpendicularly polarized (\perp) component of the transmitted (t) electric field, (\bar{E}_\perp^t):

$$\bar{E}_\perp^t = \hat{y} t_\perp E_{o\perp}^i \exp \left[-j \frac{2\pi x}{\lambda_2} \left(\frac{n_1}{n_2} \right) \sin \theta_1 - \frac{2\pi z}{\lambda_2} \left(\left(\frac{n_1}{n_2} \right)^2 \sin^2 \theta_1 - 1 \right)^{1/2} \right] \quad (1)$$

where $E_{o\perp}^i$ is the electric field amplitude at the interface in the less optically dense medium 2, n_1 and n_2 are the refractive indices of media 1 and 2, respectively, λ_2 is the wavelength in the second medium, θ_1 is the incident beam angle from the interfacial normal, and the directions x , y , and z are as shown in Fig. 1. Here we assume that the absorption characteristics of the rarer medium may be neglected and the real index of refraction may be used.

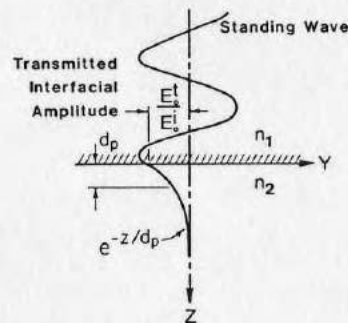


Fig. 1. A schematic of the surface wave in the y - z plane shows the standing wave pattern and exponential decay of the interfacial electric field amplitude into medium 2. See ref. 7 for further details.

Equation (1) represents the surface wave that propagates along the interface as demonstrated by Goos and Haenchen and discussed by Harrick [9]. The first exponential term accounts for the y -directional displacement between the incident and reflected beams at the interface. The penetration of this surface wave into the rarer medium in the z direction is accounted for by the second exponential term. Recognizing this form, we can set $1/d_p = 2\pi/\lambda_2((n_1/n_2)^2 \sin^2 \theta_1 - 1)^{1/2}$ and re-write eqn. (1) as

$$\bar{E}_\perp^t = \bar{E}_\perp^{t'} \exp \left[\frac{-z}{d_p} \right] \quad (2)$$

where

$$\bar{E}_\perp^{t'} = \hat{y} t_\perp E_{o\perp}^i \exp \left[-j \frac{2\pi x}{\lambda_2} \frac{n_1}{n_2} \sin \theta_1 \right]$$

The effective depth of penetration, d_p , of evanescent wave decay is defined for mathematical convenience to be the distance z required for the electric field amplitude to fall to e^{-1} of its original value (Fig. 1). It is now easy to see from eqn. (2) that for $e^{-z/d_p} = e^{-1}$ then,

$$z = d_p = \frac{\lambda_2}{2\pi \left(\left(\frac{n_1}{n_2} \right)^2 \sin^2 \theta_1 - 1 \right)^{1/2}} \quad (3a)$$

A more familiar form of the depth of penetration equation is obtained by noting that $\lambda_1 = \lambda_0/n_1$, where λ_0 is the free space wavelength of the incident beam. Equation (3a) now becomes [7]

$$d_p = \frac{\lambda_0}{2\pi n_1 \left[\sin^2 \theta_1 - \left(\frac{n_2}{n_1} \right)^2 \right]^{1/2}} \quad (3b)$$

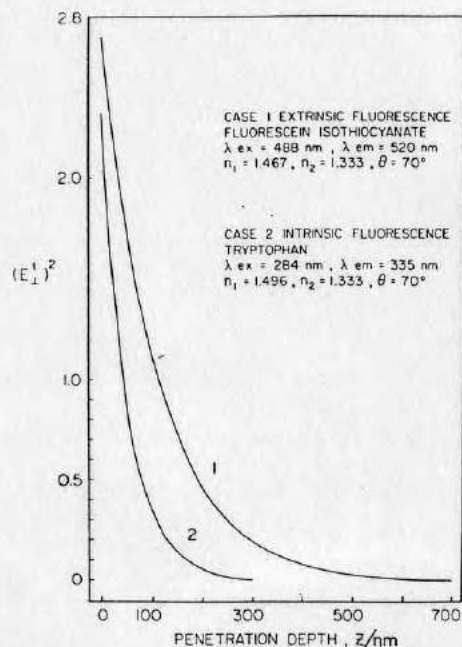


Fig. 2. Exponential intensity decay $(E_{\perp}^1)^2$ with distance z from the reflecting interface. Cases 1 and 2 demonstrate the difference between extrinsic and intrinsic TIRF.

where d_p is approximately 100 nm for intrinsic (280 nm) and 173 nm for extrinsic (488 nm) excitation light. It is important to recognize that the depth of penetration of the evanescent wave into the rarer medium is a function of λ_0 , θ_1 , n_1 , and n_2 only and manipulation of these four variables allows the experimentalist to control the depth of penetration to suit particular experimental needs.

In our configuration the perpendicular electric polarized electric field amplitude is simply the y component of the total amplitude. Thus, the electric field amplitude at the interface but in the rarer medium for our systems is given by Reichert et al. [7] and Harrick [9]:

$$E_{o\perp}^1 = \frac{2 \cos \theta_1}{\left[1 - \left(\frac{n_1}{n_2}\right)^2\right]^{1/2}} \quad (4)$$

From eqns. (2) and (3a) we find that the amplitude of the decaying evanescent excitation wave is

$$E_{\perp}^1 = E_{o\perp}^1 e^{-z/d_p} \quad (5)$$

at any distance z into the rarer medium (Fig. 1). This then allows one to plot the decaying intensity, proportional to $(E_{\perp}^1)^2$, as a function of the distance z from the interface; see Fig. 2 which shows the dependence of $(E_{\perp}^1)^2$ when λ_0 and n_1 vary.

MATERIALS AND METHODS

Two TIRF systems were used for this study. System 1 was based on glass fiber optics for extrinsic fluorescence. System 2 was based on a UV quartz optical system utilized for both the intrinsic and some extrinsic fluorescence studies. System 1 consists of three subunits: (1) the light source and associated optics; (2) the electronics needed to quantitate extrinsic fluorescence; and (3) the flow cell and associated plumbing. The three subunits all converge at the interface where light excites fluorescence which is then monitored by a photomultiplier tube. Figures 3 and 4 illustrate the system configuration.

The System 1 light source was a 2 W argon ion laser (Model 95, Lexel) operated at 488.0 nm in current control mode and coupled into an excitation optical fiber (QSF-200 UV, Quartz Products Corp.) by means of a 5X microscope objective (No. 57896, 0.10 NA, Aljae) mounted in a custom holder (Model LMI-B2, LHI-M, Newport) variable in x , y , z , θ , ϕ (Model FP-2, Newport). The output end of the excitation fiber was positioned at the focal point of a collimation lens (No. 94861, Edmund Scientific). The quasi-collimated excitation beam passed through an iris diaphragm emerged with a 4 mm diameter and an approximately divergence half angle of less than 5° . A polarizer (No. 30529, Edmund Scientific) passed light perpendicular to the plane formed by the incident and reflected beams. The lens, polarizer, and iris diaphragm were mounted inside a custom barrel holder mounted within a tripod-lens mounting device (Model AC-1, Newport) on the 20° wedge platform to yield an incidence angle θ_1 of 70° .

The excitation beam then entered a custom dove prism coupler (Precision Optical) cut from BK-7 low fluorescence glass (Schott Optical Glass Inc.; $n_{486.2 \text{ nm}} = 1.52238$). An index matching immersion oil (Type A, $n_D = 1.5150$, Cargille) optically interfaced the coupler to a $25 \times 75 \times 1$ mm microscope slide (Bev-1-edge microslides, Propper) where internal reflection occurred. The microscope slide also served as one face of the flow cell. The excitation light was reflected out of the prism and extinguished in a light trap.

Collection of interfacial fluorescence was achieved by means of two lenses, the first of which collected and collimated the fluorescent light emitted normal to the reflection interface (No. 94753, Edmund). The second lens (No. 94861, Edmund) focused the quasi-collimated output of the first lens into a collection optical fiber (QSF-600 UV, Quartz Products Corp.). Collection lenses were also mounted in a custom barrel holder in tripod mount. Collection fiber fluorescence passed through a glass interference filter (LP520, Carl Zeiss) which passed 85% of the fluorescence and blocked $> 99\%$ of the collected excitation scattered light. The emission filter was mounted over the aperture of a photomultiplier tube (PMT) (1P28P, Hamamatsu). The PMT was powered at 950 VDC (model 456, Ortec). The PMT signal was

SYSTEM OPTICS & ELECTRONICS

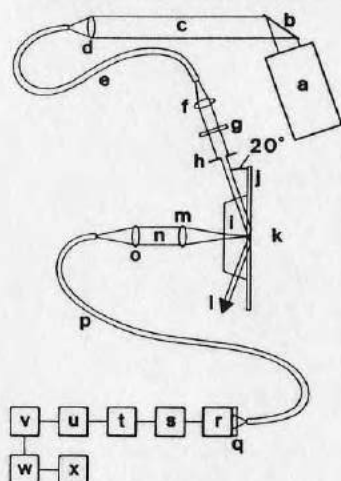


Fig. 3. Optical and electronic components of extrinsic TIRF System 1 illustrating excitation and collection optics and the flow cell. (a) Argon ion laser; (b) beam steering mirror; (c) laser excitation beam; (d) microscope focusing objective; (e) excitation optical fiber; (f) collimating lens (excitation); (g) polarizer; (h) iris diaphragm; (i) prism coupler; (j) microscope slide; (k) flow cell; (l) excitation beam; (m) collection lens; (n) collection beam (fluorescence); (o) focusing lens; (p) collection optical fiber; (q) emission filter; (r) photomultiplier tube; (s) preamplifier; (t) amplifier-discriminator; (u) photon counter; (v) sampling-control unit; (w) digital-to-analog converter; (x) strip-chart recorder.

sequentially input into a fast preamplifier (Model 9301, Ortec), an amplifier discriminator (Model 9302, Ortec), a photon counter (Model 9315, Ortec), Sampling/Control unit (Model 9320, Ortec), a D/A converter (Model 9325, Ortec), and finally recorded on a strip-chart recorder (Model 48, Pharmacia). See Fig. 3.

FLOW SYSTEM

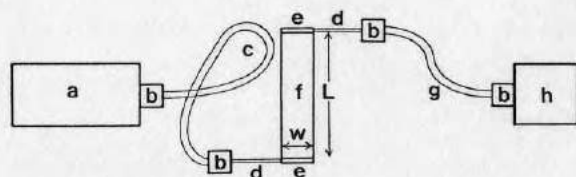


Fig. 4. TIRF flow system for System 1. (a) Syringe pump and syringe; (b) luer lock-stopcock combination; (c) input tubing; (d) hypodermic needle; (e) milled channel; (f) flow cell; (g) output tubing; (h) waste collection.

The flow configuration of System 1 is shown in Fig. 4. Solutions were introduced into the flow cell by means of a syringe pump (Model 341, Sage Instruments). Attachment of the 0.125 mm i.d. polyethylene tubing (PE200, Intramedic Clay Adams) to the syringe was facilitated by a metal luer-lock (Becton-Dickinson) and a three-way Teflon stopcock (K76P, Pharmaseal). Input tubing was connected to the flow cell by means of another luer lock-stopcock combination. The stopcock fed into a 20 gauge hypodermic needle (20 gauge—Luer Lok, Jelco) embedded in the brass flow cell base by means of a milled-out channel and Silastic® adhesive (Type A, Dow Corning).

The flow cell was a 12 mm brass base milled-out to accept a $25 \times 75 \times 1$ mm microscope slide and a 0.75 mm thick Silastic® rubber gasket. Milled channels at each end of the flow field provided fluid input and output ports. Flow field dimensions were $5 \times 0.75 \times 0.075$ cm as defined by a Silastic® gasket. The remaining flow cell wall was created by the glass microscope slide and clamping was provided by four screws which sandwiched the flow cell (gasket and microscope slide) between the brass base and an aluminum mounting plate. Fluid exited the flow cell through the output port and tubing which was identical to the input side.

The configuration of System 2 is described by Van Wagenen et al. [5], with the exception of a 150 W Xenon lamp light source (VIX 150 UV, ILC Technology). Three major differences between Systems 1 and 2 are: (1) the use of a Hg-Xe and Xe lamps with a monochromator as the light source instead of a laser; (2) the lack of optical fibers in System 2; and (3) the use of an emission monochromator in System 2 rather than an emission filter.

Conventional bulk solution fluorescence measurements were performed using a hybrid design based on System 2 with the bulk cell replacing the single reflection quartz prism. Excitation light was provided by a broadband 200 W Hg-Xe high pressure lamp (LH 150, Schoeffel Instrument). An excitation monochromator (H10-UV, Instruments SA) isolated the excitation wavelength necessary for fluorescence. A conventional 1 cm path length fluorometric quartz cuvette was mounted in a custom holder which was in turn mounted at the aperture of an emission monochromator (H10-UV, Instruments SA). Fluorescence emission was monitored normal to the excitation beam path at the center of the cuvette. Fluorescence emission was detected by a photomultiplier tube (R1332, Hamamatsu) and the Ortec photon counting equipment described. Fluorescence emission spectra were obtained on this instrument using a motor driven scan controller (Model 1020, ISA). Emission scans were run on each solution using 488 nm or 285 nm excitation light to determine the peak emission wavelength.

FITC-labeled dextrans used were commercially prepared and were dissolved in fresh phosphate buffered saline, pH 7.3 (2 mM KH_2PO_4 , 8 mM Na_2HPO_4 and 145 mM NaCl), solution (PBS) for each extrinsic experiment. FITC isomer I (F-7250, Sigma) was used to label gamma-globulin (82-041-2-1086, Fraction II, Miles). Labeling was carried out in pH 9.5 carbonate buffer for 75 min [10]. Separation of free and bound FITC was accomplished by gel filtration using Sephadex G-25 coarse beads (G-25, Pharmacia) hydrated with PBS solution in a 2.5 cm by 30 cm

long column. PBS solution was used to dilute all samples. Quantitation of the protein concentration and the degree of labeling (F/P) following gel filtration was possible using the nomogram provided by Wells et al. [11]. In System 2 the same gamma-globulin was used unlabeled and the calibration molecule was L-tryptophan (Matheson, Coleman, and Bell). Preparation of the hydrophilic quartz and glass surfaces has been outlined by Van Wagenen et al. [5].

TIRF data is a real time record of fluorescence intensity vs. time arising from the first several tens of nm of the interface. Any adsorbing protein solution introduced into the flow cell produces four distinct phases of fluorescence signal (Fig. 5) which are important in understanding both the flow and surface properties of the system. These phases are: (1) buffer background (Fig. 5a); (2) true bulk fluorescence excited by scattered light (Fig. 5b); (3) protein diffusion into the evanescent volume resulting in evanescent bulk signal (Fig. 5c); and (4) adsorption onto the surface (Fig. 5d). Since excitation light consists of two sources, evanescent light and scattered light, the scattered light contributes to the fluorescence signal both by exciting bulk solution fluorescence and by exciting fluorescence of evanescent zone and adsorbed surface molecules. As these phenomena overlap and are not simple to separate, some method must be available to extract the adsorption signal from the remaining signal components. Successful accomplishment of this task requires an in-depth understanding of each signal component and its origin within the system.

The buffer signal (Fig. 5a) is comprised of the dark count of the photomultiplier

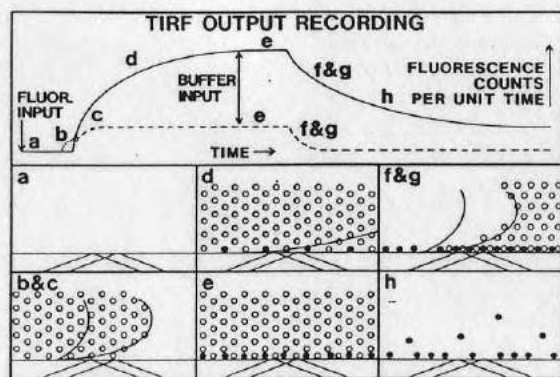


Fig. 5. Schematic TIRF strip-chart recording illustrating the various phases of signal generation within the flow cell. Each state of signal generation (a-h) is related to the nature of fluorescent material within the flow cell. Non-adsorbed bulk fluorescent molecules (○) adsorbed fluorescent molecules (●). Drawings (a)-(h) represent the adsorption case (solid line). The dashed line represents the non-adsorption case. (a) Buffer background; (b) scattering "shoulder" or scattered light excitation of bulk fluorescence; (c) diffusion into the evanescent volume through the diffusional boundary layer; (d) adsorption at the surface; (e) steady state fluorescence plateau; (f) scattered bulk fluorescence washout; (g) diffusion from the evanescent volume through the diffusional boundary layer; (h) desorption from the surface.

tube, excitation light which passes through the emission filter, and any fluorescent emission due to impurities within the glass components and/or the buffer solution.

Fluorescent solution entering the flow cell scattering volume displaces the majority of the bulk buffer but has not yet reached the evanescent region because of the diffusional boundary layer which must be traversed near the wall (Fig. 5b). During this period bulk fluorescence is excited by the scattered light only. Scattered light radiated from surface scattering sites such as defects or macromolecules may be a large or a small component of the total signal, depending upon the optical quality and cleanliness of the interface. Scattering sites within the prism, microscope-slide plate or coupling fluid may also contribute to this signal component. The bulk scattered component of the output is generally present to some degree and must be accounted for during quantitation of the adsorption signal.

Diffusion of fluorescent macromolecules into the evanescent volume creates the third component of the output signal (Fig. 5c). Both evanescent excitation and scattered excitation light within the evanescent volume are responsible for the visibility of the diffusional signal. One can model this signal, due to bulk scattering (Fig. 5b), and the time course of the signal due to evanescent excitation in the evanescent volume (Fig. 5c) by the use of the non-adsorbing modeling macromolecule dextran [6]. Thus, the relative fluorescence can be matched via appropriate calibration experiments.

The adsorption signal is the final portion of the output signal (Fig. 5d), and the quantitation of surface adsorption is the desired system output. All previous components must be separated from the adsorption signal for quantitation of the desired output and, since adsorption begins as soon as molecules have diffused to the surface, separation of these components is a difficult task.

Introduction of buffer back into the system following equilibration of the fluorescent solution will also result in four output phases (Fig. 5e-h). Immediately after beginning buffer flow, the fluorescent output signal remains at its equilibrium value while the bulk priming volume is being replaced with buffer solution (Fig. 5e). Next, the scattering component vanishes (Fig. 5f), although it is rarely separable from the diffusional component. This may be due to absorption of both excitation and emission light wavelengths by the fluorescent material remaining in the diffusional boundary layer.

Replacement of the fluorescent material in the diffusional boundary layer is the next component of the buffer flush output signal (Fig. 5g). This fluorescence diffusion from the surface differs from the fluorescence diffusion to the surface because the latter involves molecular diffusion from a semi-infinite bulk volume into a small diffusional boundary layer of buffer, while diffusion from the surface occurs from a thin diffusional boundary layer of fluorescent material into the semi-infinite buffer volume. Desorption and subsequent diffusion of the adsorbed protein comprises the last signal component (Fig. 5h).

RESULTS AND DISCUSSIONS

Correct modeling of TIRF data is dependent upon a number of assumptions: (1) light source and photon counting electronics do not drift; (2) bulk solution concentration is not depleted by adsorption and the concentration profile is constant to the surface; (3) temperature in the flow cell remains constant; (4) no photodegradation of adsorbed or bulk fluorescent molecules occurs; (5) non-linear scattering and absorption (inner-cell) effects are absent; and (6) quantum yield changes do not occur during adsorption.

The first five assumptions are valid. Constant flow at high bulk protein concentration replenishes bulk solution and maintains temperature at 25°C. Photodegradation is eliminated by chopping the light source. The thinness of the adsorbed protein layer eliminates the possibility of an inner-cell effect or of significant evanescent field attenuation, as shown experimentally and verified numerically [12].

Assumption (6) is, however, highly questionable. Lok [6] has reported that exposing adsorbed protein to PBS solution caused an increase in extrinsic fluorescence over that seen when unlabeled protein (in PBS) contacted the adsorbed protein. Our preliminary findings confirm this. In this present study, it was assumed that the fluorescence quantum yield, Q , of non-adsorbed molecules was equal to that of adsorbed molecules because it is impossible to verify or refute with our present equipment. However, it is plausible that conformational changes of the protein molecule upon adsorption and fluor-fluor interactions due to the close proximity of adsorbed molecules at the interface can be responsible for significant quantum yield changes. Physicochemical changes occurring as a result of protein adsorption probably tends to decrease the quantum yield of an extrinsic label such as fluorescein because its quantum yield is initially high, $Q \approx 0.85$ and molecular changes at the interface cannot induce fluorescence. However, the quantum yield of tryptophan may go up or down upon adsorption as Q for protein bound tryptophan is low.

Two separate methods for determining the amount of adsorbed protein using the interfacial fluorescence signal have been developed and evaluated. Both techniques require the six assumptions previously discussed.

The numerical quantitation approach is similar to that outlined by Van Wagenen et al. [5] and utilizes: (1) the fluorescence background signal N_B due to excited bulk protein solution within the evanescent volume, and (2) the evanescent signal intensity from adsorbed protein, N_A . See Fig. 6. $(E_{\perp}^1)^2$ vs. penetration depth, z , shown in Fig. 2, represents a measure of the total electric field intensity available for fluorescence excitation within the interfacial evanescent volume and may be arbitrarily expressed in field intensity units square (FIU²) as the exact integral of eqn. (5)

$$\int_0^{\infty} (E_{\perp}^1)^2 dz = \int_0^{\infty} (E_{o\perp}^1 e^{-z/d_p})^2 dz = (\text{FIU})_{\text{total}}^2 \quad (6)$$

The portion of the evanescent volume adjacent to the surface contains adsorbed protein molecules which will be excited by the evanescent electric field intensity. For

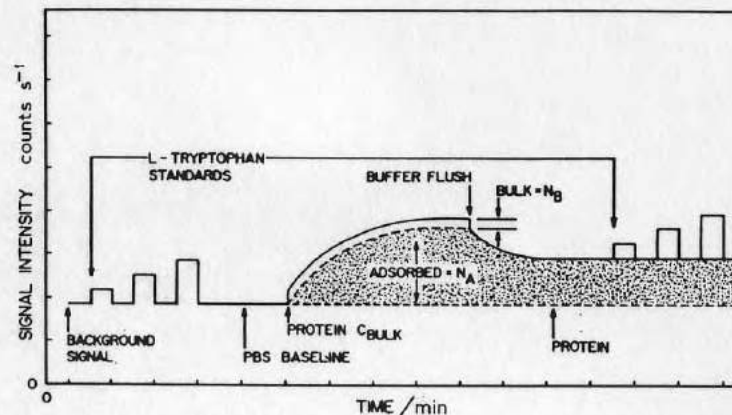


Fig. 6. An illustration of a typical TIRF data output. The tryptophan standards initiate each run and are used in the graphic calibration method. The darkened area represents adsorbed protein producing N_A counts per unit time. Evanescent zone fluorescence signal intensity is represented as N_B .

illustrative purposes, assume this thickness to be t . The integral of $(E_{\perp}^1)^2$ will yield the total evanescent field intensity available for fluorescent excitation of the film t thick as

$$\int_0^t (E_{o\perp}^1)^2 dz = \int_0^t (E_{o\perp}^1 e^{-z/d_p})^2 dz = (\text{FIU})_{\text{interfacial}}^2 \quad (7)$$

The bulk solution protein concentration (c_B) is excited by $(\text{FIU})_{\text{total}}^2$ producing N_B counts, while the adsorbed protein concentration (Γ_{vol}) is excited by $(\text{FIU})_{\text{interfacial}}^2$, producing N_A counts. The following equality must hold:

$$(\Gamma_{\text{vol}})(\text{FIU})_{\text{interfacial}}^2 Q_A / N_A = (c_B)(\text{FIU})_{\text{total}}^2 Q_B / N_B \quad (8)$$

where N_A and N_B are the counts due to adsorbed and evanescent bulk protein, and Q_A and Q_B are the quantum yield values for adsorbed and bulk protein, respectively. Assuming $Q_A = Q_B$ and solving for Γ_{vol} one gets:

$$\Gamma_{\text{vol}} = (N_A / N_B) c_B (\text{FIU})_{\text{total}}^2 / (\text{FIU})_{\text{interfacial}}^2 \quad (9)$$

Equation (9) results in an adsorbed protein volume concentration and is readily converted to a surface area concentration by multiplying Γ_{vol} by the assumed thickness of the protein film to yield Γ_{area} . The numerical method differs from that proposed by Van Wagenen et al. [5] in that an erroneous factor of 29 was included as part of the summation procedure due to an incorrect modeling assumption.

The graphical quantitation method assumes: (1) the calibration molecule does not adsorb to the surface, thus modeling the properties of the protein in the absence of macromolecular adsorption; and (2) extrapolation of linear quantitation plots of

QUANTITATION PROCEDURE

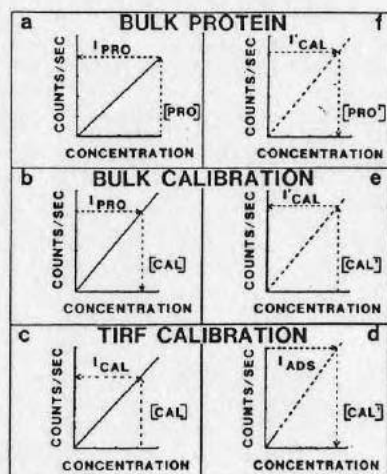


Fig. 7. Six quantitation plots illustrating the adsorption quantitation procedure. (a) Bulk protein fluorescence plot; (b) bulk calibration solution fluorescence plot; (c) TIRF calibration fluorescence plot; (d)–(f) extrapolated versions of (c), (b) and (a), respectively. See text.

TABLE 1

Summarized results of TIRF experiments

Fluorescent label type	Quantitation method ^a	Adsorbed protein concentration/ $\mu\text{g cm}^{-2}$ ^b	$\lambda_{\text{excitation}}$ / nm	$\lambda_{\text{emission}}$ / nm	Remarks ^c
Extrinsic	Graphical 1	0.024	488	> 520	1, 2, 3
Extrinsic	Graphical 2	0.032	488	520	4, 5, 6
Extrinsic	Numeric 2	0.034	488	520	4, 5, 6
Intrinsic	Graphical 1	0.015	285	335	5, 7, 8
Intrinsic	Graphical 2	0.008	285	335	5, 6, 8
Intrinsic	Graphical 3	0.017	285	335	4, 5, 6
Intrinsic	Numeric 1	0.039	285	335	5, 7, 8
Intrinsic	Numeric 2	0.015	285	335	5, 6, 8
Intrinsic	Numeric 3	0.018	285	335	4, 5, 6

^a Numbers refer to data sets.^b Adsorbed protein thickness assumed to be 10 nm.

^c (1) Laser-glass optics; (2) high pass emission filter used; therefore; $\lambda_{\text{emission}} > 520$ nm; (3) wall shear rate = 47.4 s^{-1} ; (4) Xe lamp-quartz optics; (5) emission monochromator used; (6) wall shear rate = 17.5 s^{-1} ; (7) non-flowing protein solution. Injection wall shear rate approximately 2000 s^{-1} ; (8) Hg-Xe lamp-quartz optics.

fluorescent vs. bulk concentration into the higher concentration domain for the purpose of graphical modeling. The extrapolation assumption allows graphical modeling of the fluorescent properties of the calibration solution and protein solution as though non-linear effects do not occur, which is reasonable in light of the extremely short "path length" of the TIRF experiment [12].

The graphical quantitation procedure is illustrated in Fig. 7. The bulk protein concentration to be used in the TIRF adsorption experiment is found to produce a bulk fluorescence intensity (Fig. 7a). Next a calibration solution concentration which models the protein's bulk fluorescence properties is measured (Fig. 7b). A TIRF calibration plot is generated by plotting the TIRF output against the calibration solution concentration. By using the calibration solution model concentration, a fluorescence intensity can be found on the TIRF calibration plot (Fig. 7c). This fluorescence intensity value represents that fluorescence which should be produced in the TIRF instrument by non-adsorbed protein since the dextran calibration molecule can be shown not to adsorb at the solution concentrations used. The protein adsorption experiment is then conducted and the previously determined non-adsorbed component is subtracted from the TIRF output signal. Any fluorescence intensity increase above the background level minus the non-adsorbed protein component should represent the fluorescence intensity due to adsorbed protein only.

The plots are now used in reverse order to generate a surface volume concentration from the adsorption component of the TIRF output signal. The TIRF fluorescence intensity signal associated with adsorbed protein must now be modeled by a calibration solution concentration of equal fluorescence intensity in the TIRF instrument. From the extended TIRF calibration plot this calibration solution model concentration can be found (Fig. 7d). The resulting calibration solution model concentration is then utilized to obtain a bulk fluorescence intensity from the extended bulk calibration plot (Fig. 7e). Finally, from the extended protein-bulk fluorescence plot, the protein surface volume concentration can be found from the bulk fluorescence model value (Fig. 7f). Thus, a series of graphical modeling steps utilizing three calibration plots makes it possible to derive the surface volume concentration of an adsorbed protein.

One now converts this surface volume concentration into a surface area concentration by assuming a thickness for the adsorbed film. The size of a gamma-globulin molecule is approximately $4.4 \times 4.4 \times 24$ nm in its native conformational state, and it has been shown to adsorb either with its long axis parallel or perpendicular to the surface [13–16].

The graphical quantitation scheme is primarily based upon the assumption that the calibration molecule does not adsorb on the surface. When dextran is used in the TIRF system, the fluorescence intensity rapidly returns to the background level after washing out the dextran solution, demonstrating the lack of irreversible adsorption of FITC-labeled dextrans. However, it is possible that a rapidly reversible adsorption process could be present. If such a mechanism were operating, it would be expected that the kinetics of the buffer washout phase of the TIRF signal would change with dextran concentration due to the difference between diffusion and

desorption kinetics. However, our TIRF calibration data using FITC-dextran shows no concentration-dependent kinetic variations; therefore, we conclude that either no reversible adsorption mechanism exists or, if it does exist, the adsorption kinetics are similar to or faster than the diffusional kinetics and have no adverse effect upon the assumption made here. In addition, the negatively charged nature of the FITC dextran molecule should reduce its attraction to a primarily negatively charged hydrophilic glass or quartz surface. Tryptophan operates similarly and can also be assumed to be non-adsorbing.

Table 1 summarizes the results of three intrinsic and two extrinsic TIRF experiments. Quantitation by graphical and numeric methods was done on four of the runs. The remaining extrinsic run could not be quantitated numerically.

CONCLUSIONS

The calculated surface density of FITC-IgG adsorbed on hydrophilic glass was found to be $0.024 \mu\text{g cm}^{-2}$, as determined with the graphical quantitation method. This is somewhat lower than values quoted in the literature which range from 0.1 to $0.2 \mu\text{g cm}^{-2}$ on various hydrophilic silicon dioxide and glass surfaces [15-17]. Two primary assumptions greatly influence the values tabulated in Table I and may contribute to an underestimation of adsorbed protein by the graphical quantitation technique.

First, the estimation of a 10 nm thickness of adsorbed gamma-globulin is questionable. A densely packed monolayer could range in thickness from 4 to 24 nm if no stretching or shrinking of the adsorbed molecules takes place. If multiple layers exist, a much greater thickness will be more accurate. Without additional information regarding the density, conformation, or adsorbed layer thickness any one of a range of values from perhaps 2 up to 50 nm or more would be appropriate. The 10 nm thickness was chosen because it is near the center of this range and thus has less chance of being highly erroneous. It is still plus or minus a factor of five from the extreme values; therefore, a half of an order of magnitude error may exist in our estimation.

Second, the assumption of equivalent bulk and adsorbed quantum yields is probably invalid. Since Q of extrinsically labeled adsorbed molecules probably decreases upon adsorption, more protein is actually adsorbed. Again, it is understandable that the numbers derived here for the extrinsic experiment would be low as a result of uncertainty generated by a major assumption.

Table I illustrates the difference between average adsorption values determined in intrinsic versus extrinsic TIRF, i.e., $0.018 \mu\text{g cm}^{-2}$ vs. $0.030 \mu\text{g cm}^{-2}$, respectively. Thus, it is important to note the differences between the two techniques which might lead to an explanation for the discrepancy between the values obtained.

The assumption of the thickness of the protein film affects the calculated amount of adsorbed protein differently in each technique. In the graphical approach, Γ varies directly with the thickness of the adsorbed layer. However, in the numerical approach the thickness assumption is used in the determination of

$(\text{FIU})_{\text{total}}^2/(\text{FIU})_{\text{interfacial}}^2$ and in the conversion of Γ_{vol} to Γ_{area} . Thus, if there is an error in this thickness assumption it is compounded twice in the numerical method leading to a larger error range.

A second difference is the use of UV light in the intrinsic TIRF approach. Since scattering is proportional to λ^{-4} , one has much more interfacial scattering in the UV which contributes to true bulk fluorescence rather than evanescent zone bulk fluorescence. The result is a value of N_B which is proportionally too large. By discriminating between N_B (bulk) and N_B (evanescent), the use of the latter would force Γ_{vol} to somewhat higher values (eqn. 9). Finally, the surfaces are slightly different, being hydrophilic soda-lime glass in the extrinsic and hydrophilic quartz in the intrinsic TIRF studies.

Further studies involving other methods of protein adsorption quantitation are being utilized to test the methods presented here. It is important that novel experiments be developed and carried out to probe the in situ thickness of adsorbed proteins and to determine the quantum yield of adsorbed proteins. Attempts at determining the fluorescent quantum yield of adsorbed macromolecules are being conducted by adsorbing radio labeled proteins onto surfaces and referencing the observed fluorescence against the interfacial radioactivity determined via sensitive in situ scintillation counting.

ACKNOWLEDGEMENTS

We acknowledge Jacques Baudot and Quartz Products Corporation for the optical fibers they provided. Funding was provided by a University of Utah Faculty Research Grant and by NIH Grant HL-18519. The assistance of D.E. Gregonis is gratefully appreciated.

REFERENCES

- 1 T. Hirschfeld, U.S. Patent 3604927, 1971.
- 2 M.N. Kronick and W.A. Little, *J. Immunol. Methods*, 8 (1975) 235.
- 3 R.W. Watkins and C.R. Robertson, *J. Biomed. Mater. Res.*, 11 (1977) 915.
- 4 N.J. Harriek and G.I. Loeb, *Anal. Chem.*, 45 (1973) 687.
- 5 R.A. Van Wagenen, S. Rockhold and J.D. Andrade, *Adv. Chem. Ser.*, 199 (1982) 351.
- 6 B.K. Lok, Ph.D. Thesis, Stanford University, September 1981.
- 7 M. Reichert, S. Rockhold, R.A. Van Wagenen and J.D. Andrade in J.D. Andrade (Ed.), *Interfacial Aspects of Biomedical Polymers*, Vol. 2, Plenum Press, New York, in press.
- 8 M. Born and E. Wolf, *Principles of Optics*, Macmillan, New York, 1964.
- 9 N.J. Harriek, *Internal Reflection Spectroscopy*, Interscience, New York, 1967.
- 10 M. Goldman, *Fluorescent Antibody Methods*, Academic Press, New York, 1968.
- 11 A.F. Wells, C.E. Miller and M.K. Nadel, *Appl. Microbiol.*, 14 (1966) 271.
- 12 S.A. Rockhold, M.Sc. Thesis, University of Utah, August 1982.
- 13 M.E. Soderquist and A.G. Walton, *J. Colloid Interface Sci.*, 75 (1980) 386.
- 14 B.W. Morrissey and C.C. Han, *J. Colloid Interface Sci.*, 65 (1978) 423.
- 15 B.W. Morrissey and C.A. Fenstermaker, *Trans. Am. Soc. Artif. Intern. Organs*, 22 (1976) 278.
- 16 B.W. Morrissey, *Ann. N.Y. Acad. Sci.*, 283 (1977) 50.
- 17 S.E. Bresler, V.M. Kolikov, N.V. Katushkina, R.B. Ponomareva, S.P. Zhdanov and E.V. Koromal'di, *Colloid J. USSR*, 36 (1974) 682.

The Effect of Tacticity on the Thermal Behavior of Various Poly(methacrylate esters)

G. A. RUSSELL, D. E. GREGONIS, A. A. DEVISSER, and J. D. ANDRADE

Department of Materials Science and Engineering, University of Utah,
Salt Lake City, Utah 84112

D. K. DALLING

Department of Chemistry, University of Utah, Salt Lake City, Utah 84112

Tacticity, the stereochemical placement of pendant side chains along the polymer backbone, has long been recognized as an important factor in determining bulk polymer physical properties. Such properties as crystallizability, solubility, melting point, glass transition temperature, etc. have been correlated with the tacticity of a given polymer (1,2,3,4). Introduction of Ziegler-Natta catalysts and other catalyst systems capable of controlling tacticity during synthesis has opened up new areas for commercial development based on systematic variation of molecular configuration. Little work has been reported, however, correlating chain tacticity to the surface and interfacial properties of polymers. Recent work (5) suggests that reorientation of the chains in the surface zone of the polymer can affect wettability of the surface. If that is indeed the case, the tacticity of the polymer chains may well have an influence on wettability, since the barriers to chain rotation are a function of tacticity. Also, the availability of hydrophilic and hydrophobic sites for interaction at the interface is influenced by the chain configuration and conformation. Consequently, it was felt that a study of the influence of tacticity on bulk physical and interfacial properties in the poly(hydroxyethyl methacrylate) (pHEMA)/water system might indicate some means of altering the interfacial properties of the polymer by control of its tacticity during synthesis. In this paper we report preliminary results of some experiments in which various methods of altering tacticity during synthesis have been examined and their effect correlated with changes in the thermal properties of the resulting polymers.

Synthesis of methyl and other alkyl methacrylates of high stereoregularity, either of high isotactic content or high syndiotactic content, is well-known (6). Unfortunately, the organometallic initiators used for production of stereoregular methacrylates are highly reactive to the hydroxyl functionality in the side chain of HEMA. Consequently, some means of blocking the hydroxyl group during polymerization was required. Methoxyethyl methacrylate (MEMA) was chosen as a model for a HEMA-like monomer

Literature Cited

1. Bovey, F. A. and Tiers, G. V. D., *J. Poly. Sci.*, **44**, (1960), 173.
2. Matsuzaki, K., Ishida, A., and Tateno, N., *J. Poly. Sci.*, Part C, (1967), **16**, 2111.
3. Goode, N. E., Owens, F. H., Fellman, R. P., Snyder, W. H. and Moore, J. E., *J. Poly. Sci.*, (1960), **46**, 317.
4. McCrum, N. G., Read, B. E. and Williams, G., "Anelastic and Dielectric Effects in Polymeric Solids", pp. 249-55, John Wiley & Sons, New York, 1967.
5. Holly, F. J. and Refojo, M. F., *J. Biomed. Materials Res.*, (1975) **9**, 315.
6. Lenz, R. W., "Organic Chemistry of Synthetic High Polymers", pp. 439-41, Interscience, New York, 1967.
7. DeVisser, A. C., Unpublished results.
8. Chlanda, F. P., and Donamura, L. G., *J. Appl. Poly. Sci.*, (1971), **15**, 1195.
9. Lando, J. B., Litt, M., Kumar, N. G., and Shimko, T. M., *J. Poly. Sci.*, (1974), Symposium Series No. 44, 203.
10. Bovey, F. A., *High Resolution NMR of Macromolecules*, pp. 80-82, Academic Press, New York, 1972.
11. Trekoval, J., Vlcek, P., and Lim, D., *Coll. Czech. Chem. Comm.*, (1971), **36**, 3032.

with its hydroxyl group protected, even though the methyl ether linkage is too stable to permit hydrolysis back to pHEMA. A second protected HEMA derivative used was trimethylsilylethyl methacrylate (TMSEMA), whose trimethylsilyl protection group can be cleaved readily, forming HEMA. This allows polymerization of TMSEMA using an anionic catalyst to produce a stereoregular pTMSEMA, followed by hydrolysis to stereoregular pHEMA. Polymers of HEMA, MEMA, and TMSEMA were synthesized by a variety of techniques, their tacticity was determined by ^{13}C -NMR spectrometry, and the variation in tacticity was correlated with changes in the DSC thermograms of each polymer.

Experimental

Monomer Preparation. All monomers used in this study except TMSEMA were obtained commercially. Methyl methacrylate (MMA) and methoxyethyl methacrylate (MEMA) were supplied by Aldrich Chemical Co.; 2-hydroxyethyl methacrylate (HEMA) was supplied by Hydro-Med Sciences. TMSEMA was synthesized in our laboratory by a procedure to be described elsewhere (7). The hydroquinone inhibitor was removed from the commercial monomers by extraction with aqueous NaOH. The monomer was then dried over MgSO_4 and distilled from LiAlH_4 and CuCl . The distilled product was then stored at 4°C over 5A molecular sieve until used. The structures of the monomers and abbreviations used are shown in Figure 1. The polymerization conditions used are summarized in Table I.

Anionic Polymerization. MMA, MEMA and TMSEMA were each polymerized anionically in dry toluene at -78°C using n-butyllithium as initiator. These conditions had been shown previously to produce pMMA and other alkyl methacrylates containing a high percentage of isotactic triads (8). In all cases the reaction was terminated by addition of methanol, and the polymer precipitated by a non-solvent, petroleum ether for pMMA and pMEMA, water for pTMSEMA. The crude products were then redissolved in benzene (pMMA and pMEMA) or some suitable solvent, and centrifuged to remove cross-linked polymer and precipitated LiOH. The resulting product was then dried overnight in vacuo at about 80°C .

Free Radical Polymerization. Free radical polymerization of HEMA and MEMA were accomplished by adding 1.8 mg/ml of azobis-methylisobutyrate (AMIB) to the degassed monomer. The monomer/initiator solution was injected into a split polypropylene mold and placed in an oven at 80°C for 20 hours. The resulting polymer sheet (3-4 mm thick) was then removed for further characterization. Since the pHEMA produced by bulk polymerization was too highly cross-linked to be redissolved for determination of its tacticity, the monomer, solvent (generally pyridine) and initiator were added directly to a 10 mm NMR tube along with 0.1-0.2 ml of p-dioxane as an internal standard and the resulting mixture was polymerized in situ by placing the tube into the oven at 80°C

for 20 hours. TMSEMA was polymerized in dry toluene using AMIB (TMSEMA/AMIB 1:100) as initiator. The polymer formed was precipitated in petroleum ether and dried overnight at 80°C in vacuo.

TABLE I.

MONOMERS USED AND POLYMERIZATION CONDITIONS*

Monomer	Initiator	Solvent	T ($^\circ\text{C}$)	Approx. Yield
Methylmethacrylate (MMA)	n-BuLi	Toluene	-78°	80%
	n-BuLi	THF	-78°	20%
2-Hydroxyethylmethacrylate (HEMA)	AMIB	None	60°	>95%
	AMIB w/UV	MeOH	-60°	25%
trimethylsilylethylmethacrylate (TMSEMA)	AMIB	Toluene	60°C	>90%
	n-BuLi	Toluene	-78°	20%
methoxyethylmethacrylate	n-BuLi	Toluene	-78°	30%
	AMIB	None	60°	>95%

*n-BuLi : n-butyl lithium

AMIB : azobismethylisobutyrate

UV : ultraviolet radiation

One low temperature polymerization of HEMA was carried out in an effort to produce a highly syndiotactic pHEMA. It was performed by dissolving HEMA and AMIB in methanol and exposing the solution to a 254 nm UV source for seven hours at -60°C . The resulting polymer was then precipitated in toluene and dried overnight at 60°C in vacuo prior to subsequent characterization.

Tacticity Determination. Samples for tacticity determination were prepared by placing 0.8-1.0 g of the dried polymer into a 10 mm NMR tube and adding 1.5-2 ml of an appropriate solvent along with 0.1-0.2 ml of p-dioxane as an internal reference. The tube was capped, and the solvent was allowed to swell or dissolve the polymer in the tube. CDCl_3 was used for pMMA and pMEMA, and pyridine for pHEMA and pTMSEMA. The proton decoupled 25,2 MHz ^{13}C spectrum was then obtained using a Varian XLFT-100 NMR spectrometer in the Fourier Transform mode. Spectra obtained at ambient temperature contained peaks which were too broad to resolve. Consequently, the samples were heated as high as practical without causing refluxing of solvent. Probe temperatures ranged from 50°C for MMA and pMEMA in CDCl_3 to 70°C for pHEMA and pTMSEMA in pyridine. At elevated temperatures sharp spectra were obtained in which each carbon absorption was resolved.

Assignment of the peaks in the pMMA spectra were based on published spectra (10). Assignment of peaks exhibiting shifts due to tacticity for pMEMA, pHEMA, etc. were made by analogy to pMMA.

Thermal Analysis. Differential Scanning Calorimetry (DSC) curves for each polymer were obtained over the range -50° to $+250^{\circ}\text{C}$ using a DuPont Model 990 Thermal Analysis System. Samples were weighed and placed in covered aluminum sample pans, then placed into the DSC. Each sample was annealed above its glass transition temperature for approximately 5 minutes, then cooled to the starting temperature for the thermogram. The sample was then heated at $10^{\circ}\text{C}/\text{minute}$ under a nitrogen atmosphere. An empty aluminum sample pan was used as a reference mass for each run.

Results and Discussion

pMMA. Figure 2 contrasts the ^{13}C -NMR spectra of two different samples of pMMA, one produced by free radical initiation and the other by low temperature anionic polymerization. Each peak in the spectrum is assigned to the various carbons in the polymer, and the chemical shift of each relative to the p-dioxane singlet at 0.0 ppm is shown. Of particular interest are the three peaks which correspond to the $\alpha\text{-CH}_3$ carbon atoms which are in the center of isotactic (i), heterotactic (h) and syndiotactic (s) triads, respectively. Similar splitting is observed for the carbonyl and quaternary carbon atoms, although the peaks are less well-resolved than the $\alpha\text{-CH}_3$ peaks. The area under each of the peaks is proportional to the number of carbon atoms in each type of triad in the sample. Hence, a ratio of the peak areas yields the relative amounts of each type of triad. Since the $\alpha\text{-CH}_3$ peaks are split relatively far apart, they have been used to calculate tacticities in this study. The free radical pMMA specimen contains 52% s / 41% h / 7% i triads, based on the relative peak areas. The anionic pMMA contains 10% s / 19% h / 71% i triads. The peak areas and chemical shifts of both pMMA samples, as well as those for the other polymers studied, are listed in Table II. Figure 3 contrasts the DSC thermograms of the same two polymers. Clearly, the predominantly isotactic anionic polymer exhibits different thermal behavior from that of the predominantly syndiotactic free radical polymer. The isotactic polymer shows a glass transition at 76°C , whereas the syndiotactic polymer has a T_g of 110°C . The thermal behavior of the specimens can thus be correlated with the tacticity observed by NMR.

pMEMA. The behavior of pMMA described above corresponds well with that reported previously (1). Consequently, it was expected that polymers of MEMA produced by free radical and anionic methods would show a corresponding difference in tacticity. The $\alpha\text{-CH}_3$ portions of the ^{13}C -NMR spectra of two different pMEMA samples are shown in Figure 4. The first specimen was produced using AMIB as a free radical initiator, while the second was

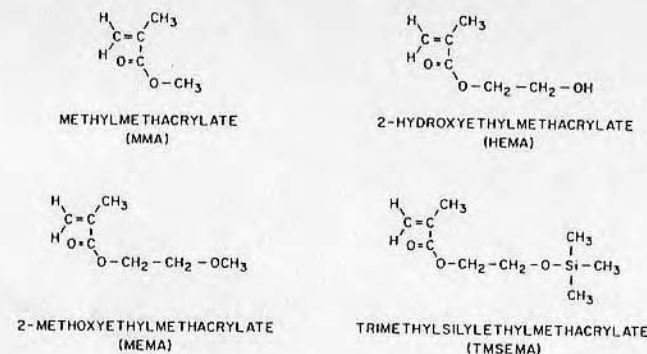


Figure 1. Monomer structure and nomenclature

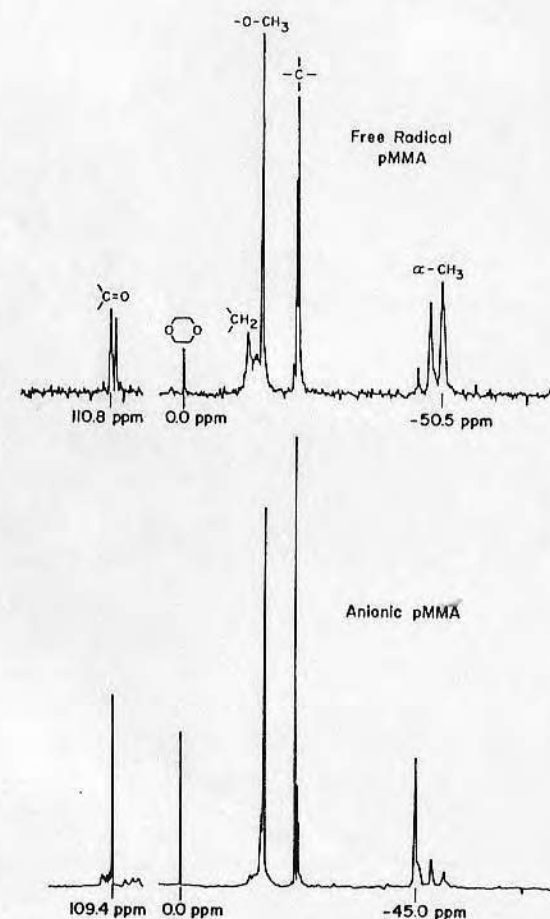


Figure 2. ^{13}C NMR spectra of poly(methyl methacrylate)

TABLE II.

Chemical Shifts for Various α -CH₃ and Carbonyl Triads*

Polymer	$\delta_{\alpha\text{-CH}_3}$ (ppm)**			Area: α -CH ₃			$\delta_{\text{C=O}}$ (ppm)			Solvent Temperature (°C)	
	i	h	s	i	h	s	i	h	s		
pMMA (anionic)	-45.0	-45.6	-45.7	57.1	15.6	8.1	109.4	109.7	110.4	CDCl ₃	Ambient
pMMA (commercial)	-45.8	-48.2	-50.5	14	88.5	109.3	--	109.9	110.8	CDCl ₃	Ambient
pHEMA (free radical)	--	-47.7	-49.5	--	54.0	107.9	--	110.1	110.7	Pyridine	70°
pHEMA (free radical- from pTMSEMA)	-44.6	-47.6	-49.4	6	57.3	89.1	--	110.2	110.8	Pyridine	70°
pHEMA (anionic- from pTMSEMA)	-44.5	-47.5	-49.4	137	164.4	165.0	110.0	110.2	110.8	Pyridine	70°
pHEMA (UV-low temp)	-45.9	-47.6	-49.3	21.1	31.2	189.6	--	--	110.8	Pyridine	70°
pMEMA (anionic)	--	-48.5	-50.2	--	28.8	55.8	--	109.4	110.3	CDCl ₃	50°
pMEMA (free radical)	--	-48.5	-50.3	--	77.5	95.0	--	109.5	110.2	CDCl ₃	50°
pMEMA (anionic from pMMA)				45.4	11.9	7.2				CDCl ₃	50°
				71%	18%	11%					

* i = isotactic; h = heterotactic; s = syndiotactic

** Chemical shifts expressed as ppm from dioxane singlet at 0 ppm

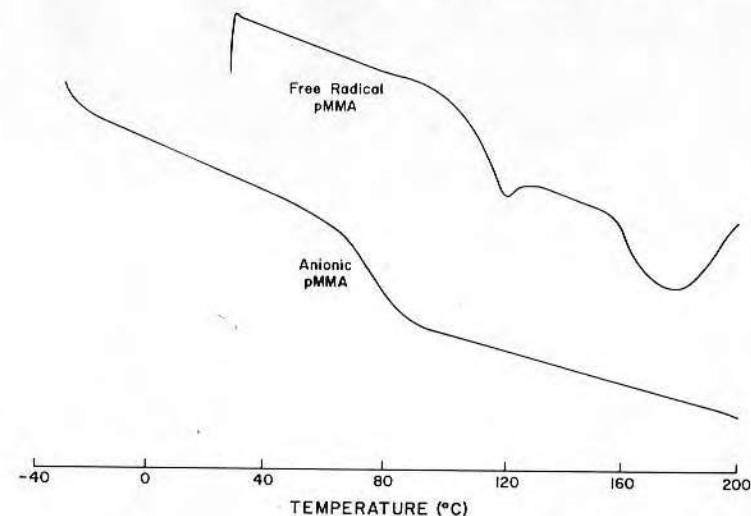
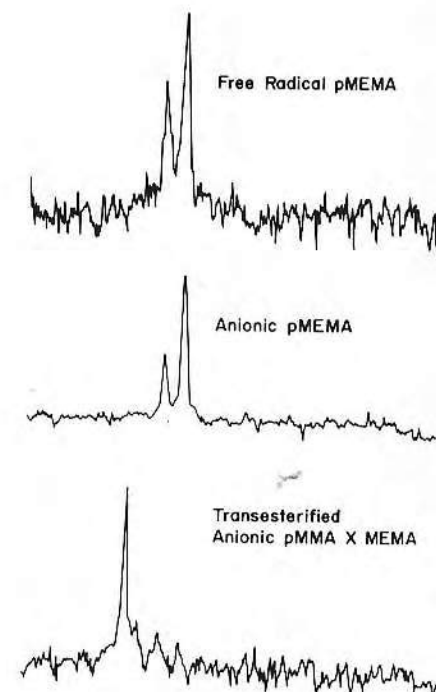


Figure 3. DSC thermograms of poly(methyl methacrylate)

Figure 4. α -CH₃ portions of ¹³C-NMR spectra of poly(methoxyethyl methacrylate)

produced anionically in toluene at -78°C . Both polymers contain a preponderance of syndiotactic and heterotactic triads, with few isotactic triads, as listed in Table II. In an effort to show that no irregularities in chemical shift had caused the anionic polymer to appear syndiotactic when it was actually isotactic, a sample of the isotactic pMMA described above was transesterified to pMEMA. The $\alpha\text{-CH}_3$ portion of its ^{13}C -NMR spectrum is shown in Figure 4c. Since it shows the same chemical shifts and relative peak areas as the parent pMMA, it must be concluded that the high syndiotactic content of the anionic pMEMA is not an artifact. Rather, it must be due to some interaction between the oxygen of the methoxy side chain and the anionic growth center which changes the local dielectric constant and alters the gegenion separation, thus favoring syndiotactic placement of incoming monomer units. Similar effects have been noted previously (11) with MEMA initiated by *t*-butyllithium at 20°C and -20°C . In that study, fewer than 10% isotactic triads were found at either temperature. The fact that both the anionic and free radical pMEMA specimens are predominantly syndiotactic is reflected in their DSC traces, shown in Figure 5. Both show an inflection at 25°C with no melting apparent, and begin to decompose above 250°C .

pHEMA. Figure 6 shows the $\alpha\text{-CH}_3$ portion of the ^{13}C -NMR spectra of pHEMA produced by four different methods. The relative tacticities calculated from the peak areas are given in Table II. The data show that pHEMA produced at elevated temperatures with AMIB (Figure 6(a)) contains predominantly syndiotactic (66%) and heterotactic triads (33%), with few isotactic triads (< 1%). Figure 6(b) shows similar results for a polymer formed from TMSEMA using AMIB as initiator, then subsequently hydrolyzed to pHEMA. Syndiotactic (58%) and heterotactic (38%) triads predominate over isotactic (4%) in this case as well. The third polymer, shown in Figure 6(c), was polymerized anionically at -78°C in toluene from TMSEMA, then hydrolyzed to pHEMA. Here we see a significant proportion of isotactic triads (30%) for the first time, with the remainder evenly divided between syndiotactic (35%) and heterotactic triads (35%). The fourth pHEMA, shown in Figure 6(d), was produced by UV initiation using AMIB at -78°C . As the figure shows, a highly syndiotactic polymer has been produced, having 78% syndiotactic triads, with 9% isotactic triads and 13% heterotactic triads. The DSC thermogram of each polymer is shown in Figure 7. The glass transition of the pTMSEMA produced anionically is 13° lower than that of free radical pTMSEMA, indicating that an increase in isotactic triads leads to a decrease in T_g , just as it did with pMMA. Further work will be required to increase the isotactic content of pHEMA polymers in order to fill out the full range from highly syndiotactic pHEMA to predominantly isotactic pHEMA. However, it now appears likely that systematic variation of tacticity will be achievable in the future and may provide a means of varying mechanical,

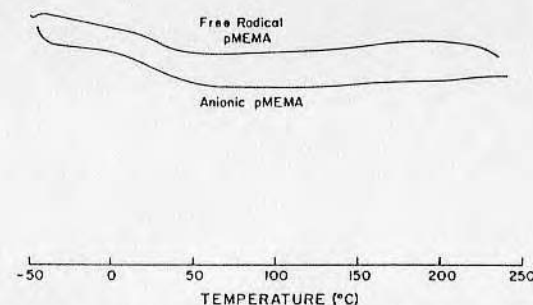


Figure 5. DSC thermograms of poly(methoxyethyl methacrylate)

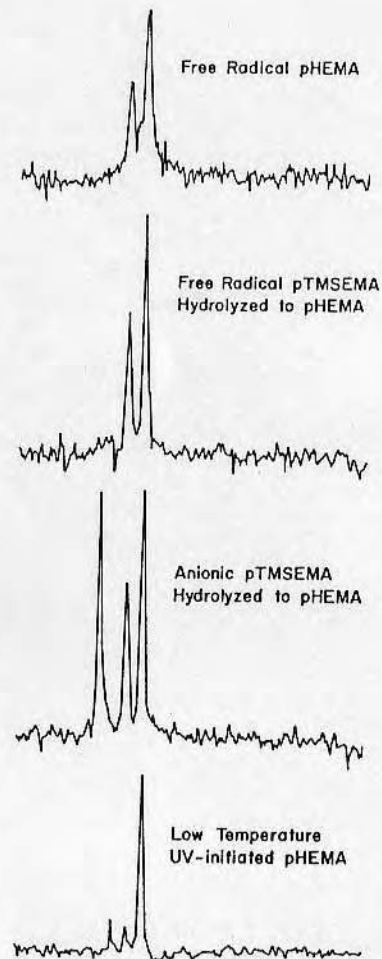


Figure 6. $\alpha\text{-CH}_3$ portions of ^{13}C -NMR spectra of poly(hydroxyethyl methacrylate)

thermal and surface properties in the pHEMA/water system for future studies.

Conclusions

Based on the data presented above, we conclude:

1. ^{13}C -NMR provides a method for directly determining the tacticity of methacrylate polymers. This eliminates the need for lengthy hydrolysis to poly(methacrylic acid) and re-esterification to pMMA.
2. Methacrylate-based polymers display significant changes in their DSC thermograms as a result of changes in tacticity.
3. Methacrylate esters with heteroatoms in their side chains interact with anionic initiators, reducing the isotactic content of the resulting polymers. Whether the effect of the heteroatoms can be reduced at temperatures below -78°C or by sterically hindering the heteroatom during polymerization remains to be seen.
4. Techniques are now available for producing soluble pHEMA polymers having a variety of tacticities. The effect of that tacticity variation on interfacial and bulk properties will be the subject of future work.

Acknowledgements:

This work was supported by NIH Grant HL 16921-01. We thank Hydro Med Sciences, Inc., New Brunswick, N. J. for generous donations of pure HEMA monomer.

Abstract

In this study a series of hydroxyethyl methacrylate (HEMA) and methoxyethyl methacrylate (MEMA) polymers of varying tacticities was produced. Both free radical and anionic initiators were used and their effect on tacticity determined. Tacticity of each polymer was measured by ratioing the ^{13}C -NMR peak areas for the $\alpha\text{-CH}_3$ carbon atoms in isotactic, syndiotactic, and heterotactic triads. Both the $\alpha\text{-CH}_3$ and carbonyl carbon peaks exhibit splitting due to tacticity, but the $\alpha\text{-CH}_3$ peak was better resolved. Chemical shifts for both atoms appear to be independent of the ester side chain for the polymers studied.

The thermal behavior of each polymer was observed over the range -50° to $+250^\circ\text{C}$ by differential scanning calorimetry (DSC). Differences in melting point and glass transition of the polymers were relatable to the tacticity measured by ^{13}C -NMR. This indicates potential for some control of the properties of pHEMA and other related hydrogels by control of tacticity during synthesis.

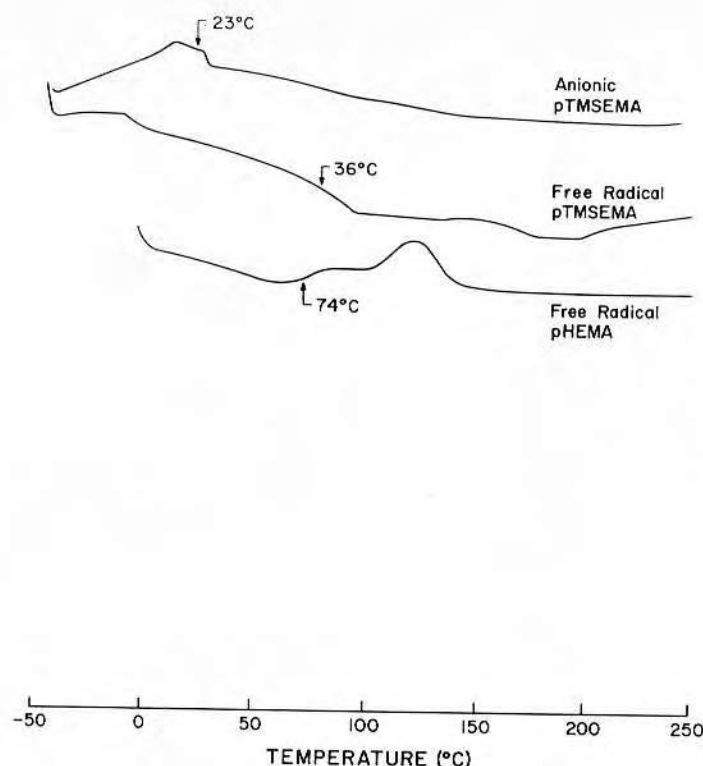


Figure 7. DSC thermograms of poly(hydroxyethyl methacrylate) and derivatives

Hydrogels for Medical and Related Applications

Joseph D. Andrade, EDITOR
University of Utah

A symposium sponsored
by the Division of
Polymer Chemistry, Inc.
at the 170th Meeting
of the American Chemical
Society, Chicago Ill.,
August 27-28, 1975

A C S S Y M P O S I U M S E R I E S

31

AMERICAN CHEMICAL SOCIETY
WASHINGTON, D. C. 1976

Thermal and Dynamic Mechanical Relaxation Behavior of Stereoregular Poly(2-Hydroxyethyl Methacrylate)

GEOFFREY A. RUSSELL,*† P. ANNE HILTNER,‡ DONALD E. GREGONIS, A. C. deVISSER,§ and JOSEPH D. ANDRADE, *Department of Materials Science and Engineering, University of Utah, Salt Lake City, Utah 84112.*

Synopsis

Thermal, dynamic mechanical, and dielectric relaxation techniques were used to determine the relaxation behavior of isotactic and syndiotactic poly(2-hydroxyethyl methacrylate) (pHEMA). Activation energies E_a were determined for the dielectric γ relaxation and compared with those of poly(2-methoxyethyl methacrylate) (pMEMA) to determine the influence of hydrogen bonding on side-chain relaxation processes. No difference in E_a was observed between syndiotactic pHEMA and atactic (predominantly syndiotactic) pMEMA. Isotactic pHEMA, however, had $E_a = 1$ kcal/mole higher than that of syndiotactic pHEMA. This was attributed to improved side-chain packing in the isotactic polymer.

INTRODUCTION

The synthesis, postpolymerization crosslinking, and swelling behavior of stereoregular poly(2-hydroxyethyl methacrylate) (pHEMA) have been described.¹ Here we present results obtained by differential scanning calorimetry (DSC), dynamic mechanical spectroscopy, and dielectric relaxation spectroscopy on noncrosslinked tactic pHEMA polymers.

The relaxation behavior of alkyl methacrylates has been the subject of extensive study.^{2,3} The mechanical relaxation behavior of crosslinked atactic pHEMA has been reviewed⁴; and one recent study compared the viscoelastic response of uncrosslinked, atactic pHEMA to that of crosslinked pHEMA.⁵ To date, however, no work has been reported on the relaxation behavior of pHEMA as a function of tacticity. In this article we report the effect of tacticity on the sub- T_g relaxation behavior of pHEMA and relate the differences in behavior to conformational differences between isotactic and syndiotactic pHEMA.

* Taken in part from Ph.D. dissertation of G. A. Russell.

† Present address: Kodak Research Laboratories, Eastman Kodak Company, Rochester, NY 14650.

‡ Department of Macromolecular Science, Case-Western Reserve University, Cleveland, OH 44106.

§ Department of Materials Science, Free University of Amsterdam, The Netherlands.

Thermal Transitions

The thermal behavior of each of the polymers studied was observed from 170 to 460 K using a DuPont Model 990 thermal analysis system fitted with a Borsma type DSC cell. Samples were prepared by depositing 10% (w/v) solutions of each polymer into aluminum DSC pans. The solutions were evaporated to dryness in air, then vacuum dried at 80°C and 0.1 Torr for 24 hr. The sample pans were then fitted with covers and hermetically sealed. Thermograms were obtained by cooling the DSC cell with the sample and reference pans in place to 150 K and then recording the differential thermal behavior on heating from 170 to 460 K. All samples were run in triplicate to ensure reproducibility.

Dynamic Mechanical Relaxation

The mechanical relaxation spectrum of each polymer was measured at approximately 1 Hz from 77 to 325 K using a freely oscillating torsion pendulum which was specially designed for the measurement of weak ($\Delta \geq 10^{-4}$) transitions at cryogenic temperatures (4 to 300 K).⁶ The specimens used were either in the form of hot-pressed strips 0.5 cm wide by 6.0 cm long by 0.02 cm thick, or in the form of glass braids which were impregnated with dilute polymer solution and then air and vacuum dried to form a composite specimen which could be suspended in the pendulum. After the sample was mounted in the grips, the pendulum was evacuated and cooled to 77 K by filling the outer Dewar with liquid nitrogen. When the entire system had reached equilibrium, the inner Dewar was filled with dry helium and the sample was slowly heated (0.5–1.0 K/min). Each 2 to 3 K the pendulum was displaced ca. 2° from the equilibrium, and the amplitudes of the resulting oscillations were recorded as a function of time using an oscillograph. The period and amplitude of the oscillations are related to the logarithmic decrement (Δ) and the relative rigidity ($1/P^2$) by

$$\Delta = (1/n) \ln (A_1/A_n)$$

and

$$1/P^2 = (\dot{n}/t_n)^2$$

where A_1 and A_n are the amplitudes of the first and n th oscillations, respectively, and t_n is the time required for n oscillations.

Dielectric Relaxation

The capacitance and conductance of each sample were measured from 77 to 325 K at 10 Hz, 100 Hz, 1 kHz, and 10 kHz using a General Radio Model 1621A capacitance measuring system of the modified Schering bridge type. Samples were prepared by casting solutions of each polymer onto 7.62 cm diameter by 7.8×10^{-3} cm thick brass electrodes using a stainless-steel casting knife. The coated electrodes were placed under inverted Petri dishes and allowed to air dry for 24 hr, then dried *in vacuo* at 0.1 Torr and 60°C for 8 hr. After vacuum drying they were stored over desiccant until use. Each coated electrode was placed in a parallel-plate capacitance cell⁷ which was jacketed for temperature control and

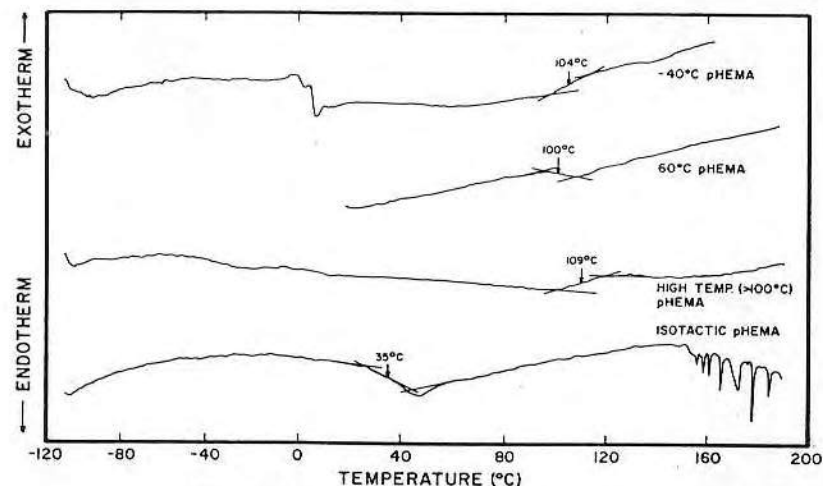


Fig. 1. DSC thermograms of pHEMA of varied tacticity.

purged with dry nitrogen. The cell was cooled slowly (ca. 1 K/min) from room temperature by passing liquid nitrogen through the cell jacket. Capacitance and conductance at each temperature and frequency were measured both during cooling to 77 K and upon subsequent warming from 77 to 325 K.

RESULTS AND DISCUSSION

Thermal Transitions

The DSC thermograms for a series of pHEMA polymers are shown in Figure 1. The glass-transition temperature reported for each sample is the midpoint of the glass-transition region. The glass transition generally extended over a range of 10–15 K for each sample. Polymerization conditions, tacticity, and T_g for each polymer are summarized in Table I. It can be seen from these data that all the azo-initiated samples have approximately the same T_g , 378 ± 5 K, independent of tacticity, which ranges from 0*i*/16*h*/84*s* triads to 0*i*/49*h*/51*s* triads. Only the anionically polymerized sample, with 80*i*/15*h*/5*s* triads, exhibits a significantly different T_g . For the isotactic sample $T_g = 308$ K, some 70 K lower than its syndiotactic counterpart. This large variation in T_g with tacticity

TABLE I
Glass Transition Temperatures of pHEMA Polymers as Determined by DSC

Polymer	Triad contents*			Polymerization temperature (K)	T_g (K)
	<i>i</i>	<i>h</i>	<i>s</i>		
pHEMA	0	17	83	233	377
	0	42	58	333	373
	0	49	51	423	382
	80	15	5	263	308

* Determined by integration of α -methyl carbon resonances in 25.2 MHz ¹³C-NMR spectra.

TABLE II
Samples Used for Dynamic Mechanical and Dielectric Relaxation Studies

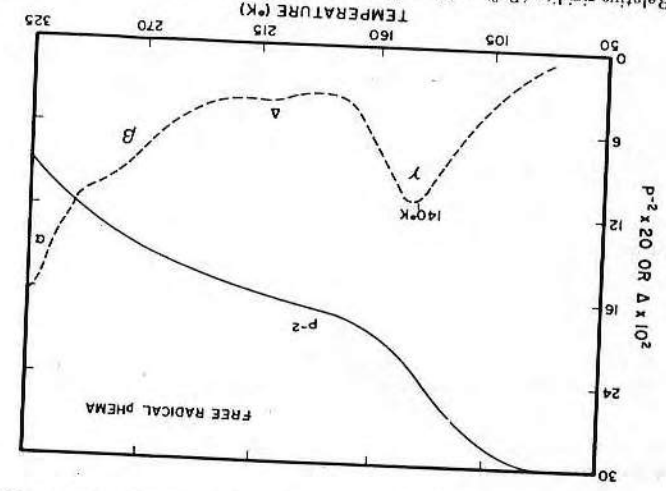
Sample	Initiator	Polymer	Polymerization temperature (K)	T _g (by DSC) (K)	Tactility	<i>s</i>
A	AMIB ^a	pHEMA	333	0	42%	58%
B	(<i>n</i> -Bu) ₂ LiCu ^b	pHEMA	263	80%	15%	5%
C	AMIB	pHEMA	233	0	16%	84%
D	AMIB	pHEMA	333	0	31%	69%
E	AMIB	pMEMA	423	0	42%	58%
^a Azobisisobutyronitrile (AIBN).						
^b <i>n</i> -Butyllithium/CuI (2:1) [(<i>n</i> -Bu) ₂ LiCu].						

parallels that observed in pMMA and other alkyl methacrylates, and indicates that the isotactic methacrylate chain is much more flexible than its syndiotactic counterpart.

Dynamic Mechanical Relaxation

Mechanical relaxation data have been plotted as logarithmic decrement (Δ) and dielectric studies are summarized in Table II. In Figure 2 the logarithmic decrement and relative rigidity are plotted versus temperature for a film specimen of sample A (0i/43h/57s). The peak of the α transition is not observable due to the onset of rubbery motion in the specimen. The β relaxation appears as a shoulder on the α peak, centered at 285 K, while the γ relaxation appears as a strong peak ($\Delta = 11 \times 10^{-2}$) with its maximum at 140 K. Similar behavior is observed for a braid specimen of sample C (0i/16h/84s), as shown in Figure 3. Here the use of the braid specimen allows us to observe the entire α relaxation,

Fig. 2. Relative rigidity (P^{-2}) and logarithmic decrement (Δ) vs. temperature for free-radical initiated pHEMA (sample A).



RELAXATION OF pHEMA

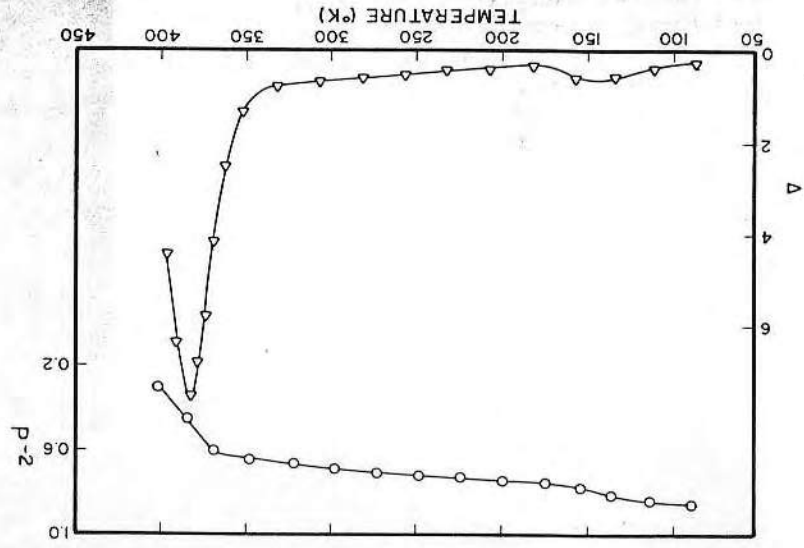
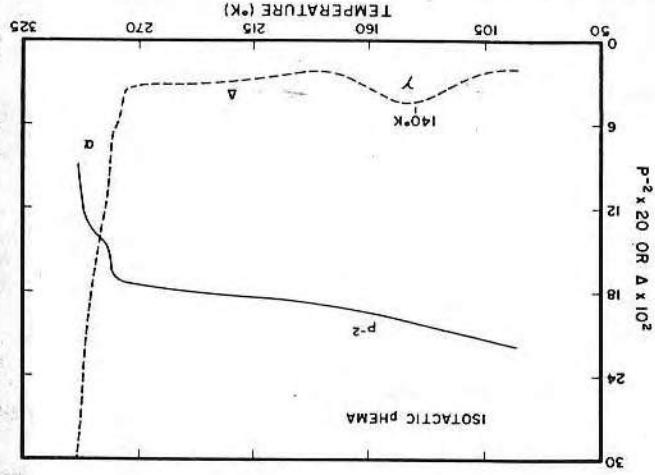


Fig. 3. Storage modulus and logarithmic decrement vs. temperature for syndiotactic pHEMA (sample C). (Every fourth data point shown.)

which has a peak at 380 K, but the weak β relaxation is not resolvable. The γ relaxation is clearly resolved, with its maximum at 145 K. Relaxation data for isotactic pHEMA (sample B) are shown in Figure 4. Again the peak in the α relaxation is not observable due to the onset of rubbery motion in the sample. No β relaxation is observed, and the onset of the α relaxation is much sharper than that of sample A, suggesting that the β relaxation has not been masked by

Fig. 4. Relative rigidity and logarithmic decrement vs. temperature for isotactic pHEMA (sample B).



still present, however, centered at 140 K.

Dielectric Relaxation

Isochronal plots of $\tan\delta$ versus temperature were made for each frequency, 10 Hz, 100 Hz, 1 kHz, and 10 kHz, in order to intercompare dielectric and dynamic mechanical relaxation data. For the samples used, dielectric breakdown at higher temperatures (>325 K) prevented the observation of the α -transition region, but the γ relaxation was clearly resolved in all cases. Plots were also made of $\log f_{\max}$ vs. $1/T_{\gamma}$, and the slope of the best least-squares line through the data was used to determine $\Delta H_{\gamma}^{\ddagger}$, the activation energy for the γ relaxation.

Dielectric relaxation data for sample C, syndiotactic pHEMA, are shown in Figure 5. A similar plot of $\tan\delta$ versus temperature for isotactic pHEMA, sample B, is shown in Figure 6. In order to assess the effect of hydrogen bonding on the γ -relaxation process, isochronal scans were made as a function of temperature for a sample of predominantly syndiotactic poly(2-methoxyethyl methacrylate) [pMEMA], sample D. pMEMA differs from pHEMA only in the terminus of the ester side-chain, where pMEMA has a methyl group, which is incapable of strong hydrogen bonding, while pHEMA has a hydroxyl group which is capable of strong hydrogen bonding. The plot of $\tan\delta$ versus temperature for sample D is shown in Figure 7. Plots of $\log f_{\max}$ vs. $1/T_{\gamma}$ for samples B, C, D, and E (a second pMEMA sample) are shown in Figure 8. The activation energies of the three predominantly syndiotactic samples B, D, and E ranged from 6.4 to 7.2 kcal/mole, while $\Delta H_{\gamma}^{\ddagger}$ for sample C, the only isotactic sample, was 8.2 kcal/mole.

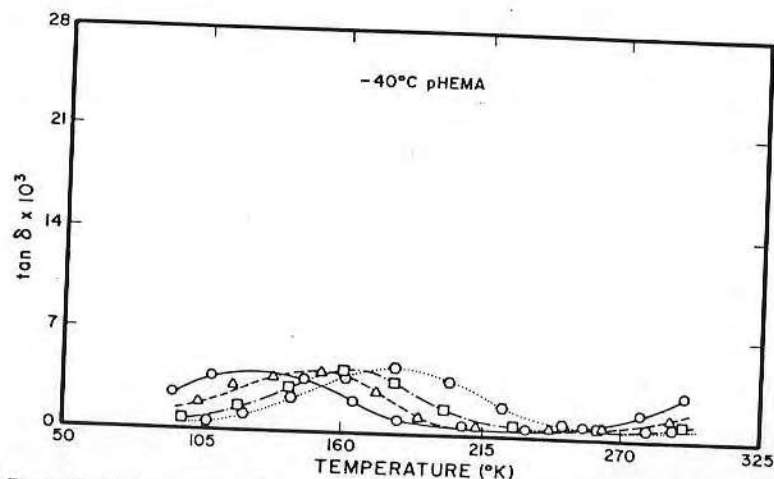


Fig. 5. $\tan\delta$ vs. temperature for syndiotactic pHEMA (sample C). (Every fourth data point shown.) (O—) 129 K, 10 Hz; (Δ ---) 149 K, 100 Hz; (\square ---) 164 K, 1 kHz; (O.....) 184 K, 10 kHz.

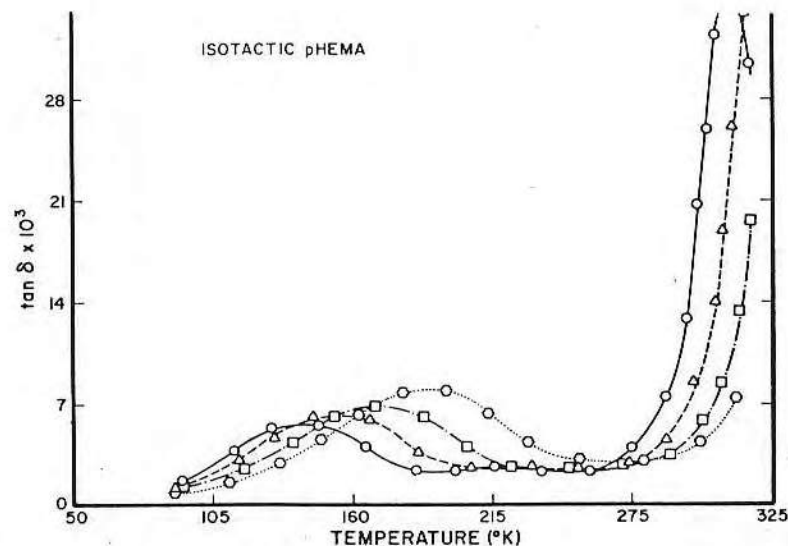


Fig. 6. $\tan\delta$ vs. temperature for isotactic pHEMA (sample B). (Every fourth data point shown.) (O—) 144 K, 10 Hz; (Δ ---) 155 K, 100 Hz; (\square ---) 169 K, 1 kHz; (O.....) 190 K, 10 kHz.

Conformational Differences in Stereoregular pHEMA

Differences in stereochemical configuration can lead to significant changes in rotational energy barriers and to differences in preferred chain conformation. In order to better understand the molecular motions which could give rise to the observed differences in relaxation behavior between syndiotactic and isotactic pHEMA, we have utilized CPK® space-filling molecular models. Transverse

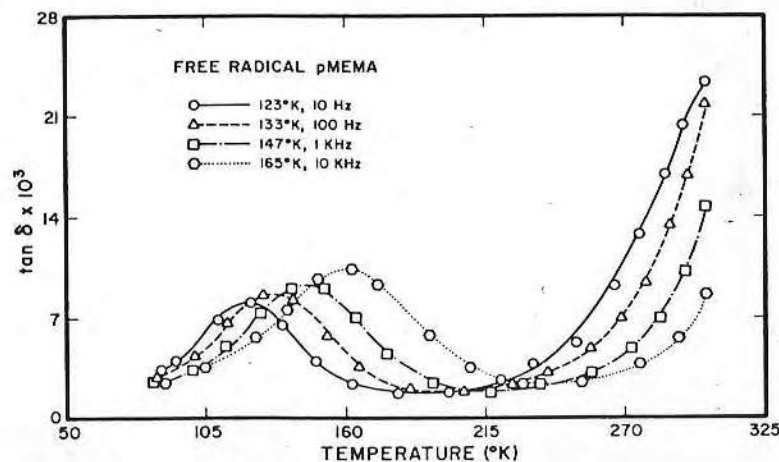


Fig. 7. $\tan\delta$ vs. temperature for atactic pMEMA (sample D). (Every fourth data point shown.) (O—) 123 K, 10 Hz; (Δ ---) 133 K, 100 Hz; (\square ---) 147 K, 1 kHz; (O.....) 165 K, 10 kHz.

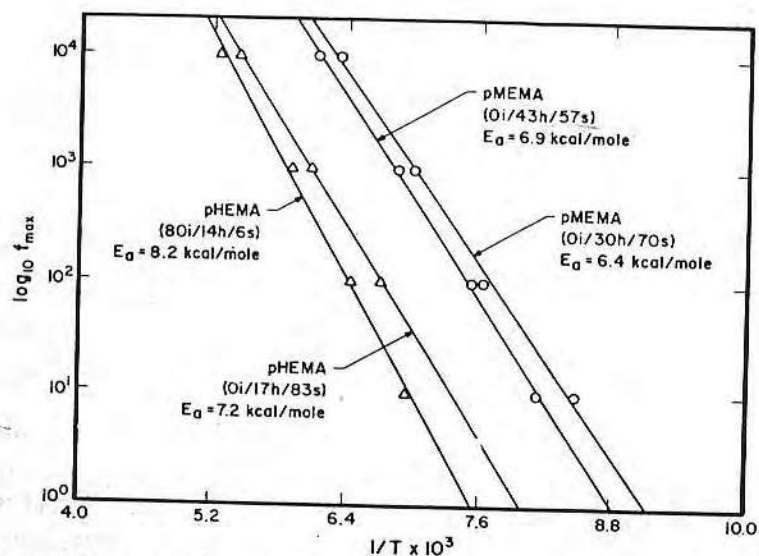


Fig. 8. $\log_{10} f_{\max}$ vs. T_g^{-1} showing variation in activation energy E_a with tacticity and monomer structure.

and axial views of the syndiotactic and isotactic chains are shown in Figures 9 and 10, respectively. In each case the chain segment contains eleven monomer

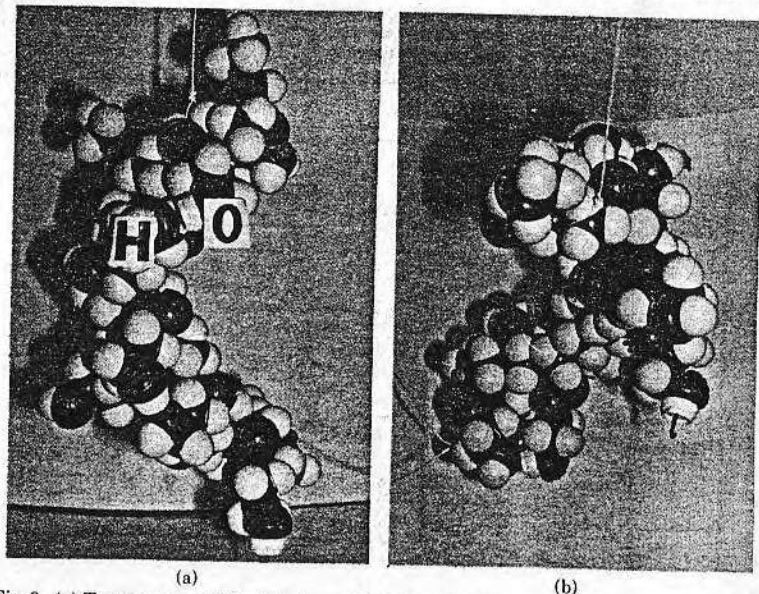


Fig. 9. (a) Transverse and (b) axial views of CPK® space-filling model of syndiotactic pHEMA chain in repeated $T_+T_-T_+G$ sequence. Note intramolecular hydrogen bond formed by nonadjacent residues.

those published for pMMA. The syndiotactic chain was assembled in an all-*trans* sequence in which the backbone bonds were alternately staggered $+15^\circ$ and -15° from 180° , the normal *trans* angle. As the chain was extended, it became necessary to intersperse *G* conformers periodically to minimize steric crowding. The resulting structure, shown in Figure 9, is composed of repeated $T_+T_-T_+G$ sequences. One consequence of introducing *G* conformers is the formation of an intrachain hydrogen bond between the two monomer units on either side of the *G* linkage. Such intrachain hydrogen bonding should provide additional stabilization of *G* conformations in syndiotactic pHEMA relative to pMMA and should increase the number of *G* conformers present.

The isotactic pHEMA chain was assembled in an all-*gauche* conformation, which gave rise to the helical structure pictured in Figure 10. The all-*gauche* structure was chosen because the CPK® models fit into it readily, with little crowding of adjacent side-chains, whereas steric hindrance did not permit assembly of the models into predominantly *trans* structures. Recent calculations of conformational energies for polyisobutylene¹⁰ and for isotactic polystyrene¹¹ which used potential functions which explicitly included methyl and methylene hydrogen interactions confirm the stability of *gauche* conformations in isotactic chains with bulky substituents. Therefore, the all-*gauche* conformation for isotactic pHEMA is not unreasonable.

Several differences between the isotactic and syndiotactic chains should be noted. First, the isotactic chain has no intrachain hydrogen bonds linking its ester side-chains. On the other hand, every *TGT* sequence in the syndiotactic chain brings two pendant hydroxyl groups into close proximity where they can form a hydrogen bond which stabilizes the local chain conformation. Second, the carbonyl groups of the isotactic chain are severely hindered by the α -methyl group of the next monomer unit in the chain and by the carbonyl carbon of the preceding monomer unit. In contrast, the carbonyl group in the syndiotactic chain is less severely crowded by its two nearest neighbors, the α -methyl groups of the preceding and succeeding monomer units. Third, the ester side chains of the isotactic pHEMA are packed together rather efficiently along the outside of the helix, while in the syndiotactic chain only those ester side-chains on either side of a *TGT* sequence exhibit intrachain interactions. The other ester side chains do not pack together because their nearest neighbors are methyl groups, which do not extend out from the backbone. Finally, we note that the polar groups in the isotactic chain are all displaced outward from the helical backbone, giving rise to a helix which has a hydrophobic inner surface and a hydrophilic outer surface. This is not the case for syndiotactic pHEMA where polar and apolar groups are interspersed along the helix. This may account, in part, for the differences observed in the swelling behavior of isotactic and syndiotactic pHEMA.¹

CONCLUSIONS

Differential Scanning Calorimetry

The glass transition in pHEMA is readily observable by DSC. Predominantly syndiotactic specimens had a T_g of 378 ± 5 K which was insensitive to small changes in tacticity. On the other hand, isotactic pHEMA had a T_g of 308 K,

those published for pMMA. The syndiotactic chain was assembled in an all-*trans* sequence in which the backbone bonds were alternately staggered $+15^\circ$ and -15° from 180° , the normal *trans* angle. As the chain was extended, it became necessary to intersperse *G* conformers periodically to minimize steric crowding. The resulting structure, shown in Figure 9, is composed of repeated $T_+T_-T_+G$ sequences. One consequence of introducing *G* conformers is the formation of an intrachain hydrogen bond between the two monomer units on either side of the *G* linkage. Such intrachain hydrogen bonding should provide additional stabilization of *G* conformations in syndiotactic pHEMA relative to pMMA and should increase the number of *G* conformers present.

The isotactic pHEMA chain was assembled in an all-*gauche* conformation, which gave rise to the helical structure pictured in Figure 10. The all-*gauche* structure was chosen because the CPK[®] models fit into it readily, with little crowding of adjacent side-chains, whereas steric hindrance did not permit assembly of the models into predominantly *trans* structures. Recent calculations of conformational energies for polyisobutylene¹⁰ and for isotactic polystyrene¹¹ which used potential functions which explicitly included methyl and methylene hydrogen interactions confirm the stability of *gauche* conformations in isotactic chains with bulky substituents. Therefore, the all-*gauche* conformation for isotactic pHEMA is not unreasonable.

Several differences between the isotactic and syndiotactic chains should be noted. First, the isotactic chain has no intrachain hydrogen bonds linking its ester side-chains. On the other hand, every *TGT* sequence in the syndiotactic chain brings two pendant hydroxyl groups into close proximity where they can form a hydrogen bond which stabilizes the local chain conformation. Second, the carbonyl groups of the isotactic chain are severely hindered by the α -methyl group of the next monomer unit in the chain and by the carbonyl carbon of the preceding monomer unit. In contrast, the carbonyl group in the syndiotactic chain is less severely crowded by its two nearest neighbors, the α -methyl groups of the preceding and succeeding monomer units. Third, the ester side chains of the isotactic pHEMA are packed together rather efficiently along the outside of the helix, while in the syndiotactic chain only those ester side-chains on either side of a *TGT* sequence exhibit intrachain interactions. The other ester side chains do not pack together because their nearest neighbors are methyl groups, which do not extend out from the backbone. Finally, we note that the polar groups in the isotactic chain are all displaced outward from the helical backbone, giving rise to a helix which has a hydrophobic inner surface and a hydrophilic outer surface. This is not the case for syndiotactic pHEMA where polar and apolar groups are interspersed along the helix. This may account, in part, for the differences observed in the swelling behavior of isotactic and syndiotactic pHEMA.¹

CONCLUSIONS

Differential Scanning Calorimetry

The glass transition in pHEMA is readily observable by DSC. Predominantly syndiotactic specimens had a T_g of 378 ± 5 K which was insensitive to small changes in tacticity. On the other hand, isotactic pHEMA had a T_g of 308 K,

some 70 K lower than its syndiotactic counterpart. The DSC thermogram of isotactic pHEMA also exhibited a series of sharp endothermic peaks in the range 423–453 K, which may have been due to the melting of small crystallites or ordered domains. Syndiotactic samples prepared in the same manner did not exhibit similar peaks.

Relaxation Behavior of Stereoregular pHEMA

Relaxation data for syndiotactic and isotactic pHEMA are summarized in Table III. From the dynamic mechanical data we can see that syndiotactic pHEMA exhibits an α relaxation at 380 K (ca. 1 Hz), a β relaxation, which appears as a shoulder on the α -relaxation (ca. 1 Hz), and a γ relaxation at 145 K (ca. 1 Hz). Isotactic pHEMA exhibits only an α relaxation at 315 K (ca. 1 Hz) and a γ relaxation at 140 K (ca. 1 Hz) which is approximately half as intense as that of syndiotactic pHEMA. The β relaxation has been completely suppressed in isotactic pHEMA. Gillham¹² attributes the suppression of the β relaxation in isotactic pMMA to interchain steric hindrance arising from the formation of helical domains within the specimen. Consideration of the molecular models of isotactic pHEMA leads to a second, equally plausible, explanation for the hindrance of carbonyl group rotation and the absence of a β -relaxation peak in isotactic methacrylates. The severe crowding of a given carbonyl group by its nearest neighbors, which was noted in the preceding section, would make rotation

O

||

about the $C^\alpha-C-O$ bond virtually impossible below T_g in isotactic pHEMA. Since carbonyl rotation is responsible for the β relaxation observed in syndiotactic methacrylates, the intrachain steric hindrance can account for suppression of the β relaxation without resort to assumptions of interchain steric hindrance and domain formation.

The increased barriers to carbonyl rotation in isotactic methacrylates may also explain the lowering of T_g observed in isotactic methacrylates relative to their syndiotactic counterparts. Since carbonyl group rotation cannot occur without some correlated conformational changes in the backbone bonds, no β relaxation is observed in isotactic pHEMA. Carbonyl group rotation may, however, give rise to additional local minima in conformational energy which are separated from the overall minimum by relatively low energy barriers. This has been observed in the conformational energy functions for polyisobutylene,¹⁰ and has been offered as an explanation for the anomalously low T_g of that polymer. If similar local minima exist in isotactic methacrylates as a result of

TABLE III
Relaxation Temperatures Observed Mechanically and Dielectrically

Sample	Polymer	Dynamic mechanical (ca. 1 Hz)			Dielectric	
		T_α (K)	T_β (K)	T_γ (K)	T_γ (K)	ΔE_γ + (kcal/mole)
A	pHEMA	not observable	285	140
B	pHEMA	315	not present	145	144	8.2
C	pHEMA	380	285	145	129	7.2
D	pMMA	not observable	280	120	123	6.4
E	pMMA	315	280	125	118	6.0

correlated backbone motions initiated by carbonyl group rotation, this would account for the low T_g of isotactic methacrylates. Since carbonyl rotation can occur in syndiotactic methacrylates without changes in backbone conformation, no local minima in conformational energy would be introduced and no lowering of T_g would be observed.

Because of dc conductivity breakthrough at higher temperatures, only the γ relaxation could be observed dielectrically. It occurred at 140 ± 5 K (10 Hz) for both isotactic and syndiotactic pHEMA, and at 120 ± 5 K for syndiotactic pMEMA. The activation energy ΔH_γ^\ddagger for the γ relaxation was not significantly affected by the presence of hydrogen bonding. It was influenced by tacticity, however, being 8.2 kcal/mole for isotactic pHEMA versus 6.8 ± 0.4 kcal/mole for predominantly syndiotactic pHEMA and pMEMA. The difference in ΔH_γ^\ddagger observed is probably due to the more efficient packing of the ester side-chains along the isotactic helix, discussed previously. It should also be noted that the conformational rearrangements responsible for the γ relaxation observed mechanically must differ somewhat from those responsible for the dielectric γ dispersion. When we plot 1 Hz mechanical data and 10 Hz dielectric data for isotactic pHEMA, as shown in Figure 11, we can see that the mechanical loss peak occurs at a higher temperature than the dielectric loss peak. Extrapolation of the dielectric data to 1 Hz yields a predicted T_γ of 133 K, whereas a T_γ of 145 K is observed mechanically. No direct comparisons can be made, therefore, between data obtained mechanically and dielectrically. However, both mechanical and dielectric data can be rationalized on the basis of models of syndiotactic and isotactic chains in Figures 9 and 10. More important, no assumption of amorphous ordering is required to explain the differences observed between isotactic and syndiotactic methacrylates.

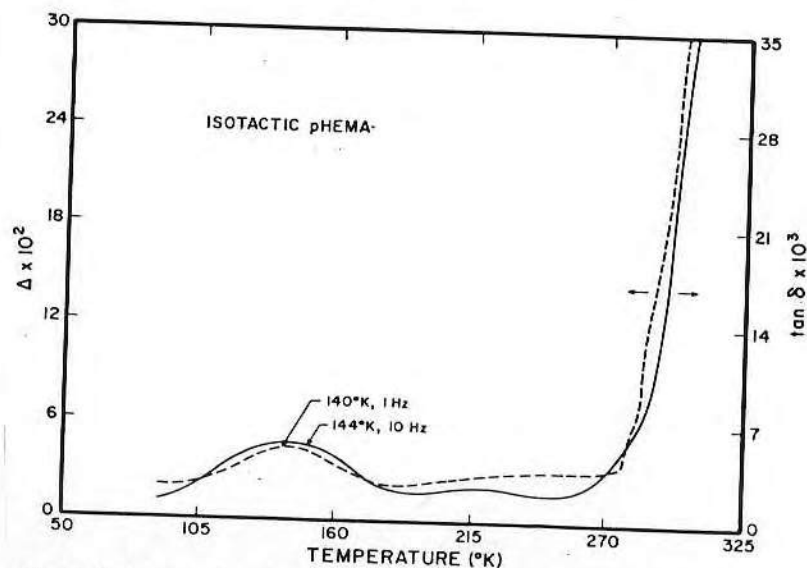


Fig. 11. Comparison of γ relaxation observed dielectrically and mechanically for isotactic pHEMA.

SUMMARY

The relaxation behavior of stereoregular poly(2-hydroxyethyl methacrylate) has been studied by dynamic mechanical and dielectric spectroscopy. Differences in relaxation have been observed which are correlated with proposed conformational differences between isotactic and syndiotactic methacrylate chains.

Portions of this work were supported by NIH Grant No. HL 16921-02. A gift of purified HEMA monomer from Hydron Laboratories, Inc., New Brunswick, NJ, is greatly appreciated. We thank Professor R. H. Boyd for the use of the dielectric relaxation apparatus, as well as for many helpful discussions. Discussions with Dr. Lutz Beck were also very stimulating and helpful.

References

1. D. E. Gregonis, G. A. Russell, A. C. deVisser, and J. D. Andrade, *Polymer*, **19**, 1279 (1978).
2. N. G. McCrum, B. E. Read, and C. Williams, *Anelastic and Dielectric Effects in Polymeric Solids*, Wiley, London, 1967.
3. I. M. Ward, *Mechanical Properties of Solid Polymers*, Wiley-Interscience, London, 1971.
4. J. Janáček, *J. Macromol. Sci. Rev. Macromol. Chem.*, **C9**, 1 (1973).
5. L. Nicolais, D. Acierno, M. Stol, and J. Janáček, *J. Polym. Sci. Polym. Phys. Ed.*, **12**, 2579 (1974).
6. C. D. Armeniades, I. Kuriyama, J. M. Roe, and E. Baer, *J. Macromol. Sci. Phys.*, **B1**, 777 (1967).
7. C. R. Ashcraft, doctoral dissertation, University of Utah, 1975.
8. P. R. Sundararajan and P. J. Flory, *J. Am. Chem. Soc.*, **96**, 5025 (1974).
9. D. Y. Yoon and P. J. Flory, *J. Polym. Sci. Polym. Phys. Ed.*, **14**, 1425 (1976).
10. R. H. Boyd and S. M. Breitling, *Macromolecules*, **5**, 1 (1972).
11. Lutz Beck, doctoral dissertation, University of Ulm (M.N.H.), Ulm, Federal German Republic, 1976.
12. J. K. Gillham, *Am. Inst. Chem. Eng. J.*, **20**, 1066 (1974).

Received June 7, 1979

Accepted December 18, 1979

poly(2-methoxyethyl methacrylate) (pMEMA) to determine the influence of hydrogen bonding on side-chain relaxation processes. No difference in E_a was observed between syndiotactic pHEMA and atactic (predominantly syndiotactic) pMEMA. Isotactic pHEMA, however, had $E_a = 1$ kcal/mole higher than that of syndiotactic pHEMA. This was attributed to improved side-chain packing in the isotactic polymer.

INTRODUCTION

The synthesis, postpolymerization crosslinking, and swelling behavior of stereoregular poly(2-hydroxyethyl methacrylate) (pHEMA) have been described.¹ Here we present results obtained by differential scanning calorimetry (DSC), dynamic mechanical spectroscopy, and dielectric relaxation spectroscopy on noncrosslinked tactic pHEMA polymers.

The relaxation behavior of alkyl methacrylates has been the subject of extensive study.^{2,3} The mechanical relaxation behavior of crosslinked atactic pHEMA has been reviewed⁴; and one recent study compared the viscoelastic response of uncrosslinked, atactic pHEMA to that of crosslinked pHEMA.⁵ To date, however, no work has been reported on the relaxation behavior of pHEMA as a function of tacticity. In this article we report the effect of tacticity on the sub- T_g relaxation behavior of pHEMA and relate the differences in behavior to conformational differences between isotactic and syndiotactic pHEMA.

* Taken in part from Ph.D. dissertation of G. A. Russell.

† Present address: Kodak Research Laboratories, Eastman Kodak Company, Rochester, NY 14650.

‡ Department of Macromolecular Science, Case-Western Reserve University, Cleveland, OH 44106.

§ Department of Materials Science, Free University of Amsterdam, The Netherlands.

Journal of Polymer Science: Polymer Physics Edition, Vol. 18, 1271-1283 (1980)

© 1980 John Wiley & Sons, Inc.

0098-1273/80/0018-1271\$01.00

CM 2